

Self-organized state formation in magnonic vortex crystals

DISSERTATION
ZUR ERLANGUNG DES DOKTORGRADES
AN DER FAKULTÄT FÜR MATHEMATIK,
INFORMATIK UND NATURWISSENSCHAFTEN
DER UNIVERSITÄT HAMBURG

vorgelegt von
Christian F. Adolff
geboren am 12.09.1986
in Hamburg

Hamburg
2015

Gutachter der Dissertation: Priv.-Doz. Dr. habil. Guido Meier
Prof. Dr. Ralf Röhlsberger
Prof. Dr. Riccardo Hertel

Mitglieder der Prüfungskommission: Prof. Dr. Daniela Pfannkuche (Vorsitz)
Priv.-Doz. Dr. habil. Guido Meier
Prof. Dr. Ulrich Merkt
Prof. Dr. Ralf Röhlsberger
Prof. Dr. Michael Thorwart

Datum der Disputation: 04. November 2015

Abstract

Complexity created by periodic arrangement of well-understood building blocks plays an important role in biochemistry, photonics, engineering and nanoelectrics. The periodic arrangement of atoms or molecules as basis determines the physical properties of crystals. With the flexibility of nanometer precise electron-beam lithography here magnetic interactions are engineered yielding two-dimensional magnonic crystals that benefit from the magnetic vortex core as crystal basis. Using scanning transmission X-ray microscopy at the MAXYMUS beamline at BESSY II in Berlin, Germany the magnonic crystal dynamics are imaged with time resolution in the sub-nanosecond regime and simultaneous spatial resolution on the nanometer scale. Self-organized vortex core state formation by adiabatic reduction of a high frequency magnetic field excitation is observed. The emerging polarization states are shown to depend on the frequency of excitation and the strength of the dipolar interaction between the elements. In spite of the complexity of the investigated system, global order caused by local interactions creates polarization states with a high degree of symmetry. An analytical dipole model and numerically solved coupled equations of motion are adopted to analytically describe the experimental results. The emerging states can be predicted by a fundamental stability criterion based on the excitability of eigenmodes in the crystal. Further experiments with ferromagnetic absorption spectroscopy are carried out that give insight into the characteristic frequencies of the vortex dynamics that are crucially influenced by the self-organized state formation. This is emphasized with experiments on benzene-like magnetic vortex molecules whose motions show strong similarities to the vibrational modes of the actual benzene molecule (C_6H_6). The symmetry of both systems determines the motions of the oscillators, i.e., the carbon atoms or the magnetic vortices. This allows to simplify the derivation of the fundamentally different dispersion relations depending on the previously tuned polarization state. The experiments confirm the calculations and prove that the magnetic vortex molecule features a reprogrammable band structure or dispersion relation. Consequently, this work allows further research studies to tailor the characteristic properties of various magnetic vortex arrangements by tuning the polarization state.

Kurzzusammenfassung

Das Zusammenspiel einer Vielzahl gleichartiger, gut verstandener Bausteine spielt eine entscheidende Rolle in vielen komplexen Systemen verschiedenster wissenschaftlicher Disziplinen wie Biochemie, Photonik, Ingenieurwissenschaften oder Nanoelektronik. Zum Beispiel bestimmen periodische Anordnungen von Atomen oder Molekülen die physikalischen Eigenschaften von Kristallen. In dieser Arbeit werden magnetisch wechselwirkende Wirbel, sogenannte magnetische Vortizes, zu magnonischen Kristallen angeordnet. Die verwendete Elektronenstrahl-Lithographie erlaubt es, die Vortizes mit Nanometer-Präzision herzustellen und als Basis auf einer regelmäßigen Kristallstruktur zu platzieren. Mittels zeitaufgelöster Röntgenmikroskopie am MAXYMUS Mikroskop (BESSY II Synchrotron, Helmholtz-Zentrum Berlin) ist es möglich, die dynamischen Prozesse mit einer Zeitauflösung von unter einer Nanosekunde und gleichzeitiger örtlicher Auflösung auf der Nanometer-Skala abzubilden. In den Experimenten wird ein hochfrequentes magnetisches Anregungsfeld adiabatisch reduziert. Dies führt zu einer selbstorganisierten Einstellung der Polarisierungen der Vortizes im Kristall. Trotz der Komplexität der untersuchten Systeme erzeugen die lokalen Interaktionen eine globale Ordnung in Form von hochsymmetrischen Polarisationszuständen. Diese hängen von der Anregungsfrequenz und der Stärke der hauptsächlich dipolaren magnetischen Wechselwirkung der Vortizes ab. Zur Beschreibung der experimentellen Ergebnisse wird ein analytisches Modell entwickelt und numerisch gelöste Bewegungsgleichungen werden untersucht. Die selbstorganisierten eingestellten Polarisationszustände können daraufhin mit einem elementaren Stabilitätskriterium erklärt werden, das auf der Anregbarkeit von Eigenmoden im Kristall basiert. Weitere Messungen mit ferromagnetischer Absorptionsspektroskopie erlauben es, die deutlichen Einflüsse der selbstorganisierten Zustandseinstellung auf die charakteristischen Frequenzen der Vortex-Bewegungen zu studieren. Diese Einflüsse werden weiter in Experimenten an ringartigen Anordnungen von Vortizes, die starke Ähnlichkeit zum Molekül Benzol (C_6H_6) haben, untersucht. Bei beiden Systemen bestimmt die Symmetrie die Bewegung der Oszillatoren, das heißt der Kohlenstoffatome beziehungsweise der magnetischen Vortizes. Dies erlaubt es auf vereinfachte Weise in einem analytischen Dipol-Modell die Dispersionsrelation des Vortex-Moleküls herzuleiten, die stark vom vorherrschenden Polarisationszustand abhängt. In den Experimenten wird die Polarisationsabhängigkeit bestätigt und somit gezeigt, dass das magnetische Vortex-Molekül eine einstellbare Bandstruktur beziehungsweise Dispersionsrelation aufweist. Infolgedessen erlaubt es diese Arbeit weiterführenden Studien die charakteristischen Eigenschaften vielfältiger Anordnungen magnetischer Vortizes gezielt zu manipulieren und maßzuschneidern.

Contents

1. Introduction	1
2. The Magnetic Vortex	3
2.1. Thiele Model for Magnetic Vortices	8
2.2. Coupled Thiele Equations	10
2.2.1. Stray-Field Coupling via Surface Charges	11
2.2.2. Circular-Trajectory Dipole-Approximation	15
3. Experimental Methods	23
3.1. Sample Preparation	23
3.2. Scanning Transmission X-ray Microscopy	27
3.3. Ferromagnetic Absorption Spectroscopy	36
4. Self-Organized State Formation in Magnonic Vortex Crystals	39
4.1. Time-Scale of the State Formation	48
4.2. Larger Crystals	51
4.2.1. Rectangular Crystals	52
4.2.2. Kagome Lattice with Pairs of Vortices	55
4.3. Indirect Self-Organized State Formation	57
5. Ring-Shaped Magnetic Vortex Molecules	61
5.1. Molecule With Eight Vortices	65
5.2. Benzene-Like Vortex Molecule	69
6. Conclusion and Outlook	77
Bibliography	81

A. Appendices	91
A.1. List of Publications	91
A.2. Model Parameters	93
A.3. Auxiliary Calculations	96
A.4. Image Processing on Vortex Domain Walls	102
A.5. Micromagnetic Simulations of the SOSF in 3×3 Crystals	103
A.6. Further Results of the SOSF in 3×3 Crystals	104
A.7. Process Parameters	105

The career of a young [theoretical] physicist consists of treating the harmonic oscillator in ever-increasing levels of abstraction.

(Sidney R. Coleman (1937-2007), said in his lectures at Harvard University.)

1. Introduction

The harmonic oscillator is one of the major concepts of modern and classical physics, described in many basic textbooks. It is commonly introduced on the example of a spring pendulum in classical mechanics. In the simplest case, it is a system that, when displaced from its equilibrium position, experiences a restoring force that is proportional to the displacement. Coupled systems of (quantum) harmonic oscillators feature collective modes that have analogies in several physical systems, in particular in the lattice vibrations of solids. The concepts of a band-structure or dispersion relation allow to describe the crystal properties, e.g., the heat capacity, on the basis of such lattice vibrations. Subject of this work are magnetic vortex structures [Wac02] that are enclosed in thin ferromagnetic disks. They feature several analogies to classical harmonic oscillators. The center region of the magnetic vortex can be understood as a rigid magnetic particle that experiences a restoring force when deflected from its equilibrium position at the center of the disk. In order to reach its equilibrium position again, the magnetic vortex performs an approximately circular, damped gyration around the center of the disk; comparable to the motion of an initially deflected spring-pendulum. During the gyration the vortices exhibit a magnetic stray field that implies a coupling with neighboring vortices. Consequently, regular arrangements of vortices, so called *magnonic vortex crystals*, feature collective vibration modes that can be described using common concepts of solid-state physics, i.e., group velocity, density of states, and band structure [Kru10a; Len11]. As other magnonic crystals, i.e., wave transmission media that feature an artificial lattice created by a periodically modulated magnetic material, magnonic vortex crystals contribute to the research field of *Magnonics* that emerges at the interfaces between the study of spin dynamics, on the one hand, and nanoscale science on the other [Kru10a; Kru10b]. Vortex crystals are candidates for man-made, artificial crystals that feature a reprogrammable band structure [Kra14]. This is due to the so-called *polarization*, a binary state-parameter of the magnetic vortex that strongly influences the coupling. In the same way the control over the relative polarization of vortex arrangements allows for electronic

devices based on magnetic vortices that allow to store or process data – like a random access memory [Boh08] or the recently demonstrated transistor operations [Kum14]. The main topic of this work is the phenomenon of the self-organized formation of polarization states in arrangements of magnetic vortices (chapter 4). After the introduction of the field of magnetic vortices and the experimental methods (chapter 2 and chapter 3), we will see that an adiabatic reduction of a high-frequency magnetic field excitation leads to a self-organized relaxation of the vortex-system into well-ordered polarization states. Consequently, this work allows to tailor the characteristic properties of magnonic vortex crystals by tuning the polarization state. Prior to the outlook on further studies that closes the thesis (chapter 6), this will be demonstrated exemplarily by the manipulation of the dispersion relation of ring-like magnetic vortex arrangements (chapter 5) that resemble the benzene molecule (C_6H_6). Especially when comparing the normal modes of the actual benzene and the vortex-molecule the abovementioned analogies between harmonic oscillators and magnetic vortices become evident.

2. The Magnetic Vortex

This work is about the collective behavior of arrangements of magnetic ground-state configurations that are present in magnetic microdisks of suitable geometry – the magnetic vortices. Basis for the presented findings is the understanding of a single magnetic vortex which is the building block of the experiments. This chapter serves as an introduction to the field of magnetic vortices. It starts with a phenomenological description of the properties of the magnetic vortex that are shortly motivated by the theory of micromagnetism. A deeper understanding of the fundamentals of magnetism and magneto dynamics on the nanoscale can be gained from textbooks like Ref. [Stö06] or Ref. [Aha00]. The main focus of this chapter is the extended Thiele model [Thi73; Krü07] that allows to describe the dynamics of magnetic vortices in an efficient and sophisticated fashion. The last part of this chapter deals with the stray-field coupling of magnetic vortices in the Thiele model. Besides the common rigid-vortex-approach with surface-charge coupling [Gus01b; Suk13], an analytical approximation that was developed in the context of this work will be presented. In order to get a basic understanding, a pair of coupled vortices will be discussed exemplarily. This chapter constitutes the foundation for the interpretation of the experiments.

Magnetic vortices emerge in ferromagnetic microstructures. As for all magnetic solids, the magnetic properties of such structures are characterized by the magnetic moment per volume, i.e., the *magnetization* \vec{M} . The magnetic induction \vec{B} of Maxwell's equations can be calculated from the magnetization and the external magnetic field \vec{H} according to

$$\vec{B} = \mu_0(\vec{H} + \vec{M}), \quad (2.1)$$

where $\mu_0 = 4\pi \cdot 10^{-7} \text{ V s A}^{-1} \text{ m}^{-1}$ is the magnetic vacuum permeability. Unlike in only diamagnetic or paramagnetic materials, the magnetic moments of the atoms in a ferromagnetic material are not independent, but spontaneously align parallel to each other

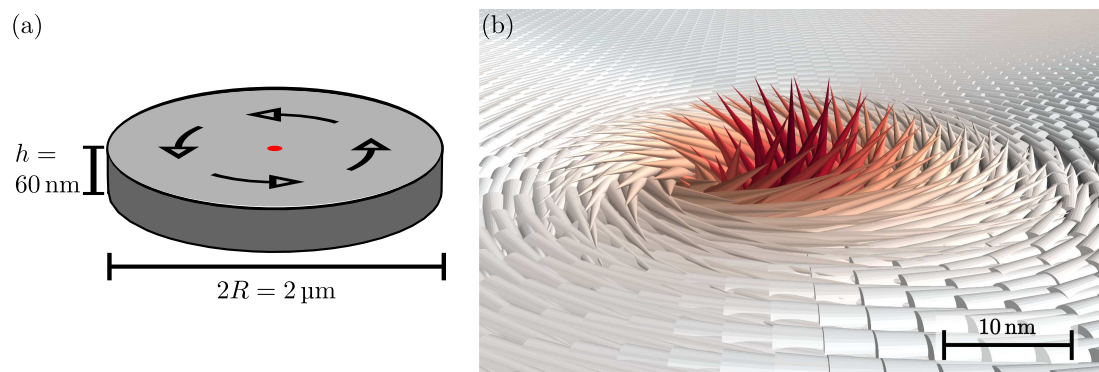


Figure 2.1.: Magnetic vortex state in a ferromagnetic micro disk. (a) Schematic of the magnetization curling around the vortex core in the center of the disk (red dot). The standard dimensions of the disks investigated in this work are depicted. (b) Close-up of the magnetization in the magnetic vortex core region. The z -component of the magnetization is color-coded in red. The vortex core has a typical size of a few ten nm.

inside of small regions, the so-called magnetic domains [Stö06]. Ferromagnetic microstructures enclose a few or only a single domain. The absolute value of the magnetization inside such a domain $M_S = |\vec{M}|$ is a material specific constant called *saturation magnetization*. For the material Permalloy ($\text{Ni}_{80}\text{Fe}_{20}$), used in the context of this work, a value of $M_S = 8 \cdot 10^5 \text{ A m}^{-1}$ is reasonable [Krü07]. Magnetic microstructures can be described with the *micromagnetic model* [Bro59] that is based on the treatment of the magnetization as a continuous vector field $\vec{M}(\vec{r})$. For the magnetic vortex, the magnetization curls in the plane around a center region, called the magnetic vortex core, where it turns out out-of-plane [Wac02]. Magnetic vortex states can be present in various magnetic microstructures, including disks, flat rectangular structures or wires [Shi00; Gol03; Nak05]. In this work magnetic vortices are investigated that are enclosed in thin microdisks as depicted in Fig. 2.1. In the micromagnetic model the emergence of the magnetic vortex as the magnetic ground state can be motivated by the minimization of all micromagnetic energies. For the investigated Permalloy disks two micromagnetic energies are dominant in the absence of external magnetic fields. The *exchange energy* models the parallel alignment of the magnetic moments in ferromagnetic materials. It is increased by inhomogeneities of the magnetization. The *demagnetization energy* describes the interaction of the magnetization with the *stray-field* that is generated by the microstructure itself. The stray-field \vec{H}_d is a result of Eqn. 2.1 and Maxwell's second equation. According to

$$\vec{\nabla} \vec{B} = \mu_0 \vec{\nabla} \cdot (\vec{H}_d + \vec{M}) = 0, \quad (2.2)$$

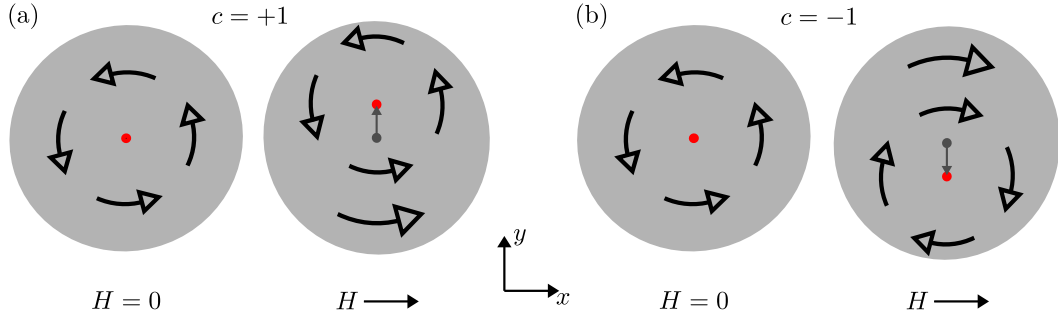


Figure 2.2.: Deflection of the magnetic vortex with a static magnetic field in x -direction. The deflection depends on the chirality c . (a) A positive chirality $c = +1$ leads to a deflection in positive y -direction. (b) A negative chirality $c = -1$ leads to a deflection in negative y -direction.

sources of the stray-field \vec{H}_d are sinks of the magnetization \vec{M} . They are also called *magnetic charges*. The demagnetization energy is reduced when surface charges are avoided [Kro62]. It follows that the magnetization aligns parallel to the surface of the microstructure. This effect is known as *shape anisotropy* and forces the magnetization to lie in the plane of the thin disk and align parallel to the border. In the core region the curling magnetization would lead to large angles between neighboring magnetic moments being unfavorable with regards to the exchange energy. Thus, the magnetization tilts out of the plane in the core region and the magnetic vortex forms as the magnetic ground state in the disk.

When an external magnetic field is applied, a third micromagnetic energy comes into play, the so-called *Zeeman energy*. It is minimized by a parallel alignment of the magnetization to the applied field. For very strong homogenous and static magnetic fields the Zeeman energy becomes dominant over all other micromagnetic energies. Consequently, the magnetization of the whole disk aligns parallel to the field. The magnetic vortex state is destroyed. For smaller field strengths the vortex state is still present but the core region is deflected from the center of the disk in order to enlarge the number of magnetic moments that are aligned parallel to the field [Gus01a]. As depicted on Fig. 2.2, the deflection direction depends on the curling direction of the magnetization in the disk, i.e., the *chirality* c of the vortex. For a static magnetic field \vec{H} that points in x -direction a clockwise curling vortex ($c = -1$) is deflected in negative y -direction, and a counter-clockwise curling vortex ($c = +1$) is deflected in positive y -direction. For increasing magnetic-field strengths the vortex core is deflected further from the center of the disks until the vortex state is destroyed. Besides the chirality, the second state

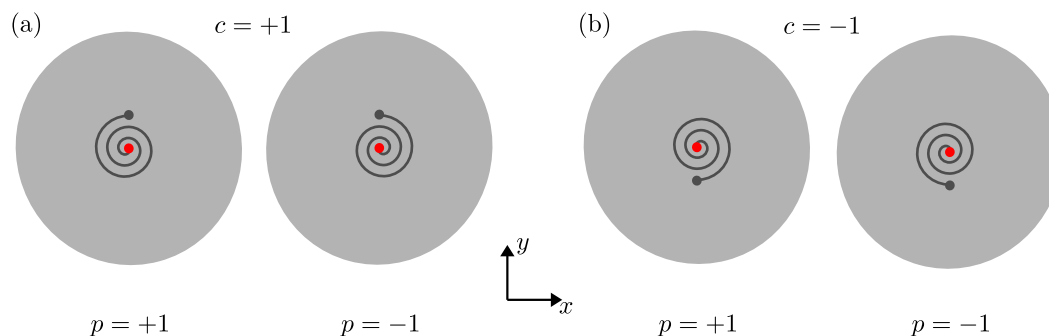


Figure 2.3.: Relaxation of a magnetic vortex subsequent to a deflection with a magnetic field in x -direction. The vortex core performs a damped gyration to its equilibrium position at the center of the disk. The gyration direction depends on the polarization p . (a) A positive polarization $p = +1$ leads to a clockwise gyration. (b) A negative polarization $p = -1$ leads to a counter-clockwise gyration.

parameter of the magnetic vortex is the out-of-plane direction of the vortex core in the center of the disk, i.e., the *polarization* p . For positive polarization $p = +1$, the magnetization in the core points in positive z -direction and it points in negative z -direction for negative polarization $p = -1$. The polarization comes into play when the magnetic field that deflects the vortices in Fig. 2.2 is switched off instantaneously. The micromagnetic energies change so that the energetically most favorable situation for the vortex core is to be in the center of the disk again. This state is not reached directly but after a damped gyration of the vortex around the center of the disk [Cho04] that is schematically depicted in Fig. 2.3. The gyration direction depends on the polarization of the vortex core. It is clockwise for negative polarization and counter-clockwise for positive polarization. The reason of this gyration is the so-called *gyrotropic mode* that is inherent to magnetic vortices. The frequency of the gyration depends on material parameters and the geometry of the disk [Gus02]. For the standard structures investigated in this work (radius $R = 1 \mu\text{m}$, height $h = 60 \text{ nm}$) the average frequency of the gyrotropic mode is around $(235 \pm 10) \text{ MHz}$ (depending on the respective preparation batch). The gyrotropic mode can be excited in various ways using magnetic fields or electric currents [VWa06; Kam11]. Here, alternating unidirectional magnetic fields that lie in the plane of the disk are used. After about 100 gyrations the transient states are damped out [Mar14] and the magnetic vortex core steadily gyrates on approximately circular trajectory around the center of the disk, when excited in resonance. This dynamic behavior can be understood in the micromagnetic model using the *Landau-Lifshitz-Gilbert equation* (LLGE)

which is a differential equation for the magnetization $\vec{M}(\vec{r})$ [Lan35; Gil56]. The LLGE is numerically solved in micromagnetic simulations that can be performed for example with the software *MicroMagnum*¹. Since the differential equation has to be solved for all position vectors \vec{r} and the demagnetization energy leads to a mutual long-range coupling of all discretization cells, the numerical calculation is very time consuming. Even with the efficient implementation of MicroMagnum that uses the graphics processing unit (GPU) to solve the LLGE, a simulation of the first 100 gyrations of a vortex contained in the standard-geometry disk lasts about 10 days.² Although the micromagnetic model with the LLGE is very precise it is in most cases impracticable for the calculations of steady state motions of large arrangements of coupled magnetic vortices. In this work another model will mainly be used to describe the magnetic vortex dynamics. The so-called *Thiele equation* is a differential equation [Thi73] that describes the vortex core as a quasiparticle that is confined in a parabolic potential [Krü07]. It can be deduced from the micromagnetic model and the LLGE with the approximation that the magnetization is only translated but does not alter its overall form [Gus01b]. Thus, the deflection of the vortex core is synonymous with the deflection of the whole vortex. The task of calculating 100 gyrations of the vortex core in the Thiele model lasts less than 50 ms.³ Thus, the computing time can be reduced by several orders of magnitude with respect to the micromagnetic simulation.

The Thiele model cannot explain polarization switching processes, because it assumes constant patterns of magnetization without internal excitation as a first principle. This is a major downside of the model since in this work the collective polarization switching of magnetic vortices is investigated. In the experiments the switching is induced, when the vortex core reaches a velocity higher than 250 m s^{-1} [Mar13]. This can only be understood in the micromagnetic model. Nevertheless, the Thiele model will prove to be sufficient to explain all major findings of this work. In the following section the Thiele model and its extensions to describe coupling magnetic vortices will be explained in detail.

¹Software download and documentation: <http://micromagnum.informatik.uni-hamburg.de>

²Cell-size: $(4 \times 4 \times 4) \text{ nm}$, System: NVIDIA Tesla M2090 GPU supported by Intel Xeon 2.67 GHz CPU)

³System: Intel Xeon 2.50 GHz CPU

2.1. Thiele Model for Magnetic Vortices

Originally the Thiele model was deduced from the LLGE for the example of rigid magnetic bubbles in thin films [Thi73] but it can also be adopted for magnetic vortices in thin-film elements [Krü07]. The minimization of the sum E of the micromagnetic energies described in the previous section is modeled by a force

$$\vec{F} = -\vec{\nabla}E \quad (2.3)$$

that acts on the quasiparticle (the vortex) at the position $\vec{x} = (x, y, z)^T$. This approach leads to the Thiele equation

$$\left(G_0^2 + \alpha_{\text{Gil}}^2 D_0^2\right) \dot{\vec{x}} = \vec{G} \times \vec{F} - \alpha_{\text{Gil}} D_0 \vec{F}. \quad (2.4)$$

Here, $\vec{G} = G_0 \vec{e}_z$ is the so-called *gyrovector*, and D_0 is the non-vanishing component of the diagonal *dissipation tensor* $D = \text{diag}(D_0, D_0, 0)$ [Krü07]. Analytically G_0 and D_0 are given by [Krü07; Vog10]:

$$D_0 = -\frac{2\pi\alpha_{\text{Gil}}\mu_0 M_S h \ln\left(\frac{R}{a_{\text{core}}}\right)}{\gamma}, \quad G_0 = -\frac{2\pi\mu_0 M_S h p}{\gamma} \quad (2.5)$$

where $\gamma = \frac{\mu_0 g e}{2m_e}$ is the gyromagnetic ratio with the Landé factor $g \approx 2$ and M_S is the material specific saturation magnetization. The radius of the disk is denoted with R and the geometry parameter h describes the height of the disk. The model parameter a_{core} is in the order of magnitude of the diameter of the vortex core. In the Thiele equation (Eqn. 2.4) two components add to the velocity $\dot{\vec{x}}$ of the vortex core. The first term describes the nature of the gyrotropic mode that moves the vortex perpendicular to the driving force \vec{F} . The second term depends on the dimensionless Gilbert damping parameter α_{Gil} and forces the vortex core back to its equilibrium position. For Permalloy $\alpha_{\text{Gil}} \approx 0.01$ applies [Liu07].

Without loss of generality (w.l.o.g.) the vortex equilibrium position can be chosen to be at the point of origin. Since the magnetic vortex can only move in the x - y -plane and only in-plane forces are considered, the z -component of the whole Thiele equation equals zero and the equation can also be represented in two dimensions:

$$\left(G_0^2 + \alpha_{\text{Gil}}^2 D_0^2\right) \dot{\vec{x}} = G_0 \tilde{r}_{90} \vec{F} - \alpha_{\text{Gil}} D_0 \vec{F}. \quad (2.6)$$

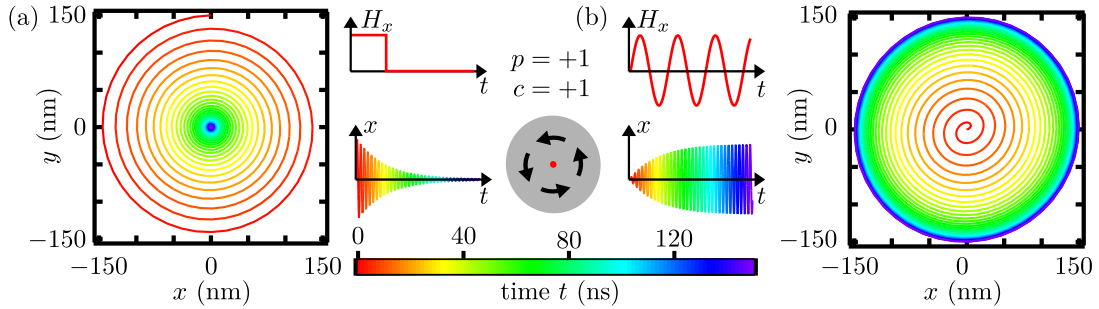


Figure 2.4.: Calculations for a single magnetic vortex in the Thiele model for two different magnetic-field excitations. The form of the exciting magnetic field in x -direction H_x is depicted in the insets. The time t is color coded. For the calculations positive chirality and polarization are given. (a) Trajectory of the vortex core gyrating back to its equilibrium position with the eigenfrequency of the gyrotropic mode after it has been deflected with a magnetic field in x -direction that is then switched off instantaneously. (b) The vortex core is resonantly excited with an alternating magnetic field near the eigenfrequency of the gyrotropic mode. It performs a transient motion until it reaches circular trajectories in the stationary case.

Here $\vec{x} = (x, y)^T$ is the deflection vector of the vortex core with respect to the center of the disk, \tilde{r}_{90} is a 90° rotation matrix in two dimensions and $F = (F_x, F_y)^T$ is the two-dimensional driving force.

According to Eqn. 2.3, the driving force \vec{F} follows from the total energy E that is deduced from the micromagnetic energies. The exchange and demagnetization energy are commonly modeled by a two-dimensional harmonic potential E_{harm} [Krü07] and a Zeeman term E_{Zee} takes external magnetic fields into account [Krü08]. The energy terms are given by

$$\begin{aligned} E_{\text{harm}} &= \frac{1}{2} \kappa_{\text{harm}} (x^2 + y^2) \\ E_{\text{Zee}} &= \mu_0 M_s \pi R h c (H_y x - H_x y). \end{aligned} \quad (2.7)$$

The total energy E is the sum of those two energies. The confining potential can also be described more precisely using anharmonicities [Dre12; Lan12; Suk13]. This approach gains importance for large deflections of the vortex core within the disk. Although the vortices reach relatively large deflections right before the switching process it is possible to obtain a good understanding of the self-organized state formation by only using the harmonic potential. Figure 2.4 depicts sample calculations in the Thiele model that show the two cases of vortex dynamics that were discussed in the last section. In Fig. 2.4(a) the vortex is deflected with a static magnetic field and then freely gyrates back to its

equilibrium position in the center of the disk after the magnetic field is switched off. Figure 2.4(b) shows how the vortex reaches its stationary gyrotropic motion, when it is excited with a unidirectional alternating field near the frequency of the gyrotropic mode. In order to describe the model parameters the abbreviations

$$\omega_0 = -\frac{pG_0\kappa_{\text{harm}}}{G_0^2 + D_0^2\alpha_{\text{Gil}}^2} \quad \Gamma = -\frac{D_0\alpha_{\text{Gil}}\kappa_{\text{harm}}}{G_0^2 + D_0^2\alpha_{\text{Gil}}^2} \quad (2.8)$$

are used. Those parameters can directly be deduced from experiments similar to the calculations presented in Fig. 2.4. For negligible damping, the angular frequency of the gyrotropic motion equals the model parameter ω_0 . The parameter Γ describes the damping of the motions. All simulations in this chapter are performed using the parameter set $(\omega_0/2\pi, \Gamma) = (227.6 \text{ MHz}, 29 \cdot 10^6 \text{ s}^{-1})$. It corresponds to a typical ratio $\frac{\Gamma}{\omega_0} \approx 2\alpha_{\text{Gil}}$ found in other experiments [Mar13]. A complete listing of all parameter sets used in this work can be found in appendix A.2.

2.2. Coupled Thiele Equations

Since arrangements consisting of multiple interacting vortices are analyzed, the particle model has to consider magneto-statical interaction of separated vortex structures. A system of N magnetic vortices can be described by a $2N$ -dimensional Thiele equation. Each two-dimensional component of this equation reads

$$(G_0^2 + \alpha_{\text{Gil}}^2 D_0^2) \dot{\vec{x}}_i = G_0 \tilde{\tau}_{90} \vec{F}_i - \alpha_{\text{Gil}} D_0 \vec{F}_i, \quad i \in \{0, 1, \dots, N-1\} \quad (2.9)$$

analogous to Eqn. 2.6, where \vec{x}_i denotes the deflection of the vortex i with respect to the center of its containing disk and \vec{F}_i describes the overall force that acts on vortex i . Besides the forces \vec{F}_{harm} and \vec{F}_{zee} following from Eqn. 2.3 and 2.7, additional forces $\vec{F}_{\text{int},ij}$ act on each vortex i that take into account the coupling with a vortex $j \neq i$. According to the Maxwell superposition principle the interaction energy of multiple interacting vortices is calculated by the sum of all pair interaction terms. Thus, in this model a single vortex is subjected to the force \vec{F}_i of the form:

$$\vec{F}_i = -\vec{\nabla} E_{\text{harm},i} - \vec{\nabla} E_{\text{zee},i} - \vec{\nabla} \sum_{j \neq i} E_{\text{int},ij}. \quad (2.10)$$

In the following sections two basic approaches for modeling the interaction energy $E_{\text{int},ij}$ will be presented.

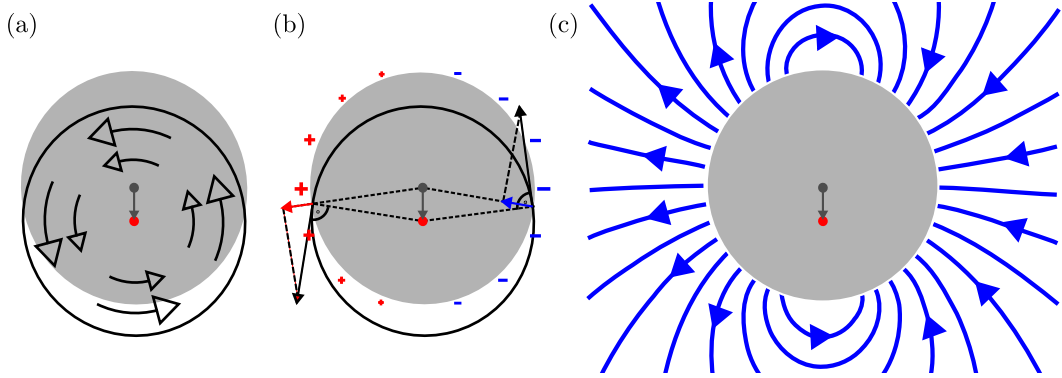


Figure 2.5.: Rigid vortex deflected from the center position. (a) The deflected magnetization pattern introduces non-parallel components at the edges of the disk. (b) The emerging surface charges are proportional to the normal component of the magnetization relative to the edge of the disk. They are indicated in red and blue. (c) The emerging stray-field is of mainly dipolar nature [Suk13].

2.2.1. Stray-Field Coupling via Surface Charges

Commonly the *rigid vortex approach* suggested by Guslienko et al., Ref. [Gus01b], is used to describe the stray-field interaction of magnetic vortices. Here, the coupling is considered by interacting so-called *magnetic surface charges*

$$\sigma = \vec{M} \cdot \vec{n} \quad (2.11)$$

that arise from deflected vortices at the sides of the disks. Where \vec{n} is the normal vector of the surface. The magnetization pattern of the deflected vortex itself remains constant. Volume charges $\rho_V = -\vec{\nabla} \cdot \vec{M}$ are absent and top and bottom surface charges are neglected. Figure 2.5 depicts a geometrical construction of the surface charges. An analytical expression for the surface charge σ_i of vortex i is given by [Shi03]

$$\sigma_i(\vec{x}_i, \varphi) = -\frac{c_i M_s}{R} \frac{x_i \sin \varphi - y_i \cos \varphi}{\sqrt{1 + \frac{|\vec{x}_i|^2}{R^2} - \frac{2}{R} (x_i \cos \varphi + y_i \sin \varphi)}}, \quad (2.12)$$

with the radius R of the disk, the deflection $\vec{x} = (x_i, y_i)^T$ of the vortex core from its equilibrium position, the chirality c_i , the saturation magnetization M_s and the angle φ in cylindrical coordinates. The energy of interacting surface charges σ_1 and σ_2 can be

written in the manner of Coulomb's law [Gus02]:

$$E_{int}(\vec{x}_1, \vec{x}_2) = \frac{\mu_0}{8\pi} \int dS_1 \int dS_2 \frac{\sigma_1(\vec{x}_1, \vec{r}_2) \sigma_2(\vec{x}_2, \vec{r}_2)}{|\vec{r}_1 - \vec{r}_2|}. \quad (2.13)$$

The integrals are taken over the side surfaces of the disks. For small deflections $|\vec{x}_i| \ll R$ Eqn 2.13 can be simplified into a Taylor series of first order in \vec{x}_i . This yields

$$E_{int,ij} = C_i C_j (s \hat{\eta}_{ij} \cdot \vec{x}_j) \cdot \vec{x}_i \quad \text{with} \quad \hat{\eta} = \begin{pmatrix} \eta_{xx} & \eta_{xy} \\ \eta_{yx} & \eta_{yy} \end{pmatrix}. \quad (2.14)$$

for the interaction energy of a vortex pair. Equation 2.15 lists the numerical integrals for the calculation of $\hat{\eta}$,

$$\begin{aligned} \eta_{xx} &= \frac{\mu_0}{8\pi} \frac{M_{s,i} M_{s,j}}{R_i R_j} \int dS_i \int dS_j \frac{\sin \varphi_i \sin \varphi_j}{|\vec{r}_i - \vec{r}_j|} \\ \eta_{xy} &= \frac{\mu_0}{8\pi} \frac{M_{s,i} M_{s,j}}{R_i R_j} \int dS_i \int dS_j \frac{-\sin \varphi_i \cos \varphi_j}{|\vec{r}_i - \vec{r}_j|} \\ \eta_{yx} &= \frac{\mu_0}{8\pi} \frac{M_{s,i} M_{s,j}}{R_i R_j} \int dS_i \int dS_j \frac{-\cos \varphi_i \sin \varphi_j}{|\vec{r}_i - \vec{r}_j|} \\ \eta_{yy} &= \frac{\mu_0}{8\pi} \frac{M_{s,i} M_{s,j}}{R_i R_j} \int dS_i \int dS_j \frac{\cos \varphi_i \cos \varphi_j}{|\vec{r}_i - \vec{r}_j|} \end{aligned} \quad (2.15)$$

which depend on the geometry, the magnetic properties, and the relative positions of the coupled vortices. The scaling factor $s < 1$ takes into account the theoretically predicted and experimentally observed fact that the coupling strength is overestimated by the rigid-vortex approach [Sug11; Vog12; Suk13]. The stray-field is mainly dipolar [Vog10]. Nevertheless, higher order terms (mainly octupolar [Suk13]) are regarded with this model as well. The coupled Thiele equation (Eqn. 2.9) is solved numerically using the Runge-Kutta-Fehlberg 45 method with variable step size control [Gal07]. Figure 2.6 shows an example calculation performed for a single disk and a pair of interacting disks. Figure 2.6(a) shows the resonance of the vortex velocity $\dot{\vec{x}}_i^2$ of the stationary motion when the vortex is excited with a unidirectional alternating field. The frequency of the resonance peak of an isolated disk will be denoted with ω_{iso} in the following. Due to the damping it is not exactly identical to the model parameter ω_0 . For the shown calculation the difference accounts for $\omega_{iso} - \omega_0 = 0.2$ MHz. The average squared velocity of the vortices versus the frequency of the magnetic-field excitation will be called frequency response in the following. It is comparable to the experimental results of the ferromagnetic absorption spectroscopy described in the next chapter. Figure 2.6(b) takes into account

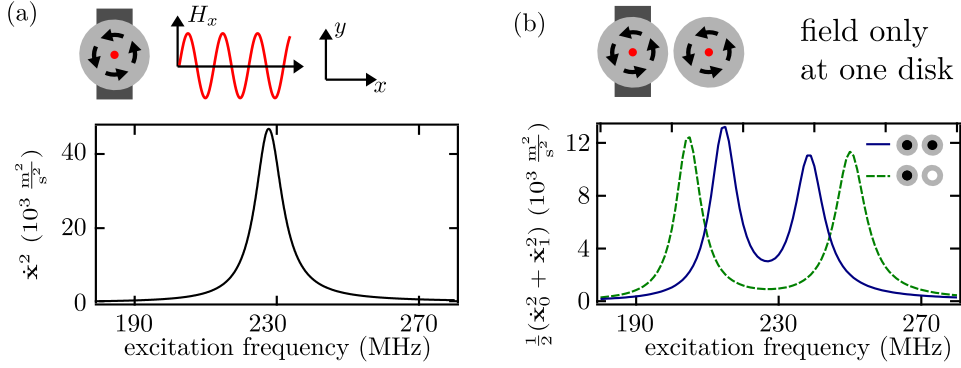


Figure 2.6.: Frequency response of a single disk and a pair of coupled disk. The frequency of an alternating magnetic-field excitation in x -direction is varied. The mean squared velocities of the stationary vortex gyrations are determined. (a) Single magnetic vortex. The gyrotropic mode is excited resonantly at the frequency of $\omega_{\text{iso}} \approx \omega_0 = 227.6$ MHz. (b) Pair of magnetic vortices. The center-to-center distance of the vortices is $2.05 \mu\text{m}$. Only one vortex of the pair is subjected to the alternating excitation-field. The frequency response depends on the relative polarization configuration, i.e., identical (solid blue) and alternating (dashed green) polarizations.

the coupling with another disk located near the first disk but not subjected to the exciting field. This can be realized experimentally when a stripline is placed only over the first disk and a current is applied that generates an Oersted field. The frequency response, i.e., the average squared velocities of the vortices $\frac{1}{N} \sum_i \dot{x}_i^2$, depends on the relative core polarizations, i.e., identical or opposite polarizations. For both cases two peaks of efficient excitation occur, that are more separated for the case of opposite polarizations. This can be understood in analogy to the spring pendulum [Vog11; Hän14]. Two coupled spring pendulums have two eigenmodes, i.e., an in-phase and an antiphase motion of the oscillators. The eigenfrequencies of those motions differ whereas their separation is determined by the strength of the spring. In the same way the two peaks in Fig. 2.6 correspond to an in-phase and an anti-phase motion of the vortices that are excited efficiently at different frequencies. The coupling strength is higher for the case of opposite polarizations [Vog11]. The theoretical description of eigenmodes in coupled vortex arrangements is discussed in detail in the publication [Hän13; Hän14] and will not be further elaborated here⁴. The ansatz is to transform the Thiele equation to

$$\dot{\vec{u}} = \tilde{M}\vec{u}. \quad (2.16)$$

⁴Further results have been published in Ref. [Hän14] – “Tunable eigenmodes of coupled magnetic vortex oscillators” by Max Hänze, Christian F. Adolff, Markus Weigand, and Guido Meier.

where the components of the vector \vec{u} are the relative coordinates \vec{x}_i of the vortex cores and \tilde{M} is a $2N$ -dimensional constant quadratic matrix. Solutions of this first order differential equation are of the form $\vec{u} = \vec{v} \exp(\lambda t)$. Hereby, the system of Thiele equations has been reduced to an eigenvalue problem. This is possible when the damping is neglected ($\alpha_{\text{Gil}} = 0$). The eigenmotions of the vortices and the corresponding eigenfrequencies in general cannot be determined analytically but have to follow from numerical calculations. However, for the case of two identical vortices placed along the x -axis, the eigenmotions can be analytically determined [Hän13; Hän14]. They read

$$\begin{aligned} \vec{x}_{1,\text{in}} &= |b_{\text{in}}| \begin{pmatrix} c_1 \cos(\omega_{\text{in}}(t - t_{0,\text{in}})) \\ c_1 p_1 \sqrt{\frac{\kappa_s + \eta_{xx}}{\kappa_s + p_1 p_2 \eta_{yy}}} \sin(\omega_{\text{in}}(t - t_{0,\text{in}})) \end{pmatrix} \\ \vec{x}_{2,\text{in}} &= |b_{\text{in}}| \begin{pmatrix} c_2 \cos(\omega_{\text{in}}(t - t_{0,\text{in}})) \\ c_2 p_2 \sqrt{\frac{\kappa_s + \eta_{xx}}{\kappa_s + p_1 p_2 \eta_{yy}}} \sin(\omega_{\text{in}}(t - t_{0,\text{in}})) \end{pmatrix} \end{aligned} \quad (2.17)$$

for the in-phase motion and

$$\begin{aligned} \vec{x}_{1,\text{an}} &= |b_{\text{an}}| \begin{pmatrix} c_1 \cos(\omega_{\text{an}}(t - t_{0,\text{an}})) \\ c_1 p_1 \sqrt{\frac{\kappa_s - \eta_{xx}}{\kappa_s - p_1 p_2 \eta_{yy}}} \sin(\omega_{\text{an}}(t - t_{0,\text{an}})) \end{pmatrix} \\ \vec{x}_{2,\text{an}} &= |b_{\text{an}}| \begin{pmatrix} -c_2 \cos(\omega_{\text{an}}(t - t_{0,\text{an}})) \\ -c_2 p_2 \sqrt{\frac{\kappa_s - \eta_{xx}}{\kappa_s - p_1 p_2 \eta_{yy}}} \sin(\omega_{\text{an}}(t - t_{0,\text{an}})) \end{pmatrix} \end{aligned} \quad (2.18)$$

for the anti-phase motion. The times $t_{0,\text{in}}, t_{0,\text{an}}$, and the amplitude factors $|b_{\text{in}}|, |b_{\text{an}}|$ define the initial deflection of the system. The coupling coefficient η_{xx} is positive and η_{yy} is negative. The sense of gyration is determined by the polarization of each vortex, whereas the chirality affects the phase correlation. It can be seen that the eigenmotions are elliptical. The ellipticity depends on the coupling coefficients η_{xx} and η_{yy} . Even for the case of maximal coupling $\frac{D}{2R} = 1$ the relation

$$\frac{\eta_{xx}}{\kappa_s} < -\frac{\eta_{yy}}{\kappa_s} < \frac{1}{10} \quad (2.19)$$

applies for the standard geometry. Thus, the trajectories can be considered approximately circular. Note that the frequency response depicted in Fig. 2.6 does not depend on the relative chiralities of the vortices since the inversion of the sign of the surface charges by changing the chirality of a vortex is canceled out by a phase shift of 180° of the excited vortex gyration.

The presented dipolar stray-field coupling via surface charges allows to determine the motions of large arrangements of vortices in a sophisticated fashion. Therefore, it is used to substantiate many experimental results presented in this work. A way to get a qualitative understanding of the vortex trajectories is to determine the eigenmotions and eigenfrequencies. This can be done numerically for arbitrary arrangements of vortices when the damping is neglected. The motions of the damped system can then be understood as a superposition of undamped eigenmodes. In the following section the idea of eigenmodes is further simplified in order to allow easier, pure analytical calculations. For that, exactly circular trajectories are assumed and the stray-field coupling is modeled via magnetic point-dipoles that are located at the centers of the disks. At the end of the upcoming section the frequency response of a pair of disks when both disks are subjected to an alternating field will be discussed exemplarily. The results will be compared to numerical calculations performed with the model presented above.

2.2.2. Circular-Trajectory Dipole-Approximation⁵

The most fundamental approach to include stray-field coupling is to consider only the average magnetization of a disk when the magnetic vortex is deflected. In a first approximation the stray-field resembles the field of a magnetic point-dipole that is located in the center of the disk and points into the direction of the net magnetization [Vog10]. Figure 2.7 illustrates the dipole model exemplarily for a negative vortex chirality $c = -1$. The direction of the average magnetization and thus the direction of the point dipole is rotated by -90° with respect to the deflection direction of the vortex within the disk. The sign of the rotation depends on the chirality $c = \pm 1$ of the vortex. Thus, the point dipole $\vec{\mu}_i$ that represents vortex i is given by

$$\vec{\mu}_i = \tilde{x}_i C_i \tilde{r}_{90} \frac{\vec{x}_i}{|\vec{x}_i|} \quad (2.20)$$

The strength of the dipole $|\vec{\mu}_i| = \tilde{x}_i$ is denoted with \tilde{x}_i since it is approximately proportional to the deflection amplitude $x_i = |\vec{x}_i|$ of the vortex core. The interaction energy $E_{\text{int},ij}$ follows to be the interaction energy of two magnetic point dipoles

$$E_{\text{int},ij} = E_{\text{dipole},i,j} = \frac{\mu_0}{4\pi D_{ij}^3} \left(\vec{\mu}_i \vec{\mu}_j - \frac{3}{D_{ij}^2} (\vec{\mu}_i \vec{D}_{ij})(\vec{\mu}_j \vec{D}_{ij}) \right) \quad (2.21)$$

⁵Parts of this section have contributed to the publication "Gyrational modes of benzenelike magnetic vortex molecules" by Christian F. Adolff, Max Hanze, Matthias Pues, Markus Weigand, and Guido Meier. Copyright 2015 by the American Physical Society.

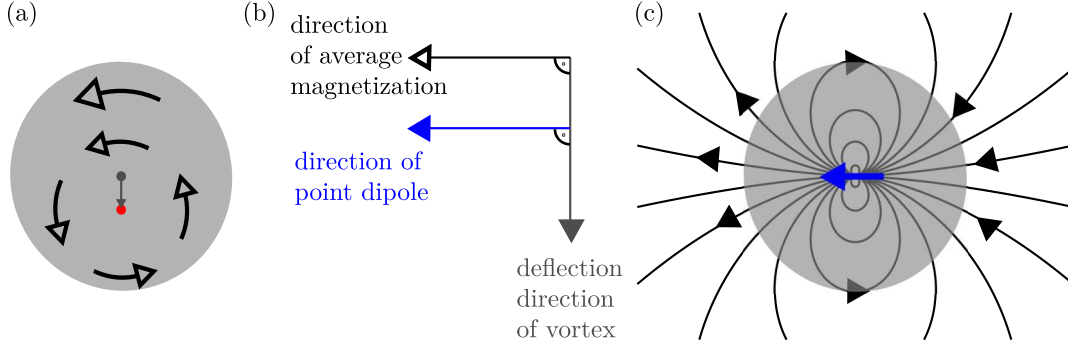


Figure 2.7.: Point-dipole approximation for the stray-field of a deflected magnetic vortex. (a) The deflection of the vortex ($c = -1$) induces a net magnetization of the disk. The direction of the average magnetization depends on the chirality c (see also Fig. 2.2). (b) Relative directions of the deflection of the vortex, the average magnetization, and the direction of the dipole. The latter two are shifted by $\pm 90^\circ$ with respect to the deflection direction depending on the chirality $c = \pm 1$ (c) Stray-field of the resulting magnetic point dipole that is located at the center of the disk.

The anchor points of the dipoles are assumed to be fixed at the centers of the disks. Thus, the vector \vec{D}_{ij} that connects the dipoles is constant.⁶ In the following we want to use this model to analytically investigate the influence of the coupling on the frequency response of a system of coupled vortices. As already described in the last section a system of N coupled vortices has N eigenfrequencies ω_e ($e \in \{1, 2 \dots N\}$) that all correspond to a specific eigenmode of the system. We assume, that such eigenmode will correspond to an approximate circular motion of all the vortices

$$\begin{aligned} \vec{x}_{e,i} &= \tilde{r}_\xi a_{e,i} C_i \begin{pmatrix} p_i \sin(\omega_e t + \varphi_{e,i}) \\ -\cos(\omega_e t + \varphi_{e,i}) \end{pmatrix} \\ &= a_{e,i} C_i \begin{pmatrix} p_i \sin(\omega_e t + \varphi_{e,i} + p_i \xi) \\ -\cos(\omega_e t + \varphi_{e,i} + p_i \xi) \end{pmatrix}. \end{aligned} \quad (2.22)$$

For negligible damping Eqn. 2.22 is the stationary solution of the Thiele equation for an isolated vortex that is excited near resonance with a unidirectional alternating field [Krü07; Mar12]. The angle between the direction of the field and the x -axis is denoted with ξ and \tilde{r}_ξ is the corresponding rotation matrix. In general Eqn. 2.22 is no solution

⁶By comparison of Eqn. 2.21 and Eqn. 2.14 one can see that the simplified model is identical to the numerical model, when $\eta_{xx} \propto (\frac{1}{D^3} - \frac{3D_y^2}{D^5})$, $\eta_{yy} \propto (\frac{1}{D^3} - \frac{3D_x^2}{D^5})$, $\eta_{xy} = \eta_{yx} \propto \frac{3D_x D_y}{D^5}$ is assumed. ($\vec{D} = (D_x, D_y)^T$.)

for coupled or damped case. Nevertheless this is a promising ansatz since approximately circular motions are observed in all experiments. Under this assumption an eigenmode of an arbitrary vortex arrangement with given chiralities c_i and polarizations p_i is fully determined by the N gyration amplitudes $a_{e,i}$ and phases $\varphi_{e,i}$. The eigenmode can be inserted into the Thiele equation (2.9) and then yields

$$\left(G_0'^2 + \alpha_{\text{Gil}}^2 D_0^2\right) \omega_e p_i \tilde{r}_{90} \vec{x}_{e,i} = -p_i G_0' \tilde{r}_{90} \vec{F}_i - \alpha_{\text{Gil}} D_0 \quad (2.23)$$

since for circular motions the time derivative is proportional to a rotation of 90° . The constant G_0 depends on the polarization of vortex i . To emphasize this, the substitution $G_0' := -G_0/p_i$ is used so that G_0' is a positive constant. When the damping is neglected ($\alpha_{\text{Gil}} = 0$), Eqn. 2.23 simplifies to

$$\omega \vec{x}_{e,i} = -\frac{1}{G_0'} \vec{F}_i. \quad (2.24)$$

This equation is one two-dimensional component of the N -dimensional differential equation. All vortex trajectories $\vec{x}_{e,i}$ are described by the $2N$ -dimensional vector $\vec{u}_e := (\vec{x}_{e,0}, \vec{x}_{e,1}, \dots, \vec{x}_{e,N-1})^T$. Thus the full equation reads

$$\omega_e \vec{u}_e = -\frac{1}{G_0'} (\vec{F}_0, \vec{F}_1, \dots, \vec{F}_{N-1})^T. \quad (2.25)$$

\vec{F}_i describes the sum of all driving forces of vortex i . Equation 2.25 is a simplified version of the undamped Thiele equation for circular trajectories. In principle it could be solved numerically in analogy to Eqn. 2.6. In the following another approach will be presented that considers the eigenfrequencies of the vortex gyrations. For that we further elaborate on Eqn. 2.25. Multiplying both sides of the equation with \vec{u}_e yields

$$\omega_e = -\frac{1}{G_0'} \frac{\sum_{i=0}^{N-1} \vec{x}_{e,i} \cdot \vec{F}_i}{\sum_{i=0}^{N-1} \vec{x}_{e,i}^2}. \quad (2.26)$$

To simplify the calculation we separate the influence of the forces that work on the isolated disks (i.e. $\vec{F}_{\text{iso},i}$) from the influence of the force $\vec{F}_{\text{int},i}$ that only exists for coupled

disks. With the substitution $Z_{N,e} = \sum_{i=0}^{N-1} \vec{x}_{e,i}^2$ this yields

$$\begin{aligned} \omega_e &= -\frac{1}{G'_0 Z_{N,e}} \left[\sum_{i=0}^{N-1} \vec{x}_{e,i} \cdot \vec{F}_{\text{iso},i} + \sum_{i=0}^{N-1} \vec{x}_{e,i} \cdot \vec{F}_{\text{int},i} \right] \\ &=: \omega_{\text{iso}} + \frac{1}{G'_0 Z_{N,e}} \sum_{i=0}^{N-1} \sum_{j \neq i} \vec{x}_{e,i} \cdot \vec{\nabla}_i \vec{E}_{\text{int},ij} \end{aligned} \quad (2.27)$$

The frequency of the gyrotropic mode of the isolated vortex following from the force $\vec{F}_{\text{iso},i}$ is denoted with ω_{iso} . The gradient operator $\vec{\nabla}$ only acts on the deflection coordinates \vec{x}_i . Regarding Eqn. 2.21 this yields the relation

$$\vec{x}_i \cdot \vec{\nabla}_i E_{\text{dipole},ij} = E_{\text{dipole},ij}. \quad (2.28)$$

Using this and the superposition principle yields

$$\omega_e - \omega_{\text{iso}} = \frac{1}{G'_0 Z_{N,e}} \sum_{i=0}^{N-1} \sum_{j \neq i} E_{\text{dipole},ij}. \quad (2.29)$$

Due to the several approximations performed the right side of this equation can still depend on the time t . To eliminate the time dependency both sides of the equation are integrated over one period of gyration. Commuting the summations with the integration yields

$$\omega_e - \omega_{\text{iso}} = \frac{1}{2\pi} \frac{1}{G'_0 Z_{N,e}} \sum_{i=0}^{N-1} \sum_{j \neq i} \int_{\omega t=0}^{\omega t=2\pi} E_{\text{dipole},ij} d(\omega t). \quad (2.30)$$

Thus, the frequency shift that is due to the coupling of the disks is shown to approximately be proportional to the average interaction energy during one period of gyration of the vortices. Figure 2.8 illustrates the dipolar interaction for two example deflections of a pair of magnetic vortices. One can see that the interaction energy strongly depends on the relative positions of the vortices. Accordingly, for such calculations the phases and amplitudes of the eigenmodes have to be known. In general those can be determined numerically as described in the previous section. For some special cases the eigenmodes can be enforced by external constraints, e.g. the symmetry of the system. This case is discussed in chapter 5 for ring-shaped arrangements of magnetic vortices. In the following we will discuss the boundary case of almost negligible coupling. When two disks

⁷The field-line plots have been performed with the free software *VectorFieldPlot* (url: <http://commons.wikimedia.org/wiki/User:Geek3/VectorFieldPlot>)

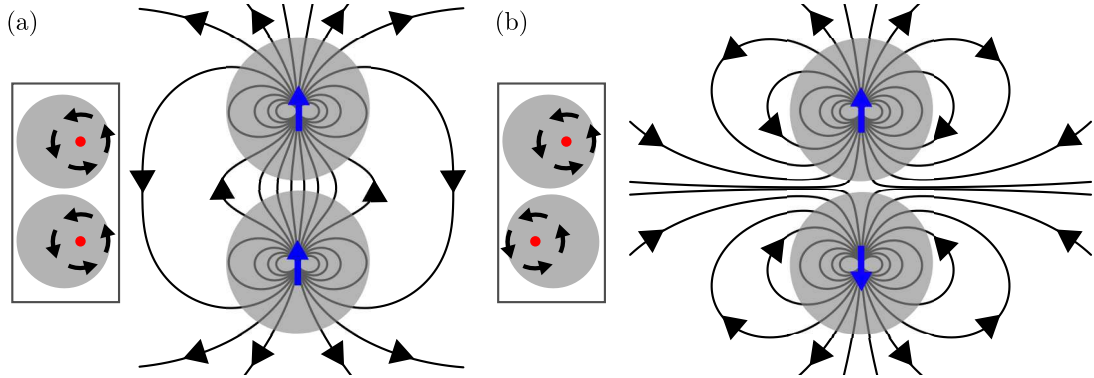


Figure 2.8.: Schematic⁷ of the dipole approximation for the stray-field interaction of vortices. Two different relative deflections of the vortex cores are depicted. (a) Parallel alignment. Typical for vortices of the same polarization when the coupling can be considered weak. (b) Anti-parallel alignment. Characteristic for the case of opposite polarizations.

are far away from one another, the external magnetic field dominates the vortex motion. Thus, all amplitudes a_i and phases φ_i are identical since the external magnetic field affects all vortices in the same way. In this boundary case, the two eigenmodes merge into one absorption peak. The coupling due to the stray-field can be regarded as a small perturbation. The relation

$$a_{e,i} = a \quad \varphi_{e,i} = \varphi \quad \forall i \in \{0, 1, \dots, N - 1\} \quad (2.31)$$

applies. Under this assumption Fig. 2.8 shows snapshots for the gyration of two vortices of identical (a) or opposite (b) polarizations when an alternating field in x -direction is applied. Figure 2.9(a) depicts an arrangement of two vortices where those boundary conditions can be assumed. The center-to-center distance of the disks is $4 \mu\text{m}$ so that the coupling can be considered weak [Mej06]. Thus, the motions are mainly given by the magnetic field that excites both disks equally. The variation of the frequency response is depicted when the pair is rotated with respect to the external magnetic field. As can be seen in Fig. 2.9(b) and (c), the frequency response has a single peak for each of the two relative polarization configurations and for each rotation angle θ . The angular frequency of this peak is assumed to correspond to the motion following from the negligible damping assumption (Eqn. 2.31) and the assumption of circular trajectories (Eq 2.22). It will be denoted with ω_p in the following equations. For the case of different polarizations ($p_1 p_2 = -1$) the frequency peaks depend on the rotation angle ϑ . In contrast, the peaks are independent of the rotation angle for the case of identical polarizations ($p_1 p_2 = 1$).

2. The Magnetic Vortex

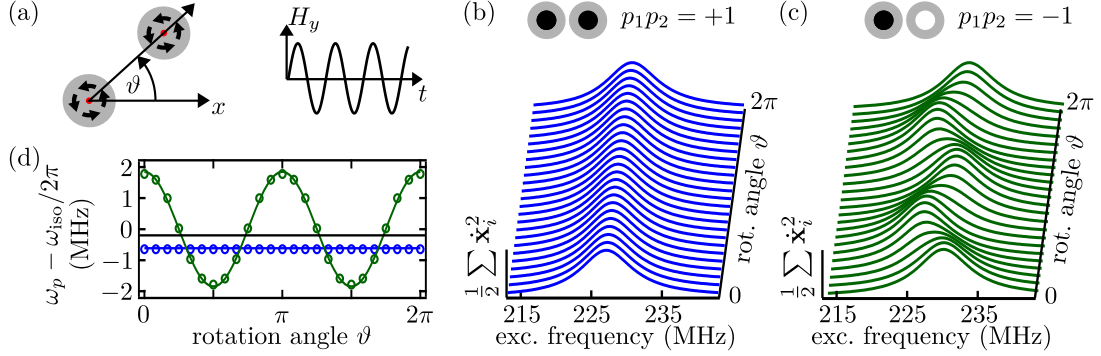


Figure 2.9.: Pair of weakly coupled disks rotated with respect to the external magnetic field. The alternating field points in y -direction. The center-to-center distance of the disks is $4\ \mu\text{m}$. Blue color depicts the case of identical polarizations, green the case of different polarizations. (a) Schematic. (b) Waterfall plot of the frequency response for the case of identical polarizations. Each line corresponds to another rotation angle. (c) Waterfall plot for different polarizations. (d) Analytical results of Eqn. 2.32 for the variation $\omega_p - \omega_{\text{iso}}$ of the peak frequency ω_p (colored solid lines) along with the position of the peaks (open circles) gained from the calculation depicted in (b) and (c). The solid black line depicts the difference $\omega_0 - \omega_{\text{iso}}$.

This can be understood with the relation 2.30 presented above. When inserting the assumptions Eqn 2.31, Eqn. 2.31 and the correct field angle for excitation in y -direction ($\xi = \pi/2$) this yields⁸

$$\begin{aligned} \omega_p - \omega_{\text{iso}} &= -\frac{\tilde{x}^2}{a^2} \frac{\mu_0}{16\pi D^3 G'_0} [(1 + p_1 p_2) + 3(p_1 p_2 - 1) \cos(2\theta)] \\ &=: \begin{cases} -\frac{B_2}{6} & \text{if } p_1 p_2 = +1 \\ \frac{B_2}{2} \cos(2\vartheta) & \text{if } p_1 p_2 = -1 \end{cases}. \end{aligned} \quad (2.32)$$

The prefactor $B_2 = \frac{3\tilde{x}^2}{a^2 G'_0} \frac{\mu_0}{4\pi D^3}$ can be understood as the bandwidth of the frequency variation. Lower center-to-center distances D increase the bandwidth B_2 . Figure 2.9(d) depicts this analytical prediction along with the frequencies that are determined from the numerical simulations presented in Fig 2.9(b) and (c). The calculation depicted in Fig. 2.6(a) yields the resonance frequency ω_{iso} of the isolated vortex. The bandwidth B_p has been fitted to the numerical calculations ($B_{p,\text{fit}}/2\pi = (3.70 \pm 0.20)$ MHz). One can see that the form of the fitted analytical predictions (solid lines) is in good agreement with the numeric calculations (open circles). Analytically the dependence of the bandwidth B_2 on the geometry parameters R, D , and h is of interest. For that, the strength $|\vec{\mu}_i| = \tilde{x}_i$

⁸The simplification is straight forward. For the mathematical proof see appendix A.3

has to be determined. The magnetic moment is given by the net magnetization in the disk. In our case it can be estimated by

$$\vec{\mu}_i = \int \vec{M}(\vec{r}) dV, \quad \text{with } M = M_S c_i \vec{e}_\beta \quad (2.33)$$

in cylindrical coordinates (polar angle denoted with β). The origin of the coordinate system is chosen to be at the vortex core. Due to the rigid-vortex approach the magnetization is rotationally symmetric. When small deflections of the vortex with respect to the disk radius are assumed, this yields

$$\tilde{x}^2 = |\vec{\mu}_i|^2 \propto (M_S \pi R h a)^2 \quad (2.34)$$

in analogy to the derivation of the Zeeman energy presented in Ref. [Krü08]. This yields

$$B_2 \propto M_S \gamma \frac{h}{R} \left(\frac{2R}{D} \right)^3. \quad (2.35)$$

The resonance of an isolated disk is known to depend approximately linearly on the ratio $\frac{h}{R}$ of the height h and the radius R of the disk [Gus02]. Thus, the bandwidth is scaled by the same factor. It can be seen in the cubic term that the bandwidth is strongly increased by a low center-to-center distance $\frac{D}{2R}$ with respect to the disk radius [Mej06].

In conclusion, we have seen in this chapter, that magnetic vortices build the ground state in microdisks of suitable geometry consisting of the ferromagnetic alloy Permalloy. They are described by two binary state parameters, i.e., chirality c and polarization p . The latter strongly influences the stray-field coupling between vortices in neighboring disks. Besides micromagnetic simulations, the motions of coupled vortices can be calculated in a particle model, the so-called extended Thiele model. Further analysis of the differential equation of motion for the undamped case allows to make use of the concept of eigenmodes. We have seen that there are similarities to the eigenmotions of coupled spring pendulums, whereas the coupling strength can be adjusted by the relative polarization configuration of the vortices. The frequency response of a weakly coupled pair of disks has been shown to depend on the average interaction energy during one period of gyration. For that, analytical calculations using a strongly simplified model have been performed. The model requires the vortices to gyrate on approximately circular trajectories. In addition, it has to be possible to estimate the relative phases and amplitudes of the mainly excited eigenmodes. For that, symmetry considerations can be used. This

will be presented in chapter 5 about ring-shaped arrangements of vortices. In the case of negligible damping the stray-field coupling can be considered as a small perturbation to the vortex dynamics. This boundary case has been evaluated numerically and analytically for a weakly coupled pair of disks. Pair interactions are the building block for larger coupled systems. According to Eqn. 2.30 the influences of the pair interactions simply add up to the overall shift ($\omega_e - \omega_{\text{iso}}$) of the frequency of a weakly coupled multi-vortex system. Thus, the results for the pair of disks can easily be extended to larger vortex arrangements.

3. Experimental Methods

Prior to the presentation and discussion of the results in chapter 4 and 5 the underlying methods that enable the experiments will be introduced. The measurements are performed at room-temperature using two complementary measurement methods, i.e., scanning transmission X-ray microscopy (STXM) and ferromagnetic absorption spectroscopy (FMR). The former allows to directly observe the trajectories of the magnetic vortices whereas the latter gives insight into the frequency response of the system. The two methods are used to investigate several arrangements of magnetic vortices in order to gain insight into the phenomenon of self-organized state formation. The samples are prepared using electron-beam lithography, thermal evaporation (PVD), and lift-off-processing on silicon-based substrates.

3.1. Sample Preparation

Inside the class 100/1000 cleanroom of the Microstructure Research Center of the University of Hamburg, the ferromagnetic thin-film microstructures are prepared. The preparation process is depicted schematically in Fig. 3.1. The fabrication of the striplines and the microdisks containing the vortices corresponds to two separate iterations following the same preparation principle. Bulk silicon substrates with 300 nm silicon-oxide coating are used for the absorption measurements and 100-nm-thick silicon nitride-membranes, transparent for soft X-rays, for the transmission X-ray microscopy. Primarily the substrate is coated with a positive e-beam resist based on polymethyl methacrylate (PMMA). Areas exposed to a sufficiently high dose of electron-beam radiation are altered structurally so that these areas can be removed by a chemical solvent, the developer. Consequently, a resist mask for the vapor deposition of the target material remains on the substrate. Subsequent to the exposure with a scanning electron microscope (Zeiss Supra 55) and the development of the mask, the target material can be deposited. For the microdisks a resist bi-layer is used in order to improve the results of the wet-chemical lift-off of the mask

3. Experimental Methods

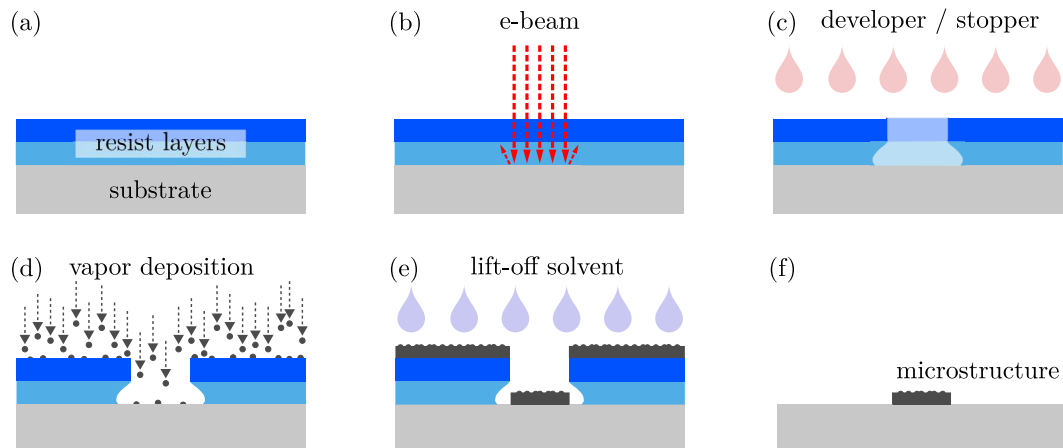


Figure 3.1.: Schematics of the preparation steps for the fabrication of a microstructure. (a) Substrate (bulk silicon with silicon-oxide coating or silicon-nitride membranes) with a resist bi-layer (positive PMMA resists) (b) Exposure of the resist layer via electron beam patterning (SEM: Zeiss Supra 55). (c) Wet-chemical development of resist chemically altered by the electron radiation. (d) Resulting resist mask for the deposition of the target material. (e) Wet-chemical removal (Lift-off) of the resist mask and the surplus material. (f) Final product: Thin-film element. The striplines are deposited onto the microstructure in a second, analogous preparation process.

and the excess material. For the bottom layer a resist with a higher sensitivity [All14] is used¹. Due to back scattering from the substrate and creation of secondary electrons in the substrate [Kys75] the resist mask undercuts at the edges (see Fig. 3.1(c)). This effect is enhanced by the bottom layer with a lower sensitivity and inhibits a direct contact between the deposited microstructure and the resist mask during the vapor deposition (see Fig. 3.1(e)). For the stripline a resist mono-layer with a medium sensitivity² is used that allows for a sufficiently high resist mask. After the development resist residues can occur. Figure 3.2(a) depicts an atomic force micrograph of a resist mask prepared in the context of this work. One can clearly see the residues that have a diameter of a few ten nm and a height of up to 30 nm. The mask has to be cleaned prior to the deposition of the microdisks since otherwise the 30 nm residues would result in pinning centers perturbing the vortex dynamics [Kam12] in the 60 nm thick disks. The issue of resist residues is known for several years, and yet no reason for the occurrence of the residues has been found with clarity [Kam12; Mar14; Pue15]. For the cleaning of the mask an O₂-plasma etching process is used. The process has been developed in the context of the doctoral studies of Matthias F.A. Pues, Ref [Pue15], who also installed the plasma etcher (Plasma

¹top layer: Allresist AR-600-56-P 950K, bottom layer Allresist AR-600-56-P 50K

²Allresist AR-600-56-P 600K

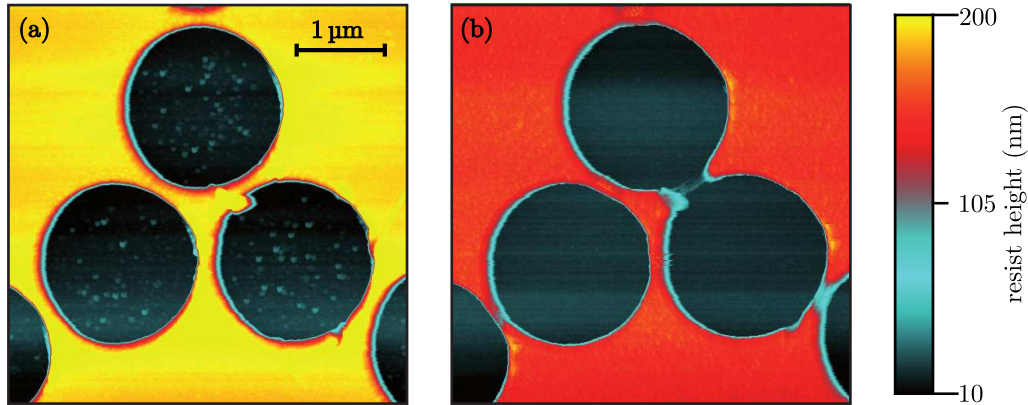


Figure 3.2.: Atomic force micrographs of a PMMA resist mask. (a) Before plasma etching. Resist residues appear in blue. (b) After plasma etching for 60 s at 70 W and an O_2 pressure of $3.3 \cdot 10^{-1}$ mbar. The residues are reduced and the mask is enlarged leading to an undesirable fusion of the disks.

Prep III from Structure Probe, Inc.). As can be seen in the atomic force micrograph in Fig. 3.2(b), the resist residues can effectively be reduced. During the isotropic etching process the mask is also enlarged in all directions since not only the residues but also the resist mask is etched away. This effect has to be considered during the design of the microstructures. As already discussed in the last chapter it can be desirable to reduce the disk interdistance to a minimum in order to increase the coupling strength. When the e-beam exposure is not adequately adapted to the etching process, the disks unwantedly merge into one structure. This effect can be seen in Fig. 3.2(b). The smallest interdistance that could be realized between two disks ($R = 1 \mu\text{m}$) in this work is 50 nm ($\frac{D_{\min}}{2R} = 1.025$).

The deposition is performed at a vacuum of $< 5 \cdot 10^{-7}$ mbar using a resistively heated boat evaporator for the ferromagnetic alloy Permalloy ($Ni_{80}Fe_{20}$) and the stripline material copper. An electron beam evaporator with a rotatable crucible revolver is used for a gold passivation layer. After the deposition of Permalloy the sample is exposed to the room atmosphere and is thereby passivated by a $1.5 \mu\text{m}$ oxide layer [Fit06]. The striplines (height: 120 nm to 150 nm) consist of copper since it shows a much higher transitivity for the used X-ray radiation than gold. A gold capping layer (height: 5 nm) is used to reduce the oxidization of the stripline. The deposition rates are monitored by a quartz crystal microbalance sensor that allows for a thickness accuracy of below 1 nm. The actually deposited film-thickness depends on many details of the PVD-system, especially the position

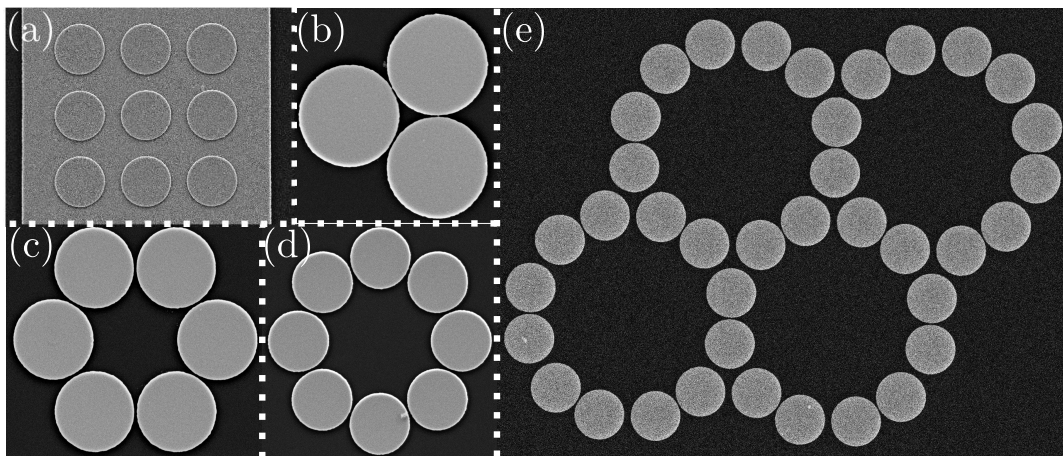


Figure 3.3.: Scanning electron micrographs of a selection of samples prepared in the context of this work. All disks show the standard geometry of $R = (1000 \pm 20)$ nm and $h = (60 \pm 3)$ nm for the different preparation batches. Within one sample the geometry variation is much smaller. (a) Rectangular arrangement of 3×3 disks covered by a stripline. The center-to-center distance is $D = 3$ μ m. (Experiments described in chapter 4.) (b) Triple of disks with the minimal achieved ratio $\frac{D}{2R} = 1.025$ ($D = 2.05$ μ m). (Experiments: section 4.3.) (c) and (d) Rings-like arrangement of six and eight disks prepared in the same way as the triple (see chapter 5 and section 3.2). (e) Arrangement of pairs of vortices with a small disk interdistance $D = 2.065$ μ m that build a hexagonal kagome lattice. The center-to-center distance of the disks that belong to different pairs is larger and amounts to $D = 2.125$ μ m (section 4.2.2).

of the sample-holder. Nevertheless a sub-nanometer precision can be achieved [Pue15]. The actual thicknesses and radii are determined via atomic-force and scanning-electron microscopy after the lift-off. Within one preparation process a nanometer-precision of the geometry can be achieved. Nevertheless experiments show that isolated disks on the same sample exhibit a variation of the resonance frequency of about ± 15 MHz due to sample impurities and edge-roughness. All parameters of the preparation are listed in Appendix A.7.

Figure 3.3 shows a selection of the arrangements of magnetic vortices that will be discussed in this work. Samples depicted in Fig. 3.3(a) and (c) constitute the focus of the result chapters 4 and 5, respectively. The rectangular arrangement of vortices depicted in Fig. 3.3(a) has been prepared in collaboration with Max Hanze in the context of the supervision of his master’s thesis. Analogous samples with a smaller center-to-center distance of $D = 2.25$ μ m have been prepared in the same batch. In contrast to the other samples presented in Fig. 3.3 the micrograph has been captured after the deposition of the stripline. The samples for the collaborations presented in section 4.1 and 4.2.1 are

not depicted in Fig. 3.3 and have been prepared by the first authors of the corresponding publications [Beh15; Hän15], Carolin Behncke and Max Hänze. All disks in Fig. 3.3 show the standard geometry, i.e., $R = 1000$ nm for the radius and $h = 60$ nm for the height of the microdiscs. This standard geometry has been chosen for mainly two reasons:

strong coupling is desirable. Since effects that arise from the stray-field coupling are in the focus of this work, strong coupling is generally desirable. According to Eqn. 2.34, large and high disks improve the coupling strengths. In addition, a low ratio $\frac{D}{2R}$ increases the coupling and leads to a stronger frequency splitting that can be observed more easily in the experiments (see Eqn.2.35). Since the minimum disks-interspace is limited to 50 nm due to the preparation technique, low ratios $\frac{D}{2R}$ can be achieved with relatively large radii.

adaption to the measurement techniques. Thicker films reduce the transitivity of the sample for the X-ray microscopy, practically resulting in increased exposure times. For the standard-height of $h = 60$ nm, capture times of about 1 minute for a $400 \text{ nm} \times 400 \text{ nm}$ area are a reasonable trade-off between coupling strength and capture time. In addition, the ferromagnetic-absorption spectroscopy-setup features an optimal sensitivity in the frequency range between 200 MHz and 400 MHz [Kam12]. The resonance frequency of an isolated disk and thus the frequency band of efficient excitation of an arrangement of vortices depends on the ratio $\frac{h}{R}$ [Gus02]. The samples presented in Fig. 3.3 shows resonance frequencies of isolated disks in the range of (225 ± 20) MHz. Thus, the disks with standard geometry can efficiently be investigated with both experimental setups.

In the following the two experimental setups will be discussed in more detail.

3.2. Scanning Transmission X-ray Microscopy

Figure 3.4 shows a schematic of the MAXYMUS microscope [MPI14] of the Max Planck Institute for Intelligent Systems (Stuttgart, Germany) located at the BESSY II synchrotron in Berlin, Germany that is used for the scanning transmission X-ray microscopy (STXM). The electrons filled into the ring accelerator emit synchrotron radiation in the range of soft X-rays that is used at the beamline (UE46-PGM2) built tangential to the ring. An undulator allows to adjust the polarization direction and the energy of the circularly polarized synchrotron radiation to the desired energy of the L_3 absorption edges

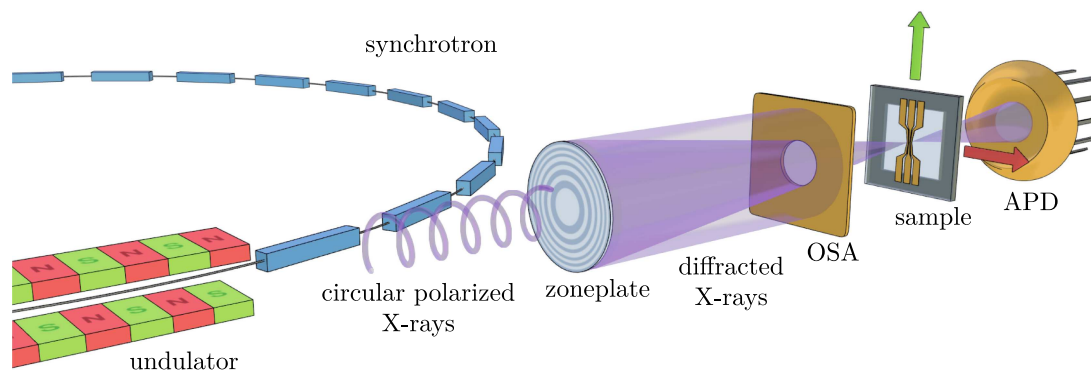


Figure 3.4.: Schematic of the scanning transmission X-ray microscope MAXYMUS at the Helmholtz-Zentrum Berlin, Germany. An undulator emits monochromatic photons of the required energy and polarization. The photons are focused onto the sample by a zone plate and the order selection aperture (OSA) that stops light of the 0th order. The sample is raster scanned through the fixed beam and the transmission is measured by an avalanche photo diode (APD). Figure reprinted with permission from Ref. [Mar14].

of nickel (853 eV) or iron (707 eV) that can be used to investigate the samples consisting of the ferromagnetic alloy permalloy ($\text{Ni}_{80}\text{Fe}_{20}$). Due to the exposure, $2p_{3/2}$ core electrons are excited into unoccupied states of the 3d valence band. This band plays a crucial role for the origin of the ferromagnetism [Sto38] in the investigated materials. The exchange interaction leads to an energy shift between the sub-bands of the two spin configurations and the different electron populations result in the net magnetic moment. The minority spins (w.l.o.g. spin-down in the following) always point in the direction of the magnetization \vec{M} considering the opposite directions of the spin and the magnetic moment in the quantum mechanical expression. Due to the so-called *X-ray magnetic circular dichroism* (XMCD) the excitation of the $2p_{3/2}$ electrons into the 3d valence band has a different cross-sections depending on the polarization of the incident photons and the direction of the magnetization [Sch87; Che95]. An excellent summary of the exact quantum-mechanical description is given in Ref. [Stö06]. The absorption of X-rays in matter is mainly given by an exponential decay that depends on the atomic number of the absorbing material and the photon energy [Tho09]. Concerning the investigation of thin magnetic films, the excitation of the electronic states described above (XMCD) results in an additional magnetization dependent absorption that provides magnetic contrast that is proportional to the projection of the photon propagation vector \vec{k} on the magnetization vector \vec{M} . As depicted in Fig. 3.4, a zone plate diffracts the synchrotron radiation

into several orders and the *orders selection aperture* (OSA) selects the light of higher order diffraction that is focused on one single spot of the sample. As common for scanning microscopy techniques the sample is moved relative to the focus point in order to pixel wise obtain the micrograph. The transmission is measured with an avalanche photo diode (APD). The scanning is realized by a movement of the sample that is mounted on a sample stage equipped with an interferometric feedback loop for the stepper motors and piezoelectric actuators for nanometer precise positioning. In Fig. 3.4 the sample is mounted perpendicular to the beam axis. This setup is used to image the vortex cores with out-of-plane contrast. The chiralities can be imaged when tilting the sample with respect to the beam-axis in order to obtain in-plane magnetic contrast.

The setup does not only provide a spatial resolution of about 25 nm limited by the currently installed zone-plate³, but for periodic magnetodynamics it also provides a temporal resolution that is mainly limited by the width of the synchrotron flashes of about 70 ps [MPI14]. This is a much higher temporal resolution than following from the repetition rate of the synchrotron (500 MHz) that results in light flashes every 2 ns. For that, a technique very similar to the stroboscopic effect of periodic motion, also known as the "wagon-wheel effect", is used. The acquisition principle for the time-resolved measurements is schematically depicted in Fig. 3.5. Exemplarily the stationary motion of a magnetic vortex excited at $T_{\text{exc}} = 200$ MHz is regarded. Although the synchrotron provides a sampling interval of $T_{\text{flash}} = 2$ ns, the example presented in Fig. 3.5 features a time resolution of $\Delta t = 1$ ns between two subsequent frames of the captured movie. This can be realized since the vortex gyration is periodically repeated every 5 ns and thus the time-frames do not necessarily have to be captured in one gyration period but can be composed from several identical excitations. This, in principle, allows for an infinitely small Δt when the sampling interval T_{flash} and the periodicity of the gyration T_{exc} have no common multiple. In this hypothetical case, every time state of the gyration would be imaged exactly once assuming an infinite acquisition time. In reality the period of excitation T_{exc} and the flash interval T_{flash} must have a least common multiple with:

$$n_p \cdot T_{\text{exc}} = n_c \cdot T_{\text{flash}}, \quad n_p, n_c \in \mathbb{N} \quad (3.1)$$

since typically only one photon per flash is transmitted through the sample and thus the measurement has to be repeated many times for every unique dynamical state in order to obtain a sufficient signal-to-noise ratio. The number of unique dynamical states that

³The spatial resolution of the microscope depends on the zone plate in use. A resolution of 10 nm has been demonstrated for a similar setup with another zone plate. [Cha12]

3. Experimental Methods

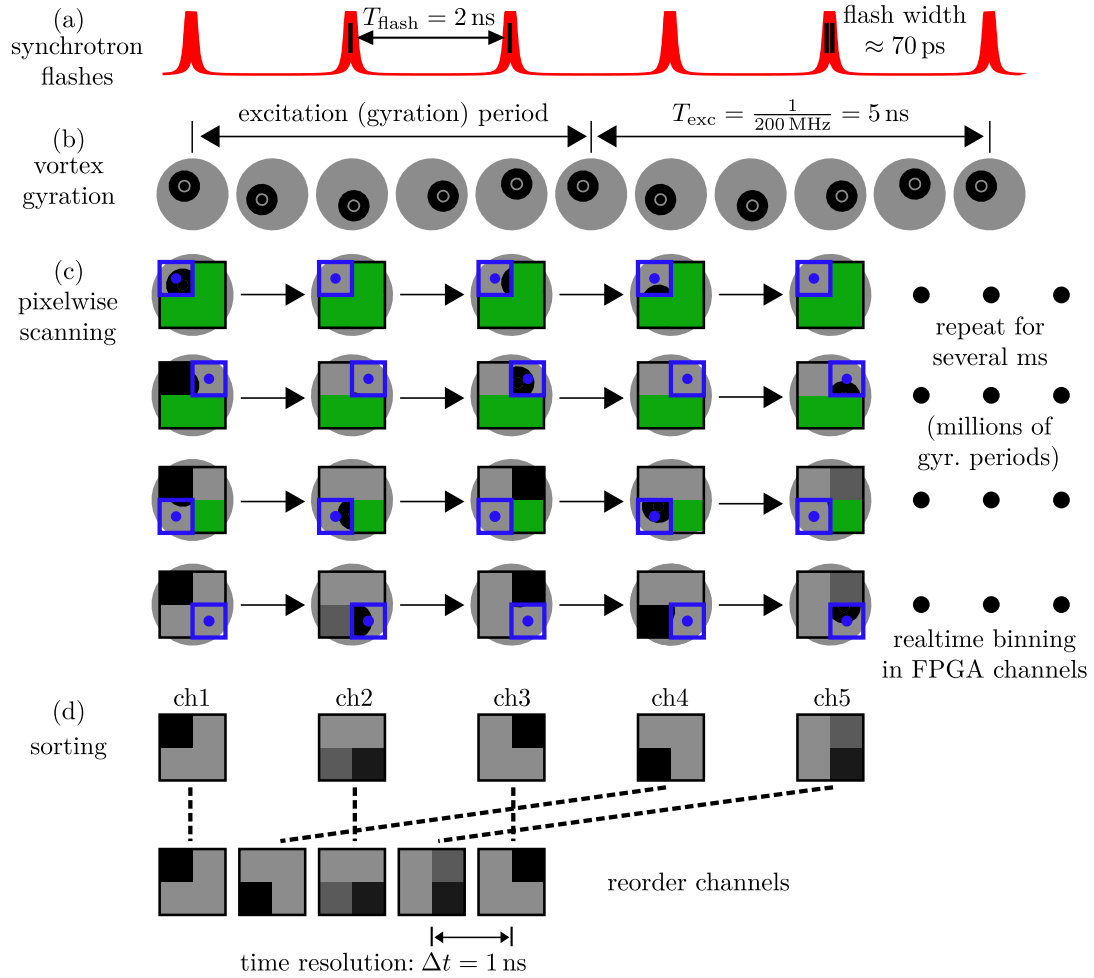


Figure 3.5.: Schematic of the capturing process of the MAXYMUS microscope. (a) Synchrotron flashes with a width of about 70 ps arrive every 2 ns. (b) The stationary motion of the vortex gyration is excited by a homogenous alternating magnetic field applied to the disk containing the vortex. The frequency of the excitation and the resulting gyration is chosen to be 200 MHz. The vortex core is schematically depicted as a large black dot in a gray circle (disk). The gyration repeats every 5 ns. (c) Pixel wise scanning of a micrograph with 2×2 pixels. Uncaptured pixels are depicted in green. The currently captured pixel is bold-framed in blue. The X-ray beam is depicted as a blue dot in the center of the disk. The photon count detected by the APD accounts for the transmission in an area of the size of the X-ray spot. For each photon flash the transmission through the currently captured pixel is measured. This process is repeated for several milliseconds until the scanning proceeds to the next pixel. The recorded absorptions are attributed to the unique dynamical states by realtime binning performed with a FPGA circuit. (d) The $n_c = 5$ channels of the FPGA are reordered in order to obtain a movie of one excitation period.

are distinguished from each other (called *channels* in the following) is labeled n_c , and n_p denotes the number of excitations periods per cycle and per channel. Consequently after n_p excitation periods or n_c X-ray flashes the same dynamical state is captured again. In the example depicted in Fig. 3.5 this yields $n_p = 2$ and $n_c = 5$. The transmission is measured via the APD for every photon flash and has to be assigned to the corresponding time-step (channel). This is realized with the electronics developed by Van Waeyenberge *et al.* based on a so-called field-programmable gate array (FPGA) [VWa06]. In order to obtain a sufficient time-resolution for the stationary motions typically a pixel-size of $10 \text{ nm} \times 10 \text{ nm}$ and an exposure time of 15 ms to 50 ms is used for the samples in standard-geometry. The sampling process is performed pixel wise. This is depicted in Fig. 3.5(c) for the simplified case of four image pixels. Each pixel is exposed to the synchrotron light individually, yielding the information for the whole movie of this pixel. During the exposure millions of gyrations are performed. Subsequently the next pixel is acquired. This is contrary to movies captured with a common video camera or time-resolved measurements at so-called full-field microscopes where the acquisition is performed frame-wise instead of pixel wise. The resulting video frames correspond to FPGA channels. After the acquisition the channels are reordered in order to obtain a movie of one single excitation period (see Fig. 3.5(d)). The resulting time resolution Δt is improved with a higher number of channels. In this work the limiting factor for the time resolution has never been the maximal number of channels of the FPGA but always a sufficiently large exposure time per pixel. Typically between 20 and 60 channels have been used to image the stationary motion. It is also possible to detect the relaxation of vortices after a pulsed excitation. For that the excitation is periodically repeated and the movement is captured for several gyration periods. For such measurements a larger number of channels has to be used in order to sufficiently sample the gyration. The photon count detected by the APD accounts for the transmission in an area of the size of the X-ray spot (blue dot in Fig. 3.5(c)). For the measurements presented in this work the spot-size is about 30 nm according to the acquisition software and thus larger than the pixel-size. Consequently, the vortex core is enlarged in the captured data.

Figure 3.6 exemplarily depicts single time-frames of a movie recorded with the MAXYMUS microscope. As can be seen from the micrograph in Fig. 3.6(a), the absorption is mainly given by the different materials. The eight permalloy disks that are arranged in a ring can be seen in black since the absorption is high with respect to the membrane (Si) and the stripline (Cu) that is placed above the bottom most disk (disk 0). The magnetic contrast is superimposed and can be emphasized by a more sophisticated color-scale

3. Experimental Methods

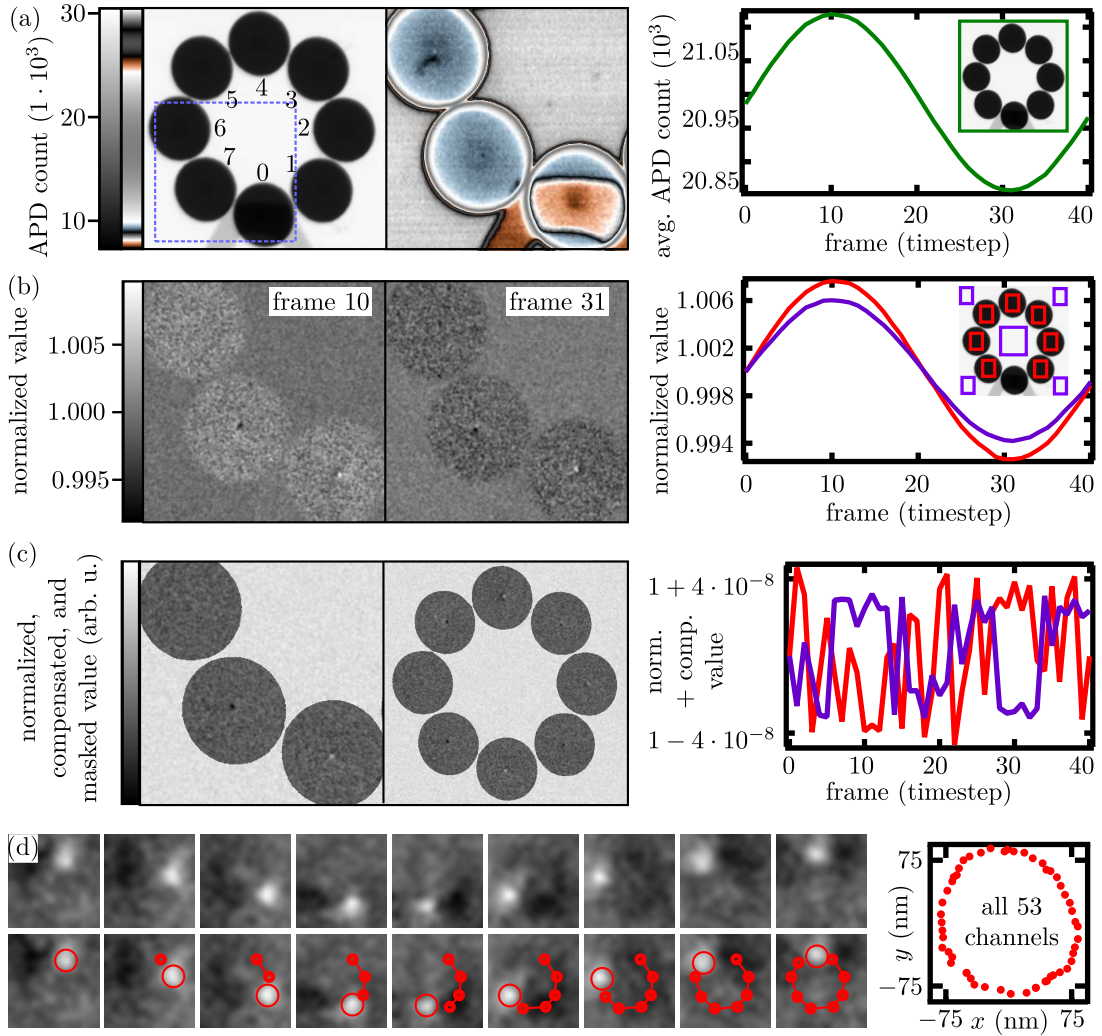


Figure 3.6.: Scanning transmission X-ray micrographs with different levels of image processing. All images correspond to one time-frame of the captured movie. (a) Raw image. Left micrograph: Linear color-scale with numbering of the disks. Right image: Detail of disks 0, 6, and 7 with complex color scale. Graph: Average photon count of the avalanche photo diode for all 41 frames of the captured movie. (b) Micrographs: Two normalized image frames. Graph: average values of the normalized movie for different intensity levels of the raw movie. According to the inset, the purple curve corresponds to the background level and the red curve depicts the disk areas. The disk areas show a higher variation leading to a blinking of the different areas in the movie. (c) Micrograph: Masked image with compensated blinking. Graph: The normalized values do not differ in intensity any more. (d) Micrographs: $250 \text{ nm} \times 250 \text{ nm}$ details of a vortex core region for different time frames. The vortex core appears as a white dot that rotates clockwise. Graph: All 53 frames of the movie reveal the vortex trajectory.

used in the right micrograph of Fig. 3.6(a). The disks now have bluish colors and the stripline-absorption levels are depicted in orange. The top disk in this detail (disk 6) features white contrast for a vortex core and the middle disk (disk 7) shows an opposite core polarization (black spot). Gaussian filtering (in time and space) has been applied to the micrograph to improve the visibility of the cores but nevertheless they can hardly be seen. This is due to the superimposed material contrast. A black impurity disguises the vortex core in disk 6. Likewise, it is almost impossible to see the white vortex core under the stripline in disk 0. The latter is due to carbon residues that stem from a previous scan in the center region of the disk. Those can be seen as a darker area at the center of the disk. There are two major approaches to improve the visibility of the core polarizations. For single (static) images it is a common approach to acquire a second image with opposite X-ray polarization and subtract the two images. Consequently, only the magnetic contrast remains. This is a very time-consuming process since two images have to be recorded and the undulator has to be moved in order to change the polarization of the light. For movies it is reasonable to use another approach, since the dynamic magnetic contrast can be isolated from the static material contrast with the following technique, the so-called *normalization*. Such image-processing can be done subsequent to the beam time and thus is not time-critical. The normalization is commonly done by first dividing each frame by its average (*flattening*) and then dividing each pixel by its time average. Ideally the resulting images only feature the changes in magnetic contrast within the disk. Figure 3.6(b) depicts the normalized micrograph for two movie frames (FPGA channels). The stripline and the carbon residues over disk 0 cannot be seen any more revealing white contrast for the core polarization. Disk 7 still shows a black vortex core but the core of disk 6 cannot be seen anymore. This is due to the impurity (see Fig. 3.6(a)) that pins the magnetic vortex core. In the experiments the surface roughness of the disk affects the excitability so that a threshold amplitude of the excitation has to be overcome in order to activate the gyration. Consequently, the vortex in disk 6 does not move and does not contribute to the dynamics depicted in the normalized image. Thus, vortices that do not move can only be seen in the direct image and not in the normalized one. Additionally note that the disks can still be seen in the normalized images. For an ideal normalization this would not be the case since, despite a negligible drift of the sample, the disks do not move and thus do not yield dynamic contrast. The two micrographs in Fig. 3.6(b) reveal that the color of the disks with respect to the color of the membrane background depends on the frame number. In frame 10 the disks are brighter than the background and vice versa for frame 31. This effect can be understood as beneficial for the comprehension

of the images presented here but strongly hinders the evaluation of other measurements, especially for a pulsed excitation. It can be understood when regarding the overall image intensity (average APD count) of the movie frames. As can be seen in the graph in Fig. 3.6(a) the intensity alternates in a sinusoidal fashion. This is due to a crosstalk of the signal sent through the stripline and the avalanche photo diode (APD). For pulsed excitations the pulse and its reflections can clearly be seen in the average APD count. For a sinusoidal excitation the intensity alternates in the way shown in Fig. 3.6(a). In order to prevent a flickering of the normalized movie the flattening, i.e., dividing the frame by its average, is performed prior to the actual normalization of the dynamic contrast, i.e., dividing every pixel by its time average. The flattening leads to the contrast change depicted in Fig. 3.6(b). Due to a small nonlinearity of the APD diode, the crosstalk has a different influence on the signal of the disks than on the signal of the membrane. This can be seen in the graph in Fig. 3.6(b). The intensity variation of the normalized image contrast is different for the disks (red line) than for the membrane background (purple line). The disks "blink" in the movie. When the different effects of the crosstalk on areas with different APD-count levels are taken into account prior to the flattening process, the blinking can be subtracted out. Such process has been developed in the context of this work and is called *compensation* in the following. The graph in Fig. 3.6(c) shows the normalized APD count for the disk areas and the membrane area after the compensation. One can see that the blinking has been subtracted out and only a noise-like fluctuation of the intensity remains. For that, the nonlinearity of the APD is first characterized by the graph presented in Fig. 3.6(b), depicting the average photon count for areas with different intensity levels, i.e., for the disks and the membrane areas. From this, a correction factor for the APD-count can be calculated for each time step by linear interpolation between the purple and the red line. After the correction is applied to every pixel of the movie, the process is repeated iteratively until an adequate reduction of the blinking is achieved (see Fig. 3.6(c)). The compensation is exceptionally beneficial for measurements with pulsed excitations that are not in the focus of this thesis. The compensation routine has been acknowledged in the work of Falk Stein *et al.* in Ref. [Ste14] on the direct observation of internal vortex domain-wall dynamics. Since pulsed excitations are used, the crosstalk had strongly disguised the magnetodynamics before the compensation was performed (see appendix A.4). For the measurements presented here, it is more comprehensive to see the disks in the movies. A compensation is not crucially important. To make the image even more comprehensive, the disk structure is superimposed as a mask to the normalized and compensated image depicted in Fig. 3.6(c). One can now guess from the

images depicted in Fig. 3.6(c) that the vortices show alternating polarizations from disk to disk. One has to keep in mind that the vortex core in disk 6 cannot be seen in the normalized image and has been accounted white in Fig. 3.6(a). Additionally note that for the determination of the core polarization not only single frames are used but the whole movie showing a gyration of the vortex core around the center of the disk. A detail of a core region for different time-steps is shown in Fig. 3.6(d). The vortex core appears as a white spot that rotates clockwise. Thus, the polarization of the core is $p = -1$. In this way it can be clearly determined from the movie that the ring shows an alternating polarization pattern. This has been tuned via indirect self-organized state-formation that will be presented in the next chapter.

In summary, rather complex image processing techniques allow to accentuate the vortex cores in large overview images of the sample. Moving vortices show strong contrast in normalized images. Static vortices can only be seen in the direct image that is superimposed with material contrast. Especially impurities of the sample and carbon depositions due to previous scans impair the quality of the direct image. In order to improve the quality of the STXM movies a routine to compensate the nonlinearity of the APD that results in a blinking of areas with different contrast levels has been developed. This routine was exceptionally beneficial for measurements with pulsed excitations, like presented by Falk Stein *et al.* in Ref. [Ste14] (see appendix A.4). From the static images presented in Fig 3.6(a) to (c) one can already presume that the vortices show alternating polarizations along the ring. When using the gyration direction in the full movie, this is substantiated. The polarization clearly follows from the gyration direction regardless of the actual color scale or possible relics of the image processing techniques. Actually, large overview scans as presented in Fig 3.6(a) to (c) are the exceptional case due to the long acquisition times. For most measurements only the center regions of the disks are scanned as depicted in Fig 3.6(d). The graph on the right shows the vortex trajectory obtained by manually evaluating the vortex core positions for all 53 frames of the movie (channels). Such evaluations yield the polarization of the core (main topic of chapter 4) and a precise measurement of the stationary motion (main topic of chapter 5). The stationary motion can also be investigated with the ferromagnetic absorption spectroscopy setup that is presented in the following section.

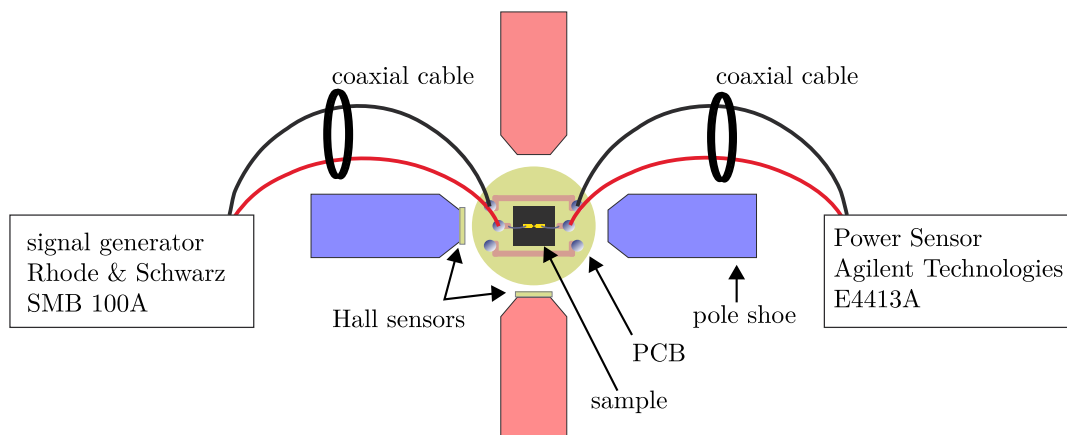


Figure 3.7.: Schematic of the setup for ferromagnetic absorption measurements. A high-frequency (a few 100 MHz) alternating current is generated and sent through the stripline placed above the microstructures on the sample. The transmitted power is measured. Two measurements are performed for each point of the absorption. In the reference measurement a strong magnetic field is applied via the pole shoes that annihilate the magnetic vortices. In the second measurement vortices are nucleated and the measurement is repeated. The difference of the two measurements yields the absorption depicted in Fig. 3.8(b).

3.3. Ferromagnetic Absorption Spectroscopy

The experimental setup for the ferromagnetic absorption spectroscopy (FMR) is situated at room atmosphere and is much simpler than the STXM setup. It consists of only a few components depicted in Fig. 3.7. The sample is mounted on a printed circuit board (PCB) that is connected via coaxial cables to a signal generator, on the one side, and a power sensor on the other. Thereby a signal can be sent through the stripline that is prepared above an ensemble of microstructures. When the stationary vortex gyration is excited by the Oersted field that is generated by the alternating current sent through the stripline, the transmission through the stripline is reduced since a small part ΔP of the input power is used to maintain the damped dynamics. The absorbed power ΔP is proportional to the sum of the velocities of the vortices $\sum_i \dot{\vec{x}}_i$ [Dre09; Kam11]. The average squared velocity $\frac{1}{N} \sum_i \dot{\vec{x}}_i^2$ has already been discussed as the frequency response of the system in the last chapter. In the following the two words "absorption" and "frequency response" will be used interchangeably. The prefactor $\frac{1}{N}$ is of no interest since the absorption will always be discussed in arbitrary units in this work. To extract the absorption ΔP a reference measurement is used where the sample is magnetically saturated by a strong external magnetic field ($\mu_0 H_{\text{ext}} > 60 \text{ mT}$) generated by magnetic coils with pole-shoes depicted in

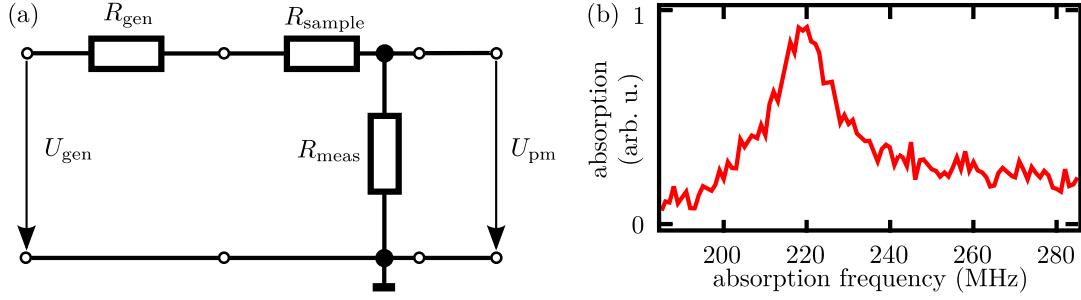


Figure 3.8.: (a) Equivalent circuit diagram of the ferromagnetic-absorption measurement-setup. The internal resistance of the power generator R_{gen} and the measurement resistance of the average power sensor are 50Ω . The sample resistance is only approximately adjusted to the wave resistance 50Ω . For the widest striplines of several μm the resistance of the sample accounts for $R_{\text{sample}} \approx 10 \Omega$ and $R_{\text{sample}} \approx 100 \Omega$ for the most narrow striplines of 800 nm in width. Such variation in the resistance is not critical due to the relatively low measurement frequencies of 200 MHz to 400 MHz .

Fig. 3.7. In this state no dynamics are expected, except for spin waves at high frequencies above 1 GHz . The reference power varies with the frequency and also because of variations of the temperature. Thus reference measurements are repeated after every change of the excitation frequency or after a time of several minutes. In Fig. 3.8 the equivalent circuit diagram of the setup and a sample absorption measurement are depicted. The resonance frequency of the shown absorption lies at about 220 MHz . The absorption is calculated with the described proceeding by the difference of two power measurements. The scale is given in arbitrary units.

The amplitude \tilde{H} of the Oersted field generated by the current \tilde{I} sent through the stripline can be estimated by

$$\tilde{H} \approx \frac{\tilde{I}}{2w} \quad (3.2)$$

according to Ref. [Sil99]. Whereas the microstructures lie directly beneath the stripline with width w . The efficiency of excitation strongly depends on the excitation frequency. In resonance 45 A m^{-1} can be enough to switch vortex polarizations. Lower field strengths are used to non-invasively measure the absorption of the vortices. For high powers the vortices reach high velocities and undesirably switch their polarizations during the absorption measurement.

4. Self-Organized State Formation in Magnonic Vortex Crystals¹

As introduced in Chapter 2, the coupling in arrangements of magnetic vortices strongly depends on the relative polarizations of the vortex cores. In this chapter we present a mechanism, called *self-organized state formation* (SOSF) that allows to tune the polarization configuration in various kinds of vortex arrangements by the temporary application of magnetic fields. This allows for the manipulation of the properties of (large) regular arrangements of magnetic vortices that will be addressed as *magnonic vortex crystals* in the following. In this chapter we will first introduce the phenomenon of self-organized state formation for rectangular crystals consisting of 3×3 vortices. Parts of those findings are also presented in the publications [Ado13; Sto15]. Subsequently, different aspects of the self-organized state formation are examined on various types of magnetic vortex arrangements including larger magnonic crystals with more than 100 vortices. The self-organized state formation builds the basis for the manipulation of the crystal properties, e.g., band-structure engineering, and for the experiments presented in chapter 5.

Figure 4.1 illustrates the setup of the first experiment. The vortices are excited by a harmonic field generated by a high frequency current applied to a stripline in coplanar waveguide geometry above the 3×3 disk-array. The disks have a diameter of $2 \mu\text{m}$ and a height of 60 nm (standard geometry). The center-to-center distance amounts to $2.25 \mu\text{m}$ and $3 \mu\text{m}$, respectively for two different sample types. Measurements are performed at the MAXYMUS beamline at BESSY II in Berlin, Germany. At first the whole crystal is

¹Parts of this chapter have been published in Ref. [Ado13] – “Self-organized state formation in magnonic vortex crystals” by Christian F. Adolff, Max Hänze, Andreas Vogel, Markus Weigand, Michael Martens, and Guido Meier. Copyright 2013 by the American Physical Society. – as well as in the review article Ref. [Sto15] – “Imaging Spin Dynamics on the Nanoscale using X-Ray Microscopy” by Hermann Stoll, Matthias Noske, Markus Weigand, Kornel Richter, Benjamin Krüger, Robert M. Reeve, Max Hänze, Christian F. Adolff, Falk-Ulrich Stein, Guido Meier, Mathias Kläui, Gisela Schütz.

4. Self-Organized State Formation in Magnonic Vortex Crystals

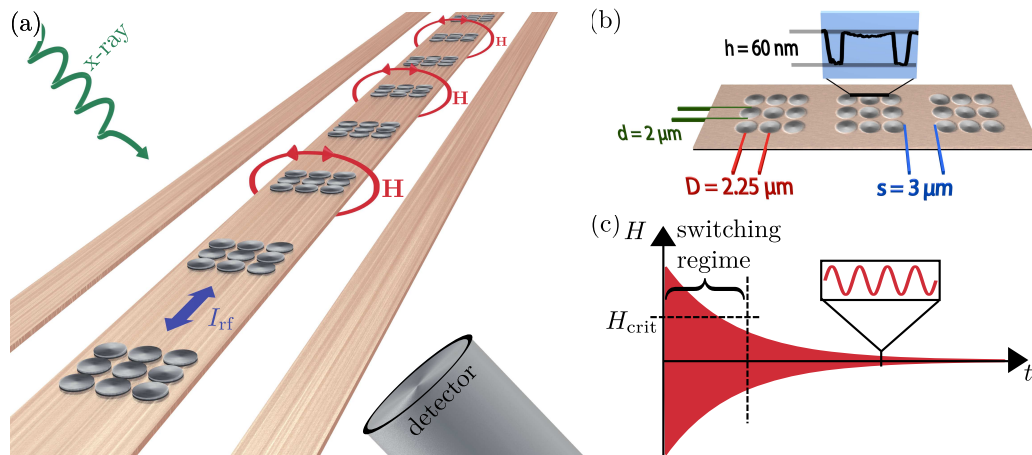


Figure 4.1.: Experimental setup. (a) Vortex arrays investigated with transmission soft X-ray microscopy. The magnetic field \vec{H} is applied via an alternating current sent through a coplanar waveguide. (b) X-ray micrograph with in-plane contrast of three vortex arrays that comprise nine nanodisks each. The magnetization curls in plane around the center of each disk (thickness $h=60$ nm, diameter $2R=2$ μm , distance $D=2.25$ μm). The inset shows a line scan of an atomic force micrograph and reveals the topography of the disks. (c) Form of the magnetic field excitation used to tune the polarization states. The amplitude of the unidirectional harmonic excitation is reduced adiabatically until vortex core switching ceases.

strongly excited by an alternating unidirectional magnetic field that causes all the vortices to permanently switch their polarizations. The field amplitude is then reduced quasi statically (millisecond time scale) with respect to the periodicity of the vortex gyration (nanosecond time scale). As depicted in Fig. 4.1(c), starting from above the switching threshold, the amplitude of the harmonic excitation is reduced until switching dies out. In a second step, the polarizations of the vortices are determined by evaluating the sense of gyration. For this, a harmonic field of decreased amplitude is applied to non-invasively detect the created polarization state. For the determination of the polarization states, e.g. for 245 MHz a time period of 4.08 ns is detected in steps of 80 ps. We find the vortices organized in preferred polarization states depending on the frequency of the primary excitation.

Since the process of switching itself cannot be investigated in the experiment, additional micromagnetic simulations have been performed (see Appendix A.5). Those reveal that the vortex polarizations in an array of disks switch rather randomly at high amplitudes of a harmonic field that is applied to all magnetic vortices in the array. At intermediate

field amplitudes the switching stops when certain stable polarization configurations are reached eventually. The stability of such polarization states can be understood with the theory presented in chapter 2. As described there, magnetic vortices couple in the manner of harmonic oscillators, whereas the coupling strength depends on the distance between the magnetic nanodisks containing the vortex cores [Vog11; Shi03; Jun11; Sug11]. When the center-to-center distance between the disks exceeds twice the diameter ($\frac{D}{2R} > 2$), the coupling can be neglected [Mej06; Vog10]. Random polarization states should emerge, independent of the excitation amplitude. Maximal coupling can be obtained by reducing the center-to-center distance between the disks until it equals the disk radius and the disks merge into a single structure ($\frac{D}{2R} = 1$). Smaller distances lead to exchange interaction at the intersection of the disks and will not be regarded here [Jai12]. We experimentally investigate two types of samples of spatially separated disks with different center-to-center distances. The disk-arrays of type 1 have a center-to-center distance of $3 \mu\text{m}$ ($\frac{D}{2R} = 1.5$). For samples of type 2 the center-to-center distance of the disks is reduced to $2.25 \mu\text{m}$ ($\frac{D}{2R} = 1.125$) so as to obtain a stronger dipolar coupling [Vog11; Vog10].

At first the results on samples of type 1 are discussed since they comprise the more simple interaction due to their lower coupling strengths. Figure 4.2(a) summarizes the resulting polarizations states that occur after the adiabatic field reduction with different frequencies. For a frequency of $f_1 = 225 \text{ MHz}$ the polarization is constant along the field direction and alternates in the perpendicular direction. Columns of constant polarization occur. In contrast, rows of constant polarization occur at two higher frequencies, i.e., $f_2 = 245 \text{ MHz}$ and $f_3 = 255 \text{ MHz}$. When excited at $f_4 = 235 \text{ MHz}$ no state could reproducibly be tuned for repeated measurements on the same crystal. This can be understood with the simplified dipolar stray-field coupling presented in section 2.2.2. A 3×3 vortex crystal may be formed from pairs of horizontally and vertically coupled vortices as building blocks. In the experiments all disks in the crystal and thus all interacting pairs are excited with the unidirectional field in y -direction, regardless of the orientation of the pair. In addition the crystals show a large disk interdistance of $3 \mu\text{m}$ so that the coupling can be considered relatively weak. Thus, the motions tend to be dominated by the external field. This idealized model system is described with Eqn. 2.32. It reveals that for a pair of vortices with alternating polarizations ($p_1 p_2 = -1$) the variation of the absorption peak $\omega_{p,\text{alt}}$, where the pair can be excited most efficiently, is proportional to the cosine of twice the angle ϑ between the x -axis and the connecting line of the two disks. Thus, in the alternating case, a pair that is placed perpendicular to the field direction ($\vartheta = 0$) can be excited most efficiently at a higher frequency than an

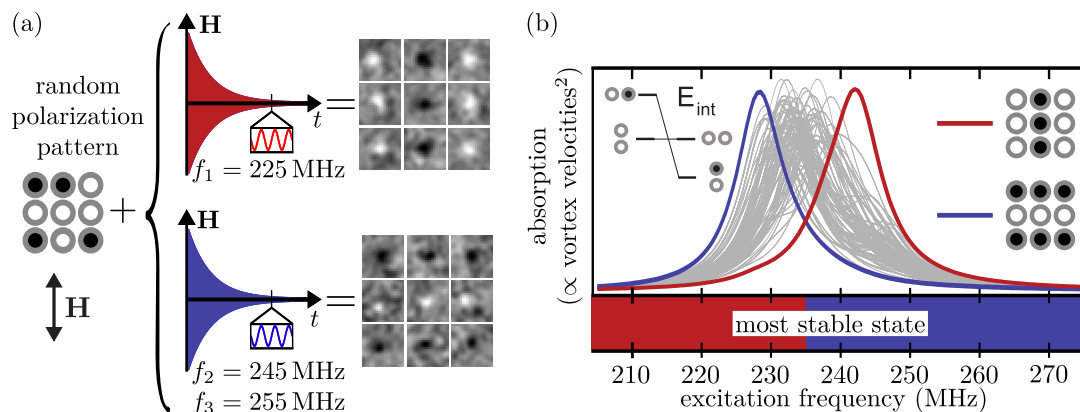


Figure 4.2.: SOSF in 3×3 crystals of type 1 ($\frac{D}{2R} = 1.5$). (a) Experiment. A variation of the frequency of the adiabatically reduced field excitation tunes differently ordered polarization states. For $f_1 = 225$ MHz columns of constant polarization occur, and rows of constant polarization emerge at $f_2 = 245$ MHz and $f_3 = 255$ MHz. No pattern could reproducibly be tuned at $f_4 = 235$ MHz. (b) Numerical calculations. Absorption profiles of all $2^9 = 512$ possible polarization states numerically calculated in the extended Thiele model ($\omega_0 = 238$ MHz, $\Gamma = 26 \cdot 10^6$ s $^{-1}$, $s = 0.6875$). The states of rows (blue) and columns (red) of constant polarization are highlighted. The bottom color scale depicts the most stable state, i.e., the state with the lowest absorption at a particular frequency. Those states are predicted to be tuned via SOSF. The inset in the upper-left corner schematically depicts Eqn. 4.1. The interaction energy (absorption frequency) in a pair of disks varies for different alignments of the pair and the core polarizations.

identical pair that is aligned parallel ($\vartheta = \pi/2$). In the case of homogeneous polarizations ($p_1 p_2 = 1$), the frequency of the most efficient excitation $\omega_{p,\text{hom}}$ does not depend on the rotation angle ϑ and lies in between the above two frequencies (see also Fig. 2.9(d)). This leads to the relation

$$\omega_{p,\text{alt}}(\vartheta = 0) > \omega_{p,\text{hom}} > \omega_{p,\text{alt}}(\vartheta = \frac{\pi}{2}) \quad (4.1)$$

that is schematically depicted in the inset of Fig. 4.2(b). Such eigenmodes with identical phases do also exist in the 3×3 crystal with the two regarded polarization patterns [Hän14]. Hence, the pairwise interaction energies in Eqn. 2.30 simply add up to the total peak offset $\omega_p - \omega_{\text{iso}}$. Note that all pairs of second-next neighbors ($\vartheta = \pi/4$) have alternating polarizations. Accordingly, they have no influence on the peak offset ($\cos(2 \frac{\pi}{4}) = 0$). Consequently, the state with columns of equal polarization has a higher frequency $\omega_{p,\text{col}}$ of most efficient excitation than the state with rows of constant polarizations ($\omega_{p,\text{row}}$), since the column state exhibits the alternating pairs perpendicular to the

field excitation ($\vartheta = 0$). Thus

$$\omega_{p,\text{row}} < \omega_{p,\text{col}} \quad (4.2)$$

applies. This can also be seen in the numerical calculations presented in Fig. 4.2(b). There, the absorptions for all $2^9 = 512$ polarization states have been calculated numerically using the extended Thiele model presented in section 2.2.1. The emerging states are highlighted in red (column state) and blue (row state). As predicted from the analytical approach, the state with rows of constant polarization can be excited more efficiently at lower frequencies than the state with columns of constant polarization. When a state is excited efficiently, the vortices in the crystal reach high velocities. At a critical velocity of about 250 m s^{-1} [Mar13] the vortices switch their polarizations and thereby lead to another polarization state in the crystal. Thus, efficiently excitable states are less stable than states that cannot be excited efficiently at a particular frequency. One can see in Fig. 4.2(b) that the emerging states indeed are the least efficiently excitable states at the corresponding frequencies f_1 , f_2 , and f_3 of the adiabatically reduced field excitation. This can easily be motivated using the relations presented above. The adiabatic field reduction passes a critical field amplitude where only one polarization state will not switch. This least excitable state is eventually adjusted after several switching processes between instable polarization states. The two states of rows and columns of constant polarizations take turns in being the most stable states for frequencies below or above a transition frequency $f_{\text{trans}} \approx 235 \text{ MHz}$ where they are equally excitable. This explains why no state could reproducibly be tuned at the frequency $f_4 = 235 \text{ MHz}$ that is close to the transition frequency.

In conclusion, we have shown that the polarization states that emerge after a self-organized state formation with adiabatic field reduction can be predicted from the comparison of all possible absorptions in the crystal. Those have been numerically calculated for all 512 polarization states².

Using the simplified analytical approach one can estimate the transition frequency ω_{trans} , where the states with rows or columns of constant polarizations are equally excitable. For that it is the most simple approach to assume identical Lorentzian peak functions that are shifted by ω_p to model the absorption. This can be done since the 3×3 crystals show an eigenmode that resembles the enforced phase relation of the exciting magnetic

²Note that only 136 polarization states are non-degenerate with respect to the frequency response (absorption) due to symmetry reasons.

field for the pattern of rows or columns of constant polarization [Hän14]. It follows

$$\omega_{\text{trans}} - \omega_{\text{iso}} = \frac{1}{2}(\omega_{p,\text{col}} + \omega_{p,\text{row}}) = \omega_{\text{iso}} - \frac{\omega_{p,\text{col}} - \omega_{p,\text{row}}}{6}. \quad (4.3)$$

Thus, the transition frequency ω_{trans} is slightly below the frequency of the isolated disk. This is in good accordance with the experiments since ω_{iso} is determined to be approximately 238 MHz for the investigated sample (see appendix A.2). The results presented in Fig. 4.2 are based on the more complex numerical simulations, since the analytical model does not include deviations of the resonances from Lorentzian peak functions. Those deviations occur when several eigenmotions of the crystal are excited at the same frequency. Due to damping this can occur even when the eigenfrequencies are non-degenerate. In the weak coupling case with rows or columns of constant polarizations this effect can be neglected since the external field only excites the eigenmode with equal phases $\varphi_i = \varphi$. Stronger coupling allows for the vortex motions to diverge from this enforced relation. The motion can be understood as a superposition of several eigenmodes. Consequently, the absorption curves are distort. This can be seen in the calculations for the experiments on the crystals of type 2 that exhibit a smaller center-to-center distance of the disks ($\frac{D}{2R} = 1.125$). Figure 4.3 (a) shows the numerically calculated absorption profiles for the experiments performed in the strong-coupling regime. One can clearly see that the peaks do not have a Lorentzian form. The numerical calculations leads to seven non-degenerate polarization states that are most stable, i.e., least efficiently excitable, at least at one frequency. The profiles of those states are colored in Fig. 4.3 (a). Experiments have been performed in the range between 225 MHz and 265 MHz. The calculations for this frequency range are depicted in detail in Fig. 4.3 (b) together with the experimentally tuned polarization states. One can see that the measured states are predicted correctly. Note that the measured behavior is very reproducible³. The measurement at 225 MHz has been performed for five additional crystals of the same geometry, always yielding the same polarization state of columns of constant polarization. The state that emerges at 245 MHz could be confirmed for three of four further crystals. Only one crystal showed the state where all disks have the same polarization, which is the second most stable state near this frequency. At a frequency of 235 MHz two additional crystals yield the states neighboring the predicted states (colored green and cyan in Fig. 4.3 (b)). These slight deviations from the theory might be due to imperfections in the preparation process. Measurements of several isolated vortices of the same preparation process revealed

³For a complete listing of all measured polarization states see appendix A.6

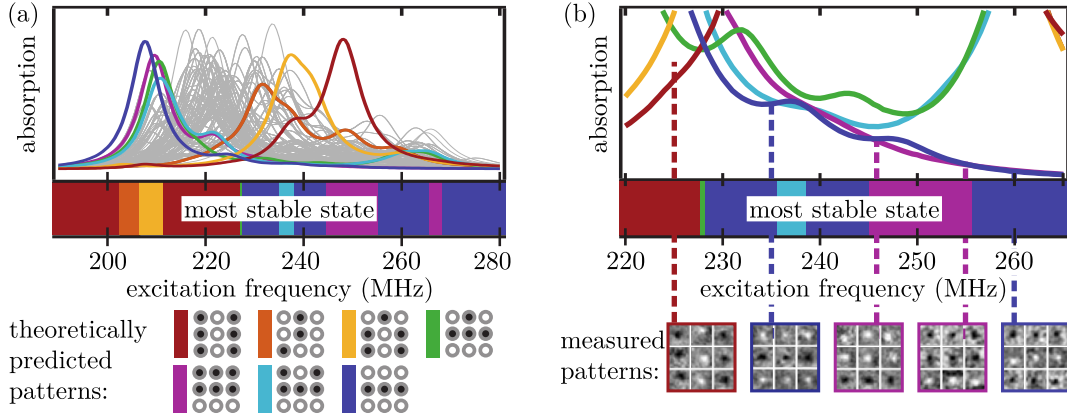


Figure 4.3.: SOSF in 3×3 crystals of type 2 ($\frac{D}{2R} = 1.125$). (a) Numeric calculation of the absorption profiles of all $2^9 = 512$ possible polarization states. Due to the strong coupling the absorption profiles are not Lorentzian peak functions. This allows for 7 different states to be tuned via SOSF. Those stable states are highlighted with colored solid lines. The bottom color scale depicts the most stable state, i.e., the state with the lowest absorption at a particular frequency. Those states are predicted to be tuned via SOSF. (b) Experimental results (bottom) in comparison with the numerical calculation (top graph). The dashed vertical lines depict the measurement frequencies. The three not degenerated polarization patterns (color of frames/lines) are correctly predicted for the five measurement frequencies.

that the resonance frequency of the vortices deviates about ± 15 MHz from disk to disk. Thus, the adjusted states can slightly vary depending on the investigated crystal on the sample. Nevertheless all crystals behave approximately identical. This can also be seen in the high-frequency absorption measurements presented in Fig. 4.4. For that additional samples with up to 60 identical 3×3 vortex arrays are prepared on silicon oxide wafers. Ensembles of both array types ($\frac{D}{2R} = 1.5$, $\frac{D}{2R} = 1.125$) are prepared in this way. The high-frequency absorption measurements allow to perform more measurements in a shorter time and give insight into the reproducibility of the state formation in the ensemble of crystals. The y -axes represent the state formation frequency f_{state} used to tune the polarization states as described above, and the x -axes account for the frequency of the absorption spectrum f_{abs} of the emerging polarization patterns. The absorption is represented by the given color code. One can see that the absorption profiles vary for different state-formation frequencies. It is straight forward to expect that the absorption signal measured after a specific state formation stems from crystals that are settled to the most stable polarization state. Thus, the absorption profile of the state that is least efficiently excitable at the state-formation frequency f_{state} is expected. Consequently, the expected absorptions can be calculated in the Thiele model and are depicted below the absorption

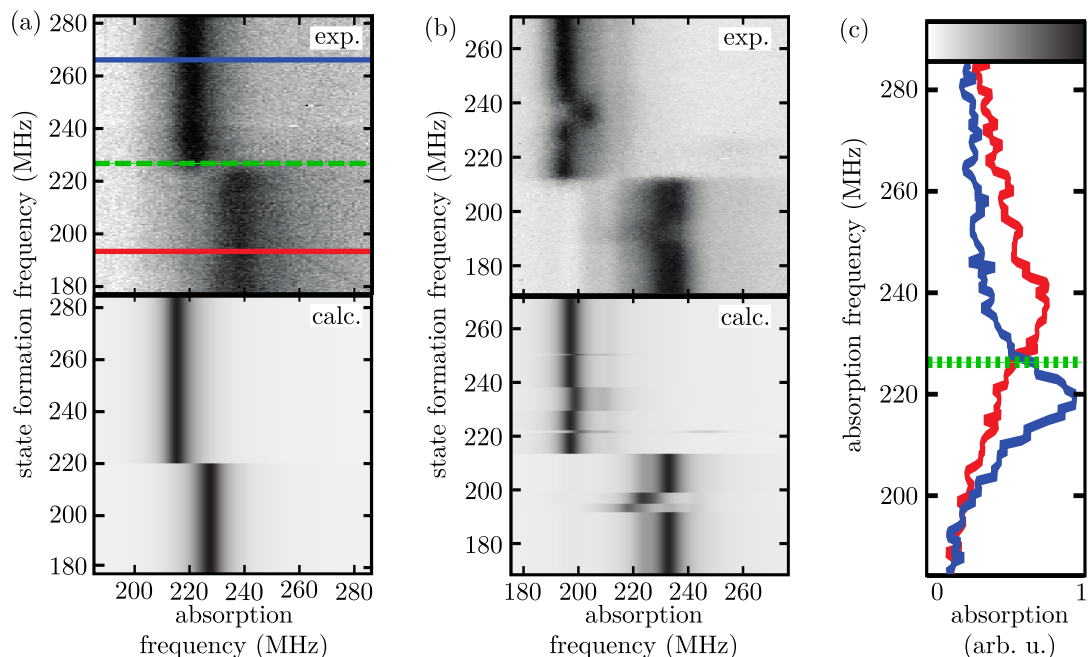


Figure 4.4.: High-frequency absorption (FMR) measurements and absorptions predicted via numerical calculations. (a) weakly coupled samples ($\frac{D}{2R} = 1.5$, type 1). Top graph: experiment. Bottom graph: numerical calculation. The solid horizontal lines highlight the position of the absorption profiles depicted in (c). The dashed green line depicts the transition frequency determined from (c). (b) strongly coupled samples ($\frac{D}{2R} = 1.125$, type 2). Top graph: experiment. Bottom graph: calculation. (c) Absorption profiles of the two tunable polarization states (rows, columns of constant polarization) that intersect at the transition frequency $f_{\text{trans}} = 226$ MHz.

measurements in Fig 4.4(a) and (b), for the two sample types respectively. Due to small variations in the preparation process, especially the change of substrate, the physical properties of the samples slightly differ from those determined for the samples used for the X-ray microscopy. Parameters of the theoretical predictions are fitted with variations of about 10% compared to previously determined parameters. They can be found in appendix A.2. The theoretical prediction is calculated under the assumption that the ensemble completely settles in the state that is most stable at the state-formation frequency. By comparing theoretically and experimentally obtained absorptions one can see that this approximation is valid, although the absorption profiles are broadened with respect to the calculations due to the variations in the ensemble mentioned above. Figure 4.4(c) depicts two example absorptions for the ensemble of the weakly coupled crystals that substantiate the presented stability criterion. The two absorption profiles are assumed to correspond to the only two states, i.e., rows and columns of constant polarizations, that can be tuned

for the weakly coupled sample type. The absorption intersect at around 226 MHz. At this frequency the most stable state should change according to the presented stability criterion, yielding the transition frequency $f_{\text{trans}} = 226$ MHz. When compared with the absorption measurement in Fig. 4.4(a), indeed the form of the absorption changes at this frequency. Additionally note that in Fig. 4.4(b) the experiments and the calculation match in detail, i.e., even the slight changes of the absorption around $f_{\text{state}} = 235$ MHz and $f_{\text{state}} = 195$ MHz can be seen in both, the calculation and the measurement. This is a strong indication that the above model can also be used for the overall behavior of ensembles of vortices that exhibit small variations in the resonance frequency.

We have demonstrated that self-organization in magnonic vortex crystals is a reproducible process, valid for ensembles of vortices. The absorption of the ensemble approximates the absorption of the least-excitable polarization state at the corresponding state-formation frequency. This work allows further research studies to tailor the characteristic properties of magnonic vortex crystals by tuning the polarization state. It is predicted that the allowed energy bands in such a crystal can be adjusted via manipulation of the polarization pattern [Shi04]⁴. Also, the predominant direction of signal transfer through the vortex crystal can be tailored by tuning the dispersion relation⁵. In the following parts of this chapter further aspects of the self-organized state formation are examined. The main focus of the next section is the time-scale that is typically needed to adjust a polarization state.

⁴This could already be demonstrated for larger magnonic vortex arrangements in the publication Ref. [Beh15] – "Band structure engineering of two-dimensional magnonic vortex crystals" by Carolin Behncke, Max Hänze, Christian F. Adolff, Markus Weigand and Guido Meier

⁵This is exemplarily shown in the publication Ref. [Ado15] – "Gyrational modes of benzene-like magnetic vortex molecules" by Christian F. Adolff, Max Hänze, Matthias Pues, Markus Weigand, and Guido Meier (see chapter 5)

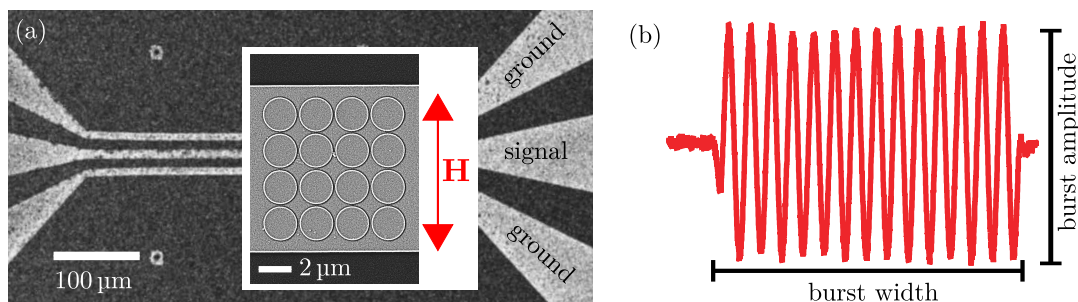


Figure 4.5.: Experimental setup. (a) Scanning transmission micrographs of the sample. A waveguide in ground-signal-ground geometry is fabricated above an ensemble of 4×4 vortex crystals (inset) in standard geometry. The coupling is adjusted to be relatively strong ($\frac{D}{2R} = 1.125$). (b) Profile of the current sent through the stripline used to tune polarization states via a burst-like magnetic field excitation.

4.1. Time-Scale of the State Formation⁶

As demonstrated in the last section, polarization states can be tuned using an adiabatically decreasing harmonic excitation. This mechanism could also be exploited for strongly coupled 4×4 crystals ($\frac{D}{2R} = 1.125$) shown in Fig. 4.5(a). Here, another signal form is used to tune polarization states via self-organized state formation. As depicted in Fig. 4.5(b), a continuous radio-frequent excitation with a defined duration is used to tune polarization states. The polarization states that emerge after the excitation with such magnetic-field bursts are identified by absorption spectra obtained from FMR measurements. In order to obtain sufficient magnetic contrast the waveguide covers 30 vortex arrays that are addressed as ensemble of vortex crystals in the following. This method gives insight into the time dependence of the state-formation process and yields a drastic increase in the number of state-formation cycles for a given time period. In a first step we observe the formation of polarization states for a proper choice of the frequency and the amplitude of the applied magnetic field burst (see Fig. 4.5(b)). In a second step the burst width is varied to identify the time-scale of the state-formation process. It is shown that states can be tuned within a small number of periods of the applied harmonic signal. The presented method is then used to achieve a memory-like writing process between polarization states on the sub-microsecond time-scale. A more comprehensive study, including numerical calculations can be found in the publication Ref. [Hän15].

⁶The results presented in this section are also published in Ref. [Hän15] – “Burst-mode manipulation of magnonic vortex crystals” by Max Hänze, Christian F. Adolff, Markus Weigand, and Guido Meier. Copyright 2015 by the American Physical Society.

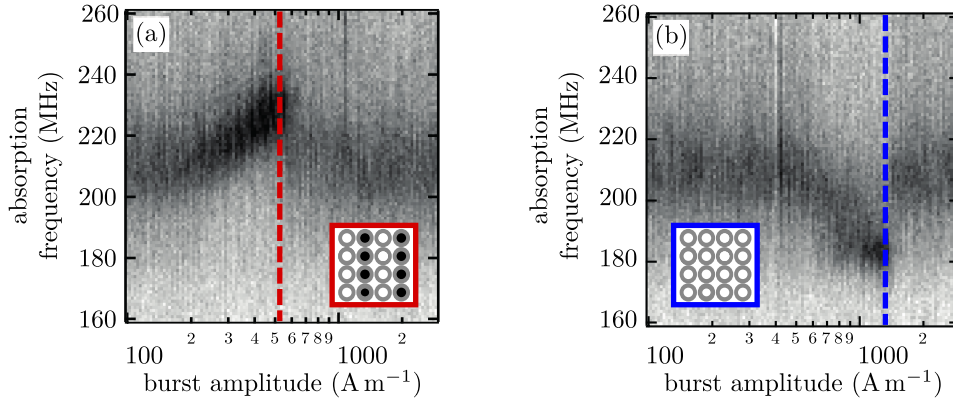


Figure 4.6.: Absorption spectra of the ensemble of arrays of 4×4 magnetic vortices after the application of a sinusoidal magnetic field burst with a width of $5 \mu\text{s}$. The frequency of the sinusoidal field burst is (a) 190 MHz and (b) 260 MHz. The burst amplitude is varied. The insets depict states that mainly contribute to the absorption around the critical amplitudes depicted as dashed vertical lines.

Figure 4.6 shows FMR absorption spectra after a sinusoidal magnetic field burst with frequencies of (a) 190 MHz and (b) 260 MHz and a width of $5 \mu\text{s}$. The burst amplitude is varied from 100 A m^{-1} to 2900 A m^{-1} . For low and high amplitudes the measured absorption spectra are identical. They correspond to the absorption of random polarization states within the ensemble of 4×4 vortex crystals. At intermediate burst amplitudes the absorption peak shifts away from the frequency of the field burst. This shift of the resonance frequency is attributed to the formation of polarization states, since efficiently excitable states, that yield strong absorption at the excitation frequency, are less stable. With increasing amplitude the number of stable states, i.e., states that are not switching during the excitation, decreases. The absorption spectra stem from the superposition of all stable states that are present in the ensemble [Hän15]. The maximum amplitude leading to state formation depends on the burst frequency and amounts to 550 A m^{-1} (Fig. 4.6(a)) or 1300 A m^{-1} (Fig. 4.6(b)). At those critical excitation amplitudes only one or at least only very few states are stable. Thus, the absorption spectra are only given by those states. For even higher amplitudes all crystals in the ensemble randomly switch between the polarization states. The most stable states according to X-ray measurements with adiabatically reduced field excitation (not shown) are a pattern of columns of constant polarization for the lower frequency $f_{\text{col}} = 190 \text{ MHz}$ and homogeneous polarizations at the higher frequency $f_{\text{hom}} = 260 \text{ MHz}$. Thus, the absorption spectra at the critical amplitudes depicted in Fig. 4.6 can mainly be attributed to those two patterns,

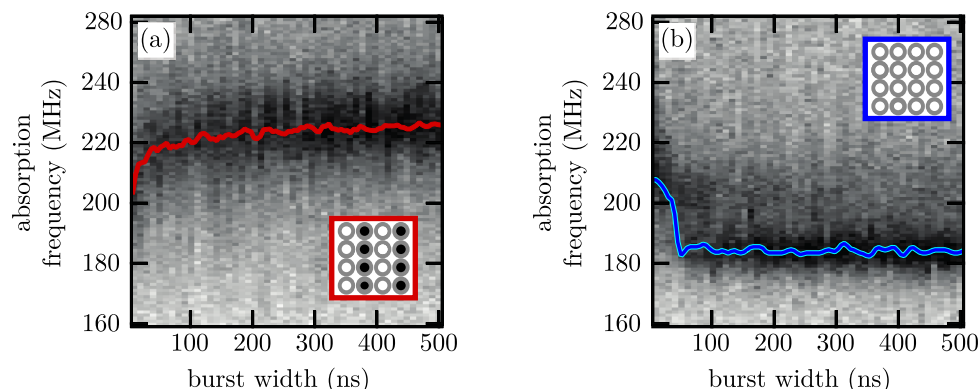


Figure 4.7.: Absorption spectra of the ensemble of arrays of 4×4 magnetic vortices for a constant burst amplitude of (a) 500 A m^{-1} and (b) 1200 A m^{-1} in dependence on the burst width. The frequency of the sinusoidal field burst is (a) 190 MHz and (b) 260 MHz . The insets depict states that mainly contribute to the absorption for burst widths above 100 ns . The red line indicates a smoothed fit to the maximum of the absorption to guide the eye. The time-scale of the polarization state-formation is about 100 ns .

respectively. To understand the time dependence of the state-formation, we performed additional measurements where the duration of the sinusoidal field burst is varied. Figure 4.7 depicts absorption spectra for the two different burst frequencies f_{col} and f_{hom} in dependence on the sinusoidal burst duration (width). The field amplitude has been adjusted so that only very few states are stable for both frequencies, respectively. We observe that for a burst width above 100 ns the absorption spectra remain on the same level, i.e., the polarization state is reliably tuned. The state-formation can be interpreted as a path through a potential landscape of polarization patterns. The oscillating magnetic field excites the vortices until they switch from an unstable into a random state. This process ceases when a certain stable state is reached. The time-scale to reach a stable state can be identified to be about 100 ns for the present material and geometry. This knowledge about the time-scale of the state-formation process allows to demonstrate a writing process on the sub-microsecond time-scale. Figure 4.8(a) depicts the absorption spectra of the ensemble of vortex crystals along the consecutive application of different magnetic field bursts. The peaks of the absorption spectra change depending on the characteristics of the two write bursts. We use the burst frequencies f_{col} and f_{hom} with burst amplitudes of $H_{\text{crit,col}} = 500 \text{ A m}^{-1}$ and $H_{\text{crit,hom}} = 1250 \text{ A m}^{-1}$, respectively. The write bursts have a length of 200 ns . In Fig. 4.8(b) the two different writing intervals are indicated by light blue and red regions. We observe that the polarization states are

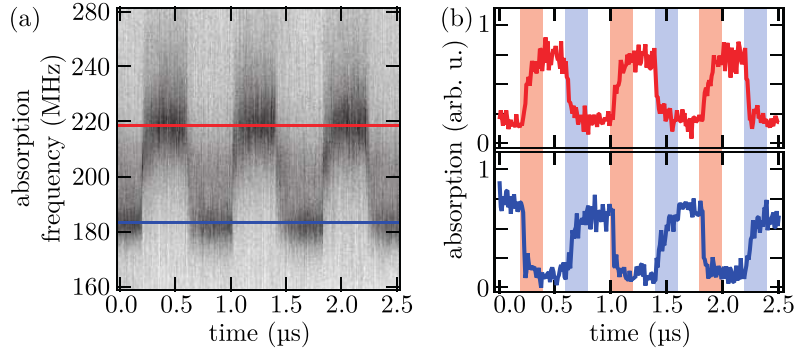


Figure 4.8.: (a) Absorption spectra of the writing process between two polarization states over time. (b) Absorptions at the highlighted frequencies of the absorption spectra (red and blue lines in (a)). The writing bursts are indicated by light blue and light red regions. They have frequencies of 180 MHz (260 MHz) and a length of 200 ns. The burst amplitude is 500 A m^{-1} (1250 A m^{-1}). The writing process is independent of the prior polarization state.

tuned independently of the previous polarization state. Thus, by using different write burst characteristics different absorption spectra can be generated. This allows to store and read the polarization states in a vortex crystal by the application of high-frequency currents through a single stripline.

4.2. Larger Crystals

In the last sections the formation of polarization states in crystals of up to $N = 16$ vortices has been presented. In the model described in the beginning of this chapter, the absorptions for the 2^N possible polarization patterns have to be calculated in order to predict the emerging state. This leads to tens of thousands of absorption curves already for 16 magnetic vortices. Due to such adverse time-complexity of the numerical model, it is not possible to calculate all absorption profiles for significantly larger crystals (with the current computing power). One way to handle that problem is to calculate only a representative subset of absorption profiles. Such Monte-Carlo-like calculations (not shown) are still being performed for the samples presented in this chapter. The focus of this section is to answer the question in how far the result of the self-organized state formation can be extrapolated from the predictions for smaller systems.

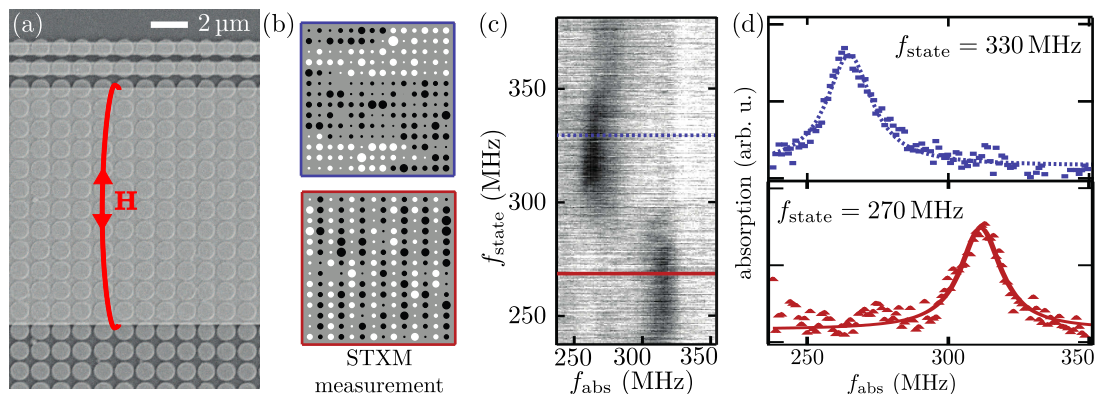


Figure 4.9.: Experiments on 50×50 rectangular crystals. (a) Scanning electron micrograph of a part of the sample. Three striplines are placed above the crystal. Two small striplines cover a row of disks each. A broad stripline covers 12 rows of disks. (b) Polarization states in a 12×12 area tuned with an adiabatic field reduction using the broad stripline (red: $f_{state} = 270$ MHz, blue: $f_{state} = 330$ MHz). The relative polarization is color-coded with black and white dots. The size of the dots depicts the gyration amplitude of the stationary motion determined via scanning transmission X-ray microscopy. (c) Absorption of the ensemble of five 50×50 crystals for different state-formation frequencies. (d) Absorption profiles for the two state-formation frequencies that led to the states depicted in (b).

4.2.1. Rectangular Crystals⁷

Figure 4.9(a) depicts a subarea of a 50×50 rectangular crystal with hundreds of vortices. In order to increase the number of vortices in the field of view of the X-ray microscope, the sample presented in Fig. 4.9(a) deviates from the standard geometry. The disks have a smaller radius of $R = 0.5 \mu\text{m}$, which is half of the standard radius. In order to keep the frequency band of efficient excitation in the experimentally favorable range of 200 MHz to 400 MHz (see chapter 3) the height of the disks has been reduced to $h = 40$ nm. Three striplines are fabricated on top of the crystal. The two small striplines can be used to transmit gyration waves of tunable wavelengths into the crystal. In the publication Ref. [Beh15] this has been used to determine the dispersion relation of the crystal. The broad stripline is used for the self-organized state formation with adiabatically reduced field excitations and will be of interest in the following. Fig. 4.9(b) shows the polarizations states that are tuned at the state-formation frequencies of 330 MHz (blue) and 270 MHz (red). In addition to the polarization information (white/black) the size

⁷Parts of this section have been published in Phys. Rev. B. (Ref. [Beh15] – “Band structure engineering of two-dimensional magnonic vortex crystals” by Carolin Behncke, Max Hänze, Christian F. Adolff, Markus Weigand and Guido Meier. Copyright 2015 by the American Physical Society)

of the dots depicts the gyration amplitude of the stationary motion. Especially in the bottom graph (red) one can see, that standing waves are present in the crystal when all vortices are excited with the alternating field sent through the broad stripline. Such wave modes [Han13] and the dispersion relation of the crystal are discussed in the publication Ref. [Beh15]. Here, we will focus on the state-formation process. Figure 4.9(c) shows the absorption spectra after self-organized state formations with different state-formation frequencies f_{state} in the range from 238 MHz to 380 MHz. One can see that mainly two absorption peaks are present at $f_{\text{abs}} = 265$ MHz and $f_{\text{abs}} = 312$ MHz. Two state-formation frequencies, highlighted with the horizontal solid red and dashed blue lines, are further investigated. Figure 4.9(d) shows the corresponding absorption profiles that resemble the profiles of the weakly coupled 3×3 crystal presented in Fig. 4.2(b). In the 3×3 crystals rows and columns of constant polarizations occur for both coupling regimes, respectively for high and low state-formation frequencies. Figure 4.9(b) shows the polarization states that emerged after self-organized state formation in the larger crystal. For the low state-formation frequency indeed columns of constant polarization occur, in analogy to the smaller crystal. In contrast, for the higher frequency, a state with large vertically alternating domains of constant polarizations emerges instead of the state with rows of constant polarizations. From the theory presented in the last sections one would expect that this emerging state has the lowest possible absorption at the state-formation frequency. Interestingly, numerical simulations show that several states have a lower absorption than the emerging state, especially the state with homogeneous polarizations and the state with rows of constant polarizations. The latter of the two states is less efficiently excitable. Consequently, one would expect rows of constant polarizations rather than the emerging state that can be considered a mixture of the expected state and the homogeneous state. A straight forward explanation of such behavior can be obtained when regarding the maximal amplitude of the state formation signal. When the amplitude is not sufficiently high, several states do not switch during the formation. Consequently, the system can settle in each of those states and not only in the state that is least efficiently excitable. Thus, in the experiments the amplitude of the state-formation signal might not have been high enough to isolate the state with rows of constant polarization. Besides such interpretation, the experimental results could also stem from the nature of the state-formation process itself, which can be understood as a path through a potential landscape. This vivid metaphor has already been introduced in the previous sections but it remains unclear whether the path is a random walk that eventually reaches a stable state, or a targeted path, that constantly reduces the energy

(absorption) of the system. The latter can be motivated by the assumption that unstable states with a lower absorption have a higher lifetime during the state-formation than unstable states with a higher absorption. In the experiment, rather row-like and rather homogeneous polarization states compete with regard to the stability. This might prohibit a targeted path through the potential landscape of the polarization states. During the process of state-formation, the polarization pattern constantly approaches to, and simultaneously diverges from, the most stable state of rows of constant polarization. Due to that, the convergence into the row-state might be unlikely or at least very slow.

In conclusion, we have seen that the major aspects of the findings for small rectangular crystals can be extrapolated to larger arrangements of disks. Column-like polarization states are stable at low frequencies and row-like states at high frequencies with respect to the eigenfrequency of an isolated disk. According to that, a perfect state with columns of constant polarization occurs in the experiment at the relatively low state-formation frequency of 270 MHz. The experiments reveal that a mixture of rows of constant polarization and homogeneous polarizations is tuned by the self-organized state formation at the relatively high frequency of 330 MHz. A state with rows of constant polarizations does not emerge although it has a lower absorption at this frequency, according to numerical calculations. This could be due to imperfections of the sample or an insufficient amplitude of the state-formation signal. However, it might also be understood within the presented model when regarding the state-formation as a targeted path through a potential landscape of possible polarization states.

Although a further investigation of the competing states certainly is an interesting topic⁸ we want to move on to a second example of larger magnonic vortex crystal. The next system shows strongly coupled pairs of disks with the standard disk geometry ($R = 2 \mu\text{m}$, $h = 60 \text{ nm}$) and a center-to-center distance of only $2.065 \mu\text{m}$ ($\frac{D}{2R} = 1.0325$). According to Eqn. 2.35, those pairs show a high bandwidth B_2 . Thus, they have clearly separated peak frequencies so that they promise to be best-suited for self-organized state formation. For all upcoming experiments – in the present and the next chapter – this geometry and center-to-center distance is used.

⁸Note that there are indications from additional measurements on this crystal (not shown) that the size of the domains depends on the state-formation frequency.

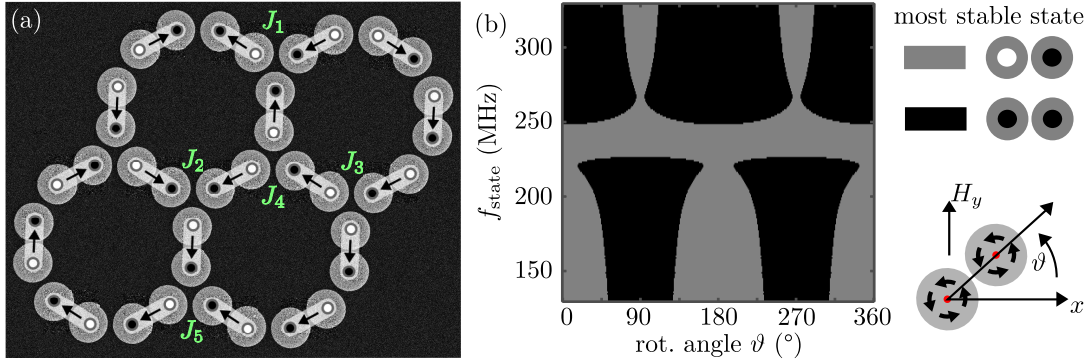


Figure 4.10.: (a) Experiments on a kagome lattice consisting of 19 pairs of disks in standard geometry. The disks within the pair show a stronger coupling $\frac{D}{2R} = 1.0325$ than neighboring vortices of different pairs $\frac{D}{2R} = 1.125$. The black and white dots in the insets of the scanning electron micrograph depict the polarizations measured via scanning X-ray microscopy after an adiabatic state formation with $f_{\text{state}} = 232.5$ MHz. For that a stripline (not shown) is placed over the whole lattice. All polarizations alternate within the pairs. The arrows in the insets illustrate the direction of the polarization alternation. (b) Numerical calculation for the most stable state for a pair of disks for different angles between the field excitation (y -direction) and the connecting line of the two disks. The schematic explains the rotation angle ϑ . Black contrast indicates that homogeneous polarizations are most stable. Analogously, gray contrast predicts that alternating polarizations will occur after a state formation at the corresponding state-formation frequency and rotation angle.

4.2.2. Kagome Lattice with Pairs of Vortices

Here we investigate an arrangement of strongly-coupled pairs of vortices. In those pairs only two non-degenerate polarization states can occur, i.e., alternating and homogeneous polarizations. Due to the strong coupling that is realized by a center-to-center distance of only $2.065 \mu\text{m}$ those two states are clearly addressable via self-organized state formation ($\frac{D}{2R} = 1.0325$). Fig. 4.10(a) shows an arrangements of such pairs of vortices that will be discussed in the following. The strongly coupled pairs are arranged in a kagome lattice. The minimal center-to-center distance of the vortices of different pairs is 250 nm ($\frac{D}{2R} = 1.125$) and thus the coupling can be regarded much weaker than within the pairs. The insets in Fig. 4.10(a) show the emerging polarizations after a state-formation with 232.5 MHz . The state-formation frequency is chosen so that all pairs exhibit alternating polarizations. This can be understood with the numerical calculations on a single pair of disks presented in Figure 4.10(b). They reveal that there is a frequency band where the state-formation leads to alternating polarizations regardless of the rotation angle θ of the pair with respect to the excitation field. This is possible due to the strong coupling.

The simplified dipole-model for a weakly coupled pair of disks described in Fig. 2.9 and Eqn. 2.32 cannot be used to explain such behavior⁹. Further numerical calculations show, that the frequency band where alternating polarizations are stable regardless of the rotation angle θ , widens for stronger coupling and vanishes when the criterion $\frac{D}{2R} = 2$ [Mej06] is exceeded. According to the predictions deduced from a single pair, the experiments presented in Fig. 4.10(a) prove, that indeed a state where all pairs of the large crystal show alternating polarizations can be reliably tuned. Consequently, the crystal can be understood as an arrangement of pairs of vortices with alternating polarizations. Such pairs can be represented by arrows pointing from the disk with one polarization (white dot) to the disk with the other polarization (black dot). The kagome lattice can be constructed by junctions of three such pairs that are rotated by 60° with respect to each other. The experiment shows that in all five junctions J_1 to J_5 two arrows point into the center and one points out of it, or vice versa. All three arrows never point into or out of the center of the junction. This behavior is known as the ice-rule in so-called artificial spin-ice that can be realized in analogous arrangements of nanomagnets instead of the vortex pairs [Lam10; Lad10; Li10; Men08]. In such artificial spin-ice systems the phenomenon of geometrical frustration can be observed. Further studies on such vortex crystals could investigate whether geometrical frustration also develops in such magnonic vortex-crystals. The fact that there is a state-formation frequency where pairs of disks always favor alternating polarizations motivates such a hypothesis. Nevertheless the process of state-formation is fundamentally different from the alignment of nanomagnets and further studies should be performed to proof the hypothesis. For the detailed investigation of geometrical frustration typically statistics about the violation of the ice-rules and the occurrences of different junction types are performed. Thus, the investigation of geometrical frustration in vortex systems requires a larger number of junctions. Unfortunately, it is not reasonably practicable to investigate larger kagome lattices than presented in Fig. 4.10 with scanning transmission X-Ray microscopy. Since the determination of the polarization of a single vortex lasts about one minute, detailed studies would exceed the availability of beamtime at a synchrotron. A promising measurement technique is the magnetic force microscopy. Although the capture time for one vortex core is in the same order of magnitude, a higher availability and the possibility of automated scanning of the crystal could allow to perform consecutive studies.

In conclusion, it has been motivated that the above vortex crystal shows similarities to

⁹The time-resolved scanning transition microscopy measurements show that the phases of the two vortices in the pair are not equal and vary depending on the rotation angle and the position of the pair in the crystal.

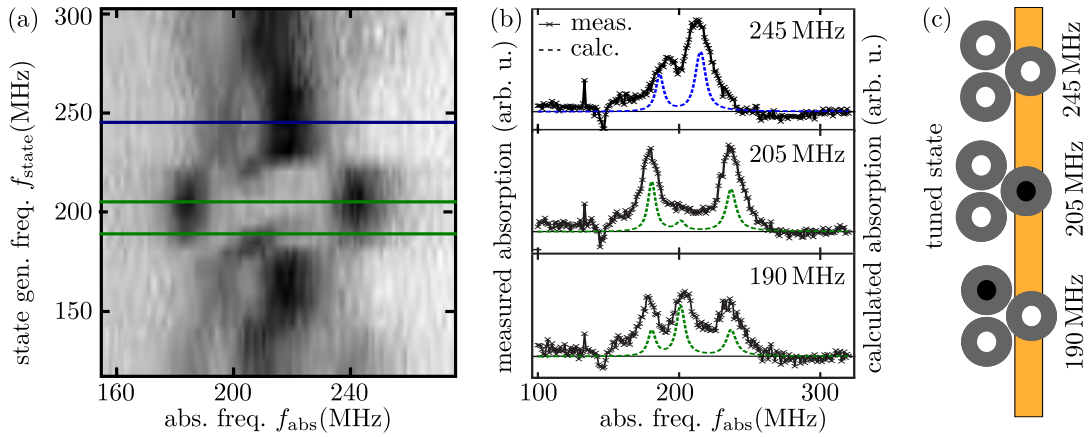


Figure 4.11.: (a) Absorption measurements for different state formation frequencies f_{state} on an ensemble of triples of disks in standard geometry with $\frac{D}{2R} \approx 1.025$. (b) Detailed absorption profiles at the three frequencies highlighted with horizontal blue or green lines in (a). Black line with marker: measurement. Dashed lines: numerical calculations. (c) Polarization configurations that yield the absorptions depicted in (b).

artificial spin-ice. The pairs of disks with alternating polarizations can be compared to nanomagnets, whereas the magnetization direction of the nanomagnet is analogous to the direction of the polarization alternation in the vortex pair. The frustration in such vortex-systems might particularly be interesting, since it presumably can be adjusted in-situ by the state-formation frequency. For example, the frustration might not occur for the same crystal when a state-formation frequency is chosen that tunes a homogeneous polarization pattern.

4.3. Indirect Self-Organized State Formation

One last aspect of the self-organized state formation will be discussed in the following. In the previous experiments all vortices have been equally excited by the alternating magnetic state-formation field. Nevertheless a formation of polarization states can also be realized when not all of the disks are directly excited. As an example for that, a triple of disks is investigated where the stripline is only placed over one of the three disks. Figure 4.11 shows the absorption of the triple for different state-formation frequencies. Since the center-to-center distance of the disks is only $D \approx 2.05 \mu\text{m}$ the strong coupling causes a complex state-formation behavior. Three different types of absorptions that alternate for varying state-formation frequencies can be identified in Fig. 4.11(a). Those

are exemplarily indicated by the horizontal blue and green lines at three different state-formation frequencies. For each type a high-resolution measurement has been performed that is depicted in Fig. 4.11(b) (solid black lines with markers). Calculations in the Thiele model reveal that those three absorption types correspond to the three non-degenerate polarization states that can be tuned in the triple. The experiment is simulated by applying an alternating unidirectional field to one disk. The resulting calculated absorptions are plotted as dashed lines in Fig. 4.11. One can see that the calculated absorptions feature the same characteristic peaks as the experiments. In addition a small middle-peak can be seen at $f_{\text{state}} = 205$ MHz that cannot be identified in the experiments. This is most probably due to ensemble broadening of the absorption spectra and a higher signal-to-noise ratio in the experiments. This comparison proves that the self-organized state formation also works when only parts of the disks of the crystal are excited by the state-formation field. For the triple of disks the indirect state formation allows to tune all three polarization states that are non-degenerate with respect to the frequency response.

Until now we have only focused on the state-formation result and did not discuss the stationary motions of the vortices during the absorption measurements. We will focus on this topic in the next chapter, where we will discuss the dispersion relation in benzene-like ring-molecules. As an introduction to the topic of the stationary motions we will discuss the eigenmotions of the triple in the remaining part of this section. This will allow to understand the form of the absorption spectra presented in Fig. 4.11(b).

As stated in section 2.2.1, the eigenmodes of an arbitrary arrangement of disk can be numerically calculated when damping is neglected [Hän14]. Figure 4.12 shows such modes for the triple of disks for the only two possible relative polarization states¹⁰. One pattern shows identical polarizations in all disks (homogeneous state) and the other pattern features two polarizations of the same sign and one polarization with a different sign (alternating state). Since there are three coupled vortex oscillators, the system shows three eigenmotions for each relative polarization state. The eigenmotions are depicted in Fig. 4.12 together with the corresponding eigenfrequencies. They feature a slightly elliptical form and different relative phases of the vortices. Note that the gyration direction depends on the polarization of the vortices. Thus, the dots in the sketches in Fig. 4.12 are only snapshots for the relative positions of the vortices for a certain point in

¹⁰Further results on the eigenmodes of a different sample, i.e., a rectangular arrangements of 3×3 vortices have been published in Ref. [Hän14] – "Tunable eigenmodes of coupled magnetic vortex oscillators" by Max Hänze, Christian F. Adolff, Markus Weigand, and Guido Meier. Copyright 2014 by the American Institute of Physics

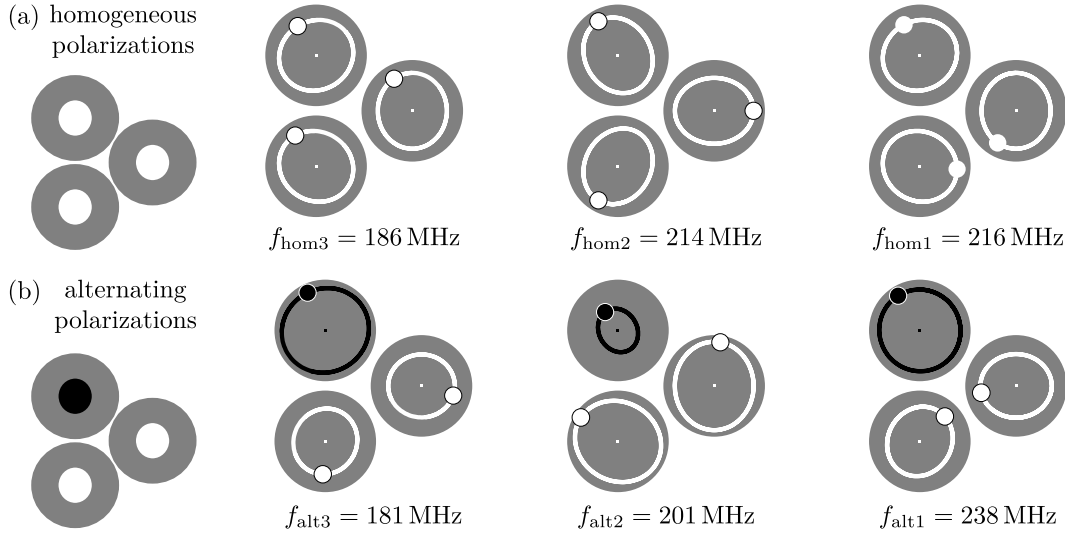


Figure 4.12.: Trajectories of the eigenmodes and corresponding eigenfrequencies calculated with the approach presented in Ref. [Hän14]. Phase relations of the depicted snapshot are indicated by black or white dots. The polarization is color-coded (white and black for positive and negative polarization) to indicate the sense of gyration.

time. Two of the three eigenfrequencies of the homogeneous state are only separated by 2 MHz ($f_{\text{hom1}} = 216 \text{ MHz}$, $f_{\text{hom2}} = 214 \text{ MHz}$). Consequently, they merge into one joint absorption peak in the calculations and measurements at $f_{\text{state}} = 245 \text{ MHz}$ presented in Fig 4.11. For the alternating polarization pattern all three eigenfrequencies are clearly separated. It can be seen in the measurements at $f_{\text{state}} = 190 \text{ MHz}$ that all three eigenmodes can separately be excited near the corresponding frequencies. In contrast, only two absorption peaks can be seen in the measurement at $f_{\text{state}} = 205 \text{ MHz}$ although the polarization pattern is identical, and thus features the same eigenmotions. This is due to the broken symmetry caused by the field excitation. At $f_{\text{state}} = 205 \text{ MHz}$, the vortex that has the minority polarization (black) is excited by the magnetic field, whereas at $f_{\text{state}} = 190 \text{ MHz}$ one of the two vortices with the majority polarization (white) is excited. When regarding the middle eigenmode of the alternating state in Fig. 4.12(b) one can see that the size of the trajectory of the vortex with the minority polarization is small with respect to the trajectories of the other two vortices. It is vividly plausible that such motion cannot efficiently be excited when the field is applied to the vortex with the relatively small motion. Thus, this eigenmode is suppressed in the absorption depicted in the middle graph of Fig. 4.11(b).

In conclusion, self-organized state formation can also be realized when not all vortices of the crystal are excited directly. Regarding the stationary motions, the emerging states show crucially different dynamics that can be understood via a superposition of eigenmodes. In the following we will make use of the remote self-organized state formation in order to further investigate the stationary motions of the vortices in ring-shaped arrangements.

5. Ring-Shaped Magnetic Vortex Molecules

In the last chapter the phenomenon of self-organized formation of polarization states in coupled magnetic vortex arrangements (crystals) was presented. In the publication Ref. [Hän14] this has been used to experimentally show that the dynamics in magnonic vortex crystals can be understood as a superposition of eigenmodes. The eigenmodes strongly depend on the relative polarizations whereas the superposition depends on the way the crystal is excited. The experiments substantiate the prediction that such vortex arrangements feature a reprogrammable band structure depending on their polarization configuration [Kru10b; Kra14; Han13]. In the publication Ref. [Beh15], it is experimentally proven that band structure engineering in two-dimensional magnonic vortex crystals is indeed possible. Here we will focus on the manipulation of the dispersion relation of ring-shaped arrangements of magnetic vortices. Especially the arrangement of six vortices brings the molecule benzene (C_6H_6) to mind that is a ring of six carbon atoms that each binds a hydrogen atom. When excited, for example with infrared light, small vibrations of the atoms with respect to the interatomic distances emerge. Historically, the comprehension of so-called normal-modes and the relation to their excitation frequencies was crucial for understanding the infrared and Raman spectra. Following the ideas of Wigner, Wilson showed in 1934 that the normal-modes could be deduced by using symmetry considerations regardless of the actual complex interactions of the atoms [Wil34]. Following this idea, one can derive that the normal-modes in vortex molecules largely depend on the symmetry of the system as well. This allows to deduce the form of the normal-modes only by symmetry considerations. The dispersion relation can then be deduced from the simplified Thiele model elaborated in chapter 2. Vortex-molecules with an arbitrary number of vortices can be fabricated. Experimentally rings with six and eight vortices are investigated. The theory allows for the transition to the model-system of an infinite chain with periodic boundary conditions, commonly discussed in textbooks

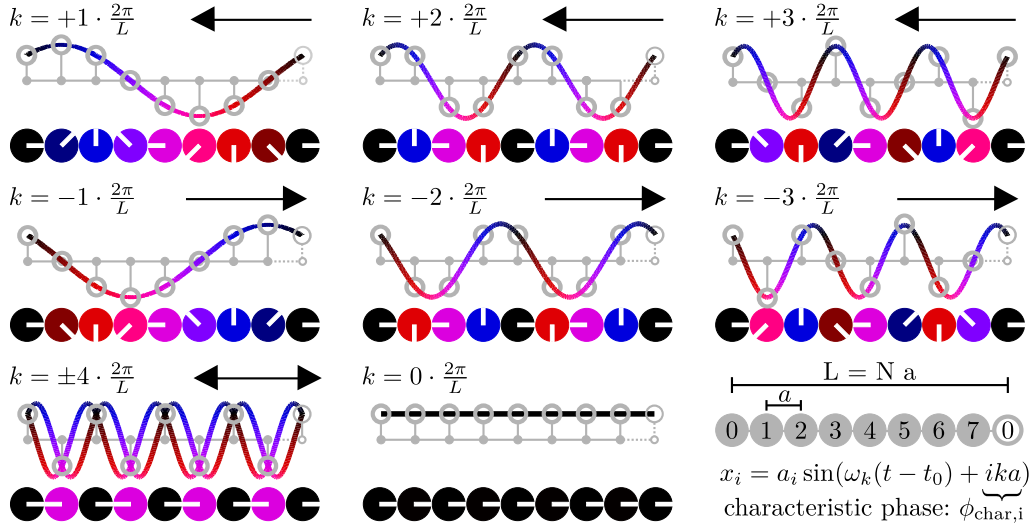


Figure 5.1.: Different representations for wave modes in chains with eight harmonic oscillators and periodic boundary conditions. The sinusoidal waves represent snapshots of the deflections x_i of the oscillators i . The waves propagate in negative x -direction for positive wave numbers k and in positive x -direction for negative values. The chain of colored dots describes the relative amplitudes and characteristic phases $\phi_{\text{char},i} = ika$. Both, the white lines and the colors, depict the characteristic phase. The radii of the circles correspond to the relative amplitudes a_i and are equal for all oscillators in this case.

about solid state physics like in Ref. [Kit76].

Figure 5.1 illustrates the eigenmodes for a chain of eight one-dimensional harmonic oscillators with periodic boundary conditions. Waves can only exist in the chain, when the wavelength λ is a fraction of the chain length L . Thus a mode is characterized in space by a phase difference between neighboring vortices of $\Delta\phi_{\text{char}} = ka$, where $k = \frac{2\pi}{\lambda}$ is the so-called wave number and a denotes the lattice constant, i.e., the distance between two oscillators. The number of different wave numbers k is identical to the number of harmonic oscillators N . When none of the modes is degenerate, all vortices gyrate with the same frequency and amplitude while showing the characteristic phases of $\phi_{\text{char},i} = ika$. The waves characterized by the wave number k propagate along the crystal during time whereas the sign of k determines the propagation direction. For negative wave numbers the wave propagates in positive x -direction and vice versa¹. For $k = 0$ all oscillations are in unison and the wave with $\lambda = \infty$ does not propagate. In Fig. 5.1 below the waves,

¹The propagation direction is inverted with respect to the common description of plane waves, i.e. $\sin(kx - \omega t)$. This is due to the different sign of the time dependency commonly used to describe gyrations of magnetic vortices. Consequently, $\sin(\omega t - kx)$ describes the standing wave in this work.

the characteristic phases $\phi_{\text{char},i} = ika$ are depicted as colored dots. Such characteristic-phase diagrams will be used to discuss the experiments in the following. Without loss of generality the initial time t_0 is chosen that $\phi_{\text{char},0} = 0$ for the vortex with index $i = 0$ in the diagrams.

Figure 5.2 shows an analog schematic for the gyration of vortices arranged in a ring. Although the gyrations are performed in two dimensions the approximately circular trajectories of the vortices can be described with the same two parameters as the linear chain, i.e., amplitude and phase of the oscillation (gyration). This yields

$$\vec{x}_{\kappa,i} = \tilde{r}_{\xi} a_{\kappa} \begin{pmatrix} \sin(\omega_{\kappa}(t - t_0) + i\kappa\alpha + ip_i\alpha + p_i c_i \pi) \\ \cos(\omega_{\kappa}(t - t_0) + i\kappa\alpha + ip_i\alpha + c_i \pi) \end{pmatrix} \quad (5.1)$$

in analogy to the linear chain and according to the stationary trajectory of an isolated vortex without damping excited by an alternating magnetic field (see Eqn. 2.22). The angle between the direction of the field and the x -axis is denoted as ξ . \tilde{r}_{ξ} is the corresponding rotation matrix. Again for the normal modes the oscillators gyrate with the same frequency and amplitude while showing a characteristic phase difference $\Delta\phi_{\text{char}} = \kappa a$. Here $\alpha = \frac{2\pi}{N}$ denotes the angle between two neighboring vortices in the ring and κ can be regarded as a dimensionless wave number. Since the vortices are arranged in a ring, an additional phase $ip_i\alpha$ is added that corresponds to a rotation of each vortex by $i\alpha$. The latter phase causes the symmetry of the eigenmodes to be analogous to the linear chain. For each point in time the vortex cores are located on geometric roulettes, i.e., epitrochoids and hypotrochoids. For wave numbers κ with $|\kappa| > 0$ the form of the roulettes stays constant over time and they rotate around the center of the ring, whilst the vortex cores are always located on the curve. Such trajectories are depicted for the case of identical polarizations and chiralities $c_i = p_i = 1$ in Fig. 5.2. For positive wave numbers $\kappa > 0$ the roulettes rotate clockwise and anti-clockwise for $\kappa < 0$. Thus, the sign of κ denotes the propagation direction of the gyration waves. For $\kappa = 0$ the normal mode is called the breathing mode since the vortices lie on a circle that changes its size over time. The type of the roulette depends on the polarization p_i . For positive polarizations $p_i = 1$ the vortices gyrate on epitrochoids for positive wave numbers κ and on hypotrochoids for negative wave numbers. In contrast, epitrochoids are present for negative wave numbers and hypotrochoids for positive wave numbers for the case of negative polarizations $p_i = -1$. Thus, the form of roulettes on the right and the left columns of Fig. 5.2 can be interchanged when switching the polarization of all vortices. The rotation direction does not change since it only depends on the wave number κ . Also the diagrams

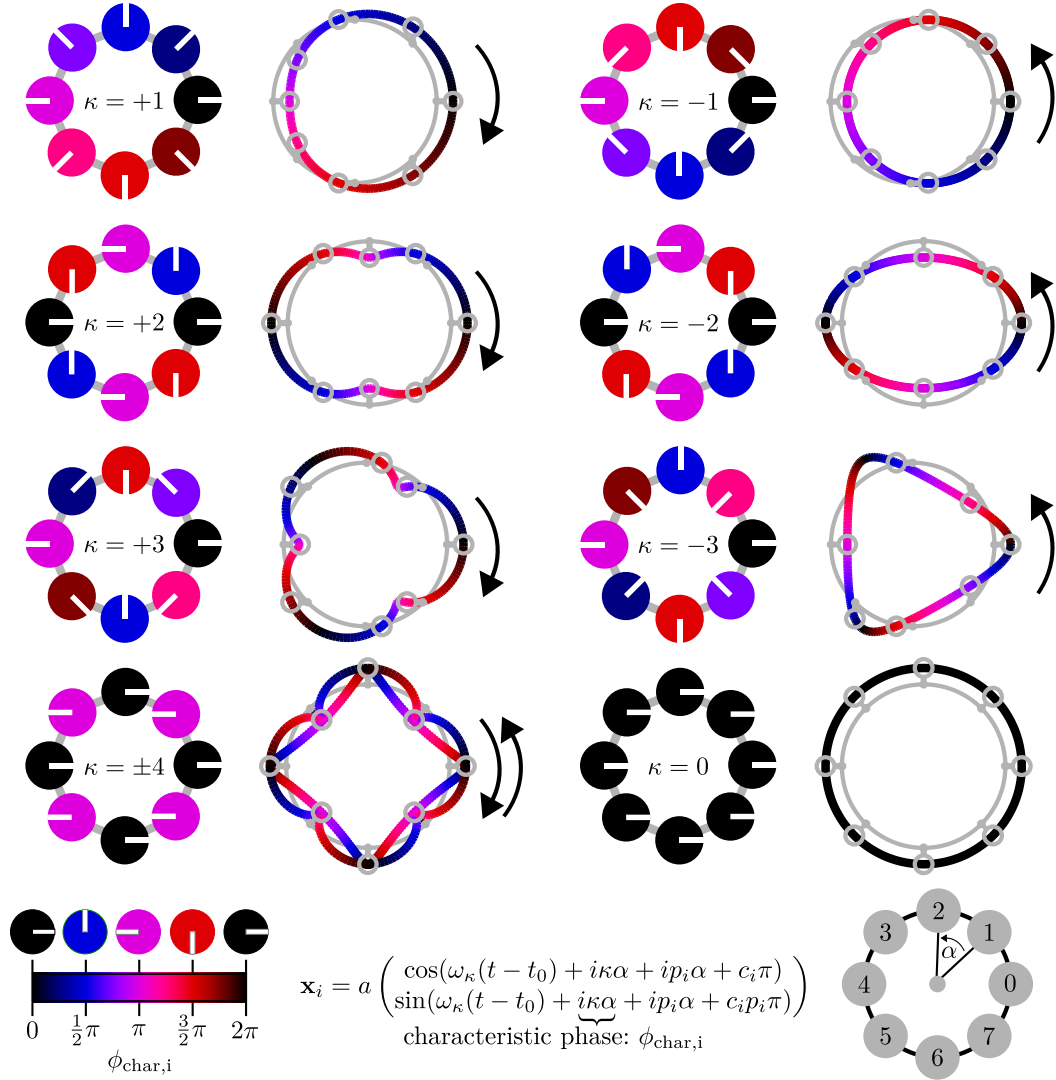


Figure 5.2.: Schematic of the proposed gyrational normal-modes in a ring of eight magnetic vortices. In analogy to Fig. 5.1 the characteristic phases $\phi_{\text{char},i} = i\kappa\alpha$ are depicted by colored dots. Both, the white lines and the colors, depict the characteristic phase. The radii of the circles correspond to the relative amplitudes a_i and are equal for all oscillators. The colored lines correspond to the gyrations of the vortices when equal polarizations and chiralities $p_i = c_i = 1$ are assumed for all vortices. The vortices are located on epitrochoids or hypotrochoids for positive or negative dimensionless wave numbers κ , respectively. The roulettes rotate clockwise for positive wave numbers and counter-clockwise for negative wave numbers. The depicted modes only occur in such way, when the damping is negligible and none of the modes is degenerated with respect to the corresponding gyration frequency ω_κ .

of the characteristic phases are invariant under the change of the polarization or chirality. The influence of the polarizations p_i and the chiralities c_i is described by additional phases $p_i c_i \pi$ and $c_i \pi$ in Eqn. 5.1. Note, that in general each vortex rotates on another roulette according to its polarization p_i and chirality c_i . For opposite chiralities c_i the vortices are positioned on identical roulettes that are rotated differently. Therefore, only the characteristic phases $\phi_{\text{char},i} = i\kappa\alpha$ and especially the corresponding dimensionless wave number κ , that are independent of the polarizations and chiralities, are used to describe the motions in the vortex-molecules in the following. In the following section, experiments are compared with the presented normal modes. The measured or simulated vortex-trajectories of the form

$$\vec{x}_{\text{meas},i} = \tilde{r}_\xi a_{\text{meas},i} C_i \begin{pmatrix} p_i \sin(\omega t + \varphi_{\text{meas},i}) \\ -\cos(\omega t + \varphi_{\text{meas},i}) \end{pmatrix} \quad (5.2)$$

can be compared with Eqn. 5.1 yielding the measured characteristic phases

$$\phi_{\text{char},i} = i\kappa\alpha = \varphi_{\text{meas},i} + \omega t_0 - ip_i\alpha. \quad (5.3)$$

Again the initial time t_0 is chosen that $\phi_{\text{char},0} = 0$ for the vortex with index $i = 0$. This allows to compare the measurements presented in the following section with the characteristic phase diagrams depicted in Fig. 5.2.

5.1. Molecule With Eight Vortices

The idealized characteristic phases of the gyration modes presented in Fig. 5.2 correspond to presumed normal modes of a vortex-molecule. In an experiment such modes never occur isolatedly but are always superimposed due to damping. To receive an impression whether the normal modes are in fact inherent in magnonic vortex crystals numerical calculations with reduced damping ($\omega = 226 \text{ MHz}$, $\Gamma = 2.5 \cdot 10^6 \text{ s}^{-1}$) are performed. The results are presented in Fig. 5.3 for two polarization patterns of identical (homogeneous) polarizations (a) and a polarization pattern that alternates along the ring (b). For the top graphs one of the vortices is initially deflected and the Fourier transform of the trajectories of all vortices during the relaxation is calculated. The damping is reduced by a factor of ten with respect to the experimental damping, so that the peaks in the Fourier transform are clearly separated. It can be seen that seven peaks occur for the homogeneous polarization configuration and only five peaks for the alternating polarization configuration.

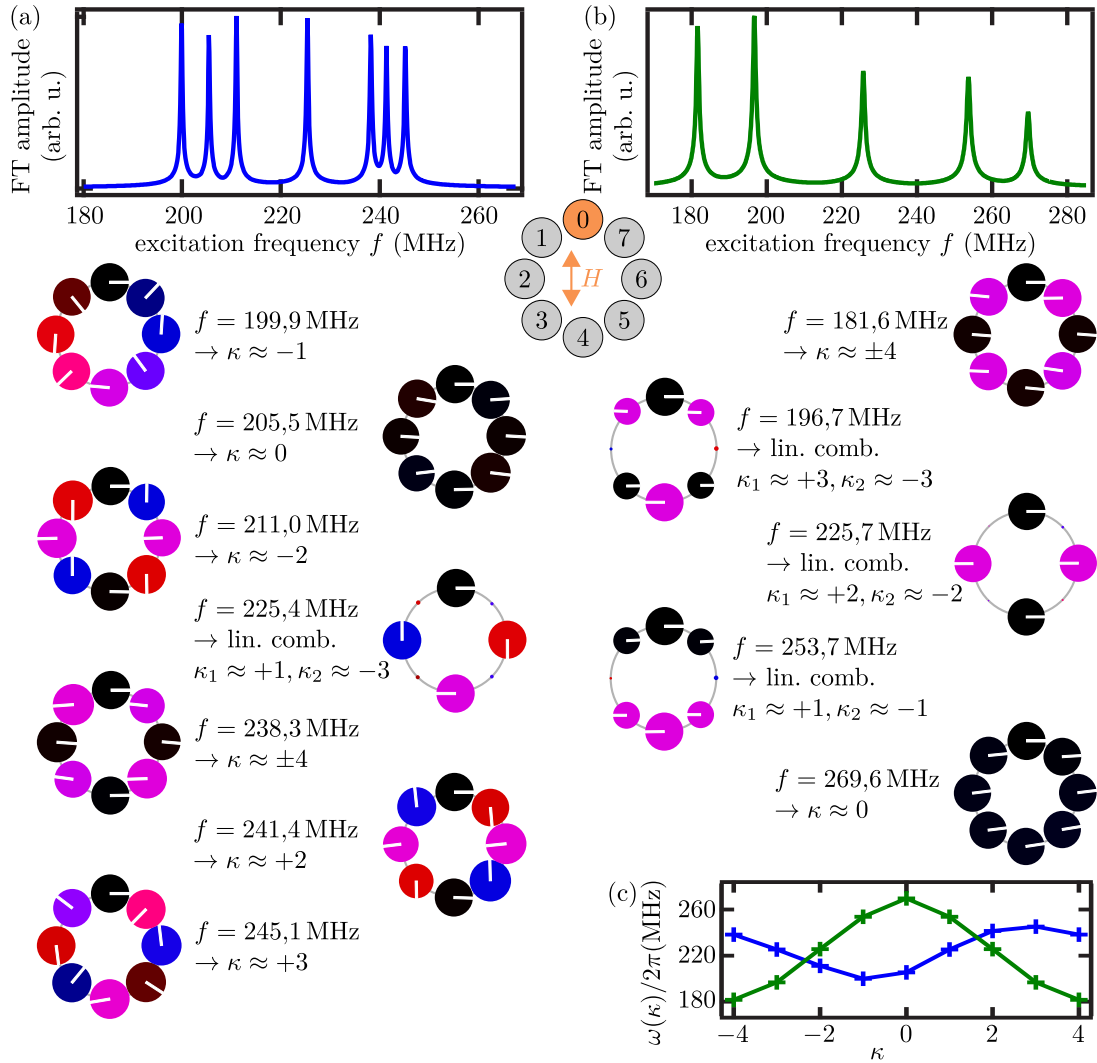


Figure 5.3.: Numerical calculations for a ring of eight vortices with reduced damping (a) Homogeneous polarizations $p_i = 1 \forall i$. (b) Alternating polarizations. The top graphs depict the possible resonances of the system. The colored dots represent the characteristic phases observed at the resonance frequencies. The inset between (a) and (b) illustrates the indexing of the vortices. Vortex 0 is excited with a magnetic field in vertical direction. (c) Dispersion relation for the homogeneous (blue) and alternating case (green) determined from the calculations presented in (a) and (b).

This is attributed to degenerate modes. This assumption can be confirmed when regarding the characteristic phase diagrams. For that, another numerical calculation has been performed in which the top vortex (index 0) is excited with a unidirectional alternating field in y -direction. The diagrams depict the characteristic phases when the molecule is excited near the peaks of the Fourier transform. The size of the circles correspond to the relative amplitude of the vortex gyrations a_i/a_0 . It can be seen, that especially for the homogeneous polarization pattern the phase relations strongly resemble the predicted normal modes. Except for the center mode of 225.4 MHz, the relative amplitudes of the vortex gyrations are almost equal and the relative phases can be associated with one wave number each. The central mode can be explained by a superposition of equal weight of the wave numbers $\kappa = 1$ and $\kappa = -3$. Thus all eight wave numbers can be associated with the seven resonances of the system. For the alternating polarization pattern even more wave numbers have identical frequencies. As depicted in Fig. 5.3(b) three of the five modes can be explained by a superposition of equal weight of two wave modes. Only the highest and the lowest resonance are simple modes that can be constructed by use of only one wave number. With this mapping of frequency and wave number the dispersion relation $\omega(\kappa)$ can be sketched (see Fig. 5.3(c)). The dispersion relation resembles sinusoidal curves as also predicted for linear chains of vortices [Han13] whereas the bandwidth is higher for alternating polarizations due to the stronger coupling [Vog11]. In the next section we will focus on the form of the dispersion relation in detail. Here we will firstly discuss the influence of the higher damping that is present in the experiments.

Figure 5.4 shows the experimental results of a ring with alternating polarizations obtained via STX microscopy in comparison with a simulation adapted to the experimentally determined properties of the disks ($\Gamma = 28.5 \cdot 10^6 \text{ s}^{-1}$, $\omega = 234.2 \text{ MHz}$, $s = 0.6875$). The alternating polarization pattern has been tuned by a self-organized state formation with a frequency of $f_{\text{state}} = 207.3 \text{ MHz}$. One can see from the calculated absorption spectrum depicted in Fig. 5.4(e) that the five resonances superimpose due to the higher damping. In the experiments the trajectories of the vortices are captured for three frequencies depicted as solid horizontal lines in Fig. 5.4(e). The polarizations and the chiralities are measured. The determined characteristic phases are presented along with the simulations in Fig. 5.4(b)-(d) for the three frequencies, respectively. The simulations and the experiments are in good accordance. The highest frequency of 280 MHz is close to the highest resonance of the molecule. According to the simulations with lower damping

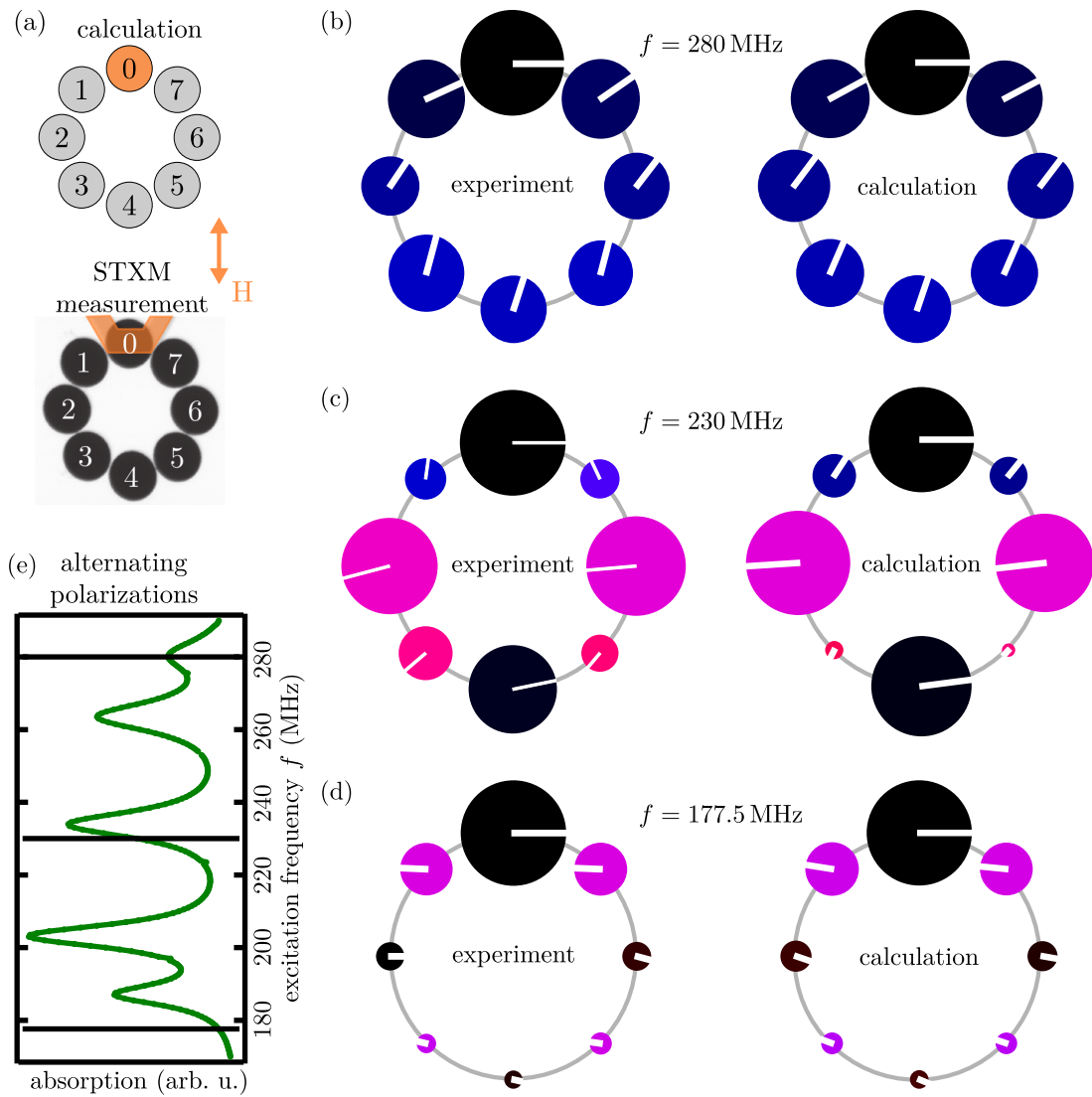


Figure 5.4.: Measurements along with numerical calculations performed on a ring with eight vortices with alternating polarizations. (a) Schematic. (b)-(d) Results for the characteristic phases for three different excitation frequencies. Left diagrams: experimental results obtained via STX microscopy. Right diagrams: Numerical calculations. (e) Calculated absorption. The horizontal black lines depict the three measurement frequencies.

presented in Fig. 5.3, the breathing mode $\kappa = 0$ should occur at this frequency². Including damping, the characteristic phases are not identical but bend up the farther the vortex is away from the excited vortex $i = 0$. Nevertheless, all vortices have comparable amplitudes which are predicted for an excitation of a single normal mode. At the medial frequency of 229.7 MHz, depicted in Fig. 5.4(b), the trajectories alternate in amplitude. The vortices with even indices have higher amplitudes than the vortices with odd indices. This is characteristic for a superposition of modes $\kappa_1 = 2$ and $\kappa_2 = -2$ that corresponds to standing waves. For zero damping, the motions of the vortices with odd index can be neglected whereas in the experiment the amplitudes are only reduced by about 50% since further modes are superimposed. In Fig. 5.4(c) a phase difference of approximately $\Delta\phi_{\text{char}}(\kappa = 4) = \pi$ is present for all vortices, when the ring is excited with the lowest experimental frequency of 177.4 MHz. This has also been predicted for the lowest resonance frequency in the low-damping case presented in Fig. 5.3(b). In contrast to such calculations, the vortices that are far away from the excited vortex 0 have smaller amplitudes, since the molecule is excited below the corresponding resonance (see Fig. 5.4(e)). In conclusion it can be stated that the X-ray measurements performed on a ring-molecule of eight Permalloy disks can be understood analogous to the model of normal modes in a chain of harmonic oscillators with periodic boundary conditions. Up to now the effects of the relatively strong damping of the vortex core oscillation has only been described phenomenologically on the basis of a comparison between the experiments and numerical calculations. The calculation and the simulations are in good agreement but the mode mixing has not been investigated systematically. In the following section further measurements on a benzene-like vortex molecule consisting of six vortices will give insight into the mode mixing and the dispersion relation of such ring-molecules.

5.2. Benzene-Like Vortex Molecule³

Figure 5.5 shows the investigated vortex molecule consisting of six Permalloy disks. At first the homogeneous polarization pattern shown in Fig. 5.5(a) will be discussed. It is adjusted by applying an offset field during the nucleation of the vortices that is perpendicular to the plane of the disks. As described in the previous section, due to the N -fold

²Note, that in Fig. 5.3 the model parameter are not adapted to the experiment. Thus the absolute values for the resonance frequencies differ.

³The publication Ref. [Ado15] – "Gyrational modes of benzene-like magnetic vortex molecules" by Christian F. Adolff, Max Hänze, Matthias Pues, Markus Weigand, and Guido Meier is based on the findings presented in this section. Copyright 2015 by the American Physical Society.

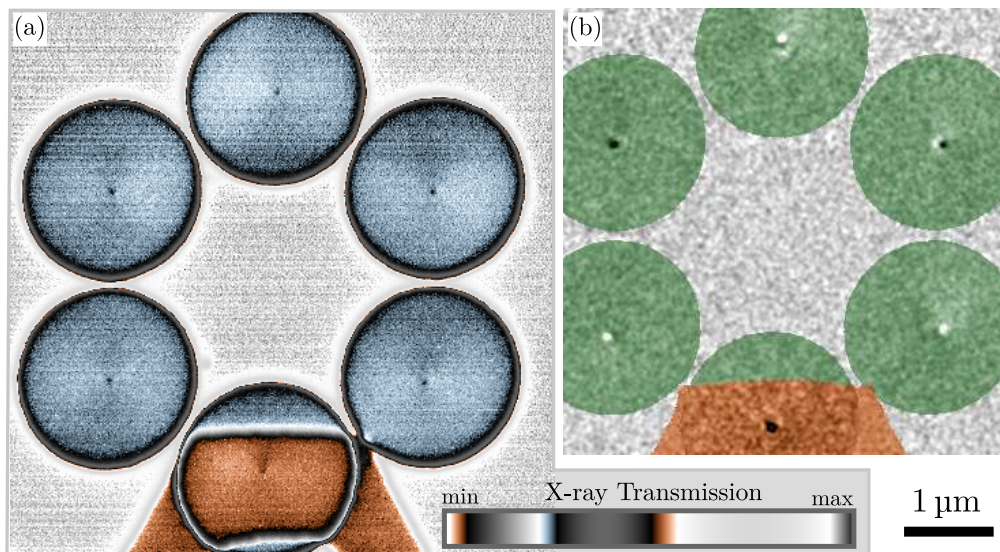


Figure 5.5.: X-ray micrographs of six disks that contain a vortex each. The Permalloy disks are 60 nm thick and have a 2 μm diameter, the minimal distance between the disks is 60 nm. (a) Vortex molecule with homogeneous core polarizations in all six disks. The magnetic contrast can be seen in the raw data of one time frame. The vortex cores appear as black dots. (b) Vortex molecule with alternating polarizations. The static contrast is subtracted to emphasize the magnetic contrast even more prominently (see section 3.2). Disks and stripline are colorized. In the captured movie black vortex cores gyrate clockwise ($p_i = -1$) and white cores counter-clockwise ($p_i = 1$).

rotational symmetry and the linearity of the system, there has to be a basis of N normal modes, that fulfill this symmetry. In analogy to the description of a linear chain of harmonic oscillators with periodic boundary conditions, we determine these modes to be plane waves with wavelengths that are fractions of the circumference of the ring. For a ring of an even number of N disks the normal modes are given by Eqn. 5.1. In the last section the characteristic phases $\phi_{\text{char},i} = i\kappa\alpha$ have been determined from the experiments. We have seen that the motions can indeed be understood by a superposition of such modes. Hence, here we directly fit a linear combination of such normal modes

$$\vec{x}_i(\omega_{\text{exc}}) = \sum_{\kappa=-3}^2 \vec{x}_{\kappa,i} \quad (5.4)$$

to the experiments. The weights of the linear combination are given by the amplitudes $a_{\kappa}(\omega_{\text{exc}})$ of the normal modes (see Eqn. 5.1). Those are called normal modes contributions in the following. Figure 5.6(a) depicts the form of the normal modes for equal chiralities and polarizations ($c_i = 1$, $p_i = -1$) of all vortices. Since a homogeneous polarization

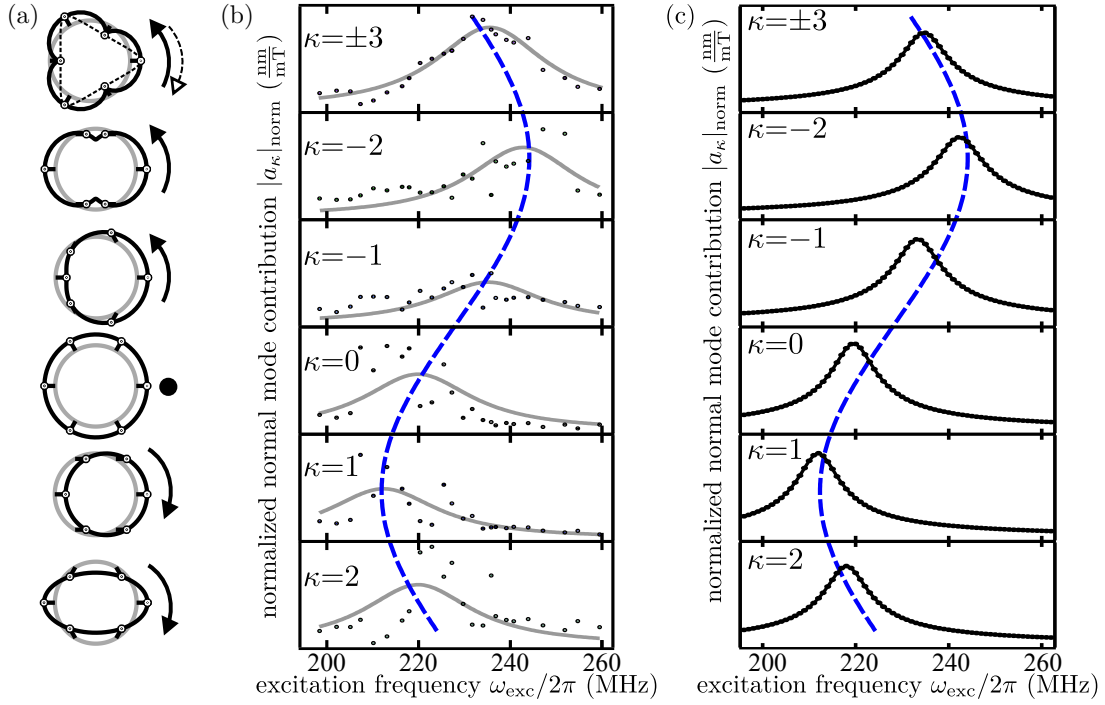


Figure 5.6.: (a) Pictograms for the form and the propagation direction of the normal modes of the ring ($p_i = -1$). (b) Experiments with a homogeneous core polarization pattern ($p_i = -1$). Each graph shows the contribution of a normal mode to the overall motions in the molecule for different excitation frequencies. The data points are obtained by a fit to the trajectories traced via scanning transmission X-ray microscopy. The solid gray lines are Lorentzian fit curves (Eqn. 5.7). The linear [Sil99] influence of different excitation strengths is normalized out. The vertical scale of each graph ranges from 0 to 34 nm/mT. (c) Numerical calculations equivalent to the experiments presented in (b). The vertical scale reaches from 0 to 310 nm/mT. The higher excitation efficiency can be explained by absence of surface roughnesses and impurities.

pattern with $p_i = -1$ is present in the molecule, some properties invert with respect to normal modes presented in Fig. 5.2 in the last section (page 64). Epitrochoids are present for negative wave numbers and hypotrochoids for positive wave numbers. Figure 5.6(b) shows the experimental results for the investigated vortex-benzene, when the homogeneous polarization pattern $p_i = -1$ is present. The steady-state motions of the vortices are traced for 24 different frequencies around the resonance frequency of an isolated disk. The gray line in each of the six graphs is a Lorentzian fit through the black data points that are proportional to the absolute gyration amplitude $|a_\kappa|$ of one normal mode $\vec{x}_{i,\kappa}$. These data points are obtained by applying a curve fit with the linear combination of normal modes given by Eqns. 5.1 and 5.4 to the vortex trajectories of the six vortices. For each frequency one global curve fit is performed that comprises the complete motion of the six vortices and thus yields one data point in each of the six graphs. It is an experimental necessity to vary the strength of the alternating magnetic field for different frequencies of excitation in order to ensure threshold gyration amplitudes for all vortices. The approximately linear influence [Lan12; Sil99] of the different excitation strengths is normalized out in Fig. 5.6(b). The experimental data points show a relatively strong variation. Therefore, a numerical calculation presented in Fig. 5.6(c) has been performed, and evaluated in the same way as the experiment, in order to more clearly see the superposition of the normal modes. We point out that each eigenmode has its maximal contribution at different frequencies that lie on a sinusoidal line (dashed blue). This can be understood with the circular-trajectory dipole-approximation presented in section 2.2.2. When inserting an eigenmode $\vec{x}_{\kappa,i}$ into Eqn.2.30 and only regarding next-neighbor interaction, the frequency offset $\omega_{\text{hom}}(\kappa) = \omega_{\text{iso}} - \omega_\kappa$ of the maximal mode contribution with respect to the resonance frequency of an isolated disk ω_{iso} follows to be⁴

$$\omega_{\text{hom}}(\kappa) = \omega_{\text{iso}} - \frac{1}{2}B_{\text{hom}} \cos((\kappa + p)\alpha). \quad (5.5)$$

The bandwidth B_{hom} is a positive constant given by $B_{\text{hom}} = \frac{1}{C'} \frac{\mu_0}{2\pi D^3} (\frac{\tilde{a}_\kappa}{a_\kappa})^2$. The strength of the dipole moment is denoted as \tilde{a}_κ since it is proportional to the gyration amplitude a_κ . The relation $\omega_{\text{hom}}(\kappa)$ will be called the analytically determined dispersion relation in the following. Since $\omega_{\text{hom}}(+1) = \omega_{\text{hom}}(-3)$ for the case of $p_i = 1 \forall i$ and $N = 8$, this explains the degeneracy of the corresponding modes in Fig. 5.3. Note that the dispersion relation is not reflection symmetric. Thus, contrary to the actual benzene molecule, the propagation of identical waves (same κ) in the two possible directions (sign of κ)

⁴The simplification is straight forward. Interactions with further neighbors can also be included easily. For the mathematical proof see appendix A.3

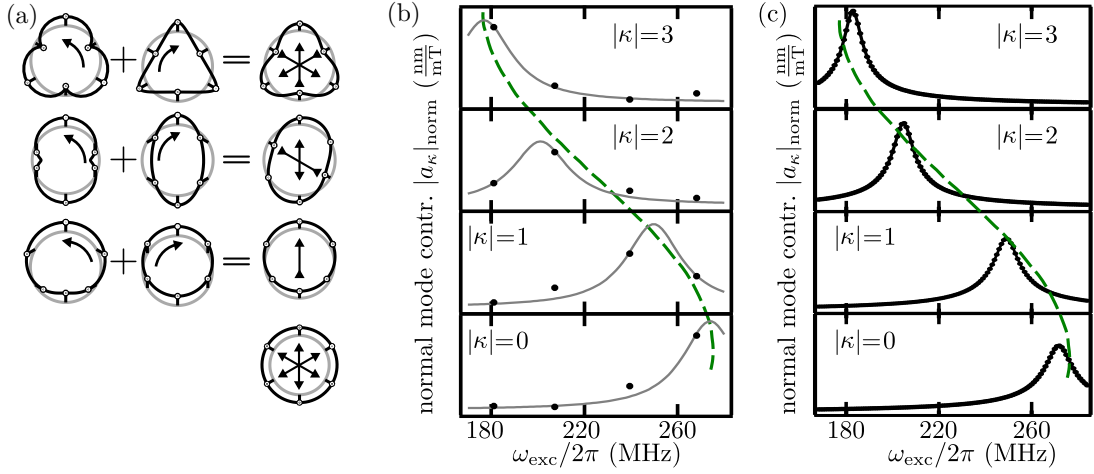


Figure 5.7.: (a) Pictograms of the composition of the normal modes to obtain standing waves. (b) Experiments with alternating polarization pattern. Each graph shows the contribution of a standing wave to the overall motions in the molecule for different excitation frequencies. The data points are obtained by a fit to the trajectories traced via scanning transmission X-ray microscopy. The solid lines correspond to the fit with Eqn. 5.7. The vertical scale is identical to that in Fig. 5.6(b). (c) Numerical calculations equivalent to the experiments presented in (b). The vertical scale is identical to that in Fig. 5.6(c).

is not degenerated. The global gyration direction of the vortices in the homogeneous polarization case has no equivalent in the linear vibrations in benzene. Such kind of global gyration direction cannot be defined for an alternating polarization pattern since the vortices gyrate in different directions according to their polarization p_i . The alternating polarization pattern is shown in Fig. 5.5(b) and has been adjusted experimentally using an adiabatic state formation at $f_{\text{state}} = 224$ MHz. Although only one vortex is directly excited, indirect self-organized state formation allows to tune the polarizations in the whole molecule (see section 4.3). The symmetry of the ring changes due to the alternating polarization pattern so that two normal modes $\vec{x}_{i,|\kappa|} = \vec{x}_{i,\kappa} + \vec{x}_{i,-\kappa}$ have to be combined in order to get standing waves. For such superposition of modes Eqn. 2.30 yields

$$\omega_{\text{alt}}(\kappa) = \omega_{\text{iso}} + \frac{1}{2}B_{\text{alt}} \cos(\kappa\alpha), \quad B_{\text{alt}} = 3 B_{\text{hom}}. \quad (5.6)$$

for next-neighbor interaction⁵. One can see that with respect to the homogeneous case (Eqn. 5.5) the factor p vanishes in the cosine and the prefactor is multiplied by (-3) . The different bandwidths are commonly explained by a weaker coupling between vortices of

⁵The simplification is straight forward. Interactions with further neighbors can also be included easily. For the mathematical proof see appendix A.3

equal polarization than of vortices with different polarizations [Vog11]. Recently, studies by Oksana et al. confirm such factor for triples and clusters of vortices [Suk15]. For the borderline case of an infinite linear chain ($N \rightarrow \infty$) the results of Eqns. 5.5 and 5.5 are in concordance with previous results [Han13]. Considering the alternating case, Eqn. 5.6 is reflection symmetric and thus no preferred propagation direction is present. This time, all modes can be compared to the normal modes of the actual benzene molecule when only the carbon atoms are regarded. Using the Wilson numbering [Wil34], the normal mode with $|\kappa| = 1$ corresponds to mode 'Y' of the actual benzene, $|\kappa| = 2$ corresponds to mode '6a' and $|\kappa| = 3$ can be compared to normal mode '12'. The pictograms for such modes used by Wilson in the seminal publication Ref.[Wil34] are depicted as arrows in the center of the normal modes presented in Fig. 5.7(a). The standing waves are fitted to the trajectories and yield the results presented in Fig. 5.7(b)⁶. In the following we discuss the effects of damping on the experimental results. For negligible damping, there are sharp resonances when the eigenfrequency of a normal mode is met. This case has been depicted Fig. 5.3. In the experiment the damping allows to excite the system in between those resonances. The normal modes mix in the way shown in Fig. 5.6 and 5.7 for the two investigated polarization patterns. The contributions $a_\kappa(\omega_{\text{exc}})$ are fitted to the experimental data with Lorentzian functions that are shifted according to the analytically derived discrete dispersion relation $\omega(\kappa)$

$$a_\kappa(\omega_{\text{exc}}) = \mathcal{L}_\Gamma(\omega_{\text{exc}} - \omega(\kappa)), \kappa \in \left[-N/2, \dots, N/2\right] \quad (5.7)$$

This set of equations can be understood as the continuous dispersion relation of the damped system, where ω_{exc} is the frequency of the exciting magnetic field and $\mathcal{L}_\Gamma(\omega)$ the Lorentzian peak function with damping parameter Γ . According to Eqns. 5.1, 5.4 and 5.7, the motion of the vortices is then given by

$$\vec{x}_i(\omega_{\text{exc}}) = \sum_{\kappa} \mathcal{L}_\Gamma(\omega_{\text{exc}} - \omega(\kappa)) c_i \tilde{r}_\xi \begin{pmatrix} p_i \sin(\omega_{\text{exc}}(t - t_0) + i\kappa\alpha + ip_i\alpha) \\ \cos(\omega_{\text{exc}}(t - t_0) + i\kappa\alpha + ip_i\alpha) \end{pmatrix} \quad (5.8)$$

whereas for $\omega(\kappa)$ the analytical dispersion relation of the actual polarization pattern (ω_{hom} or ω_{alt} , Eqns. 5.5 or 5.6) has to be inserted. The global fit of the experimental data presented in Fig. 5.6(b) and Fig. 5.7(b) with the set of normal mode contributions $a_\kappa(\omega_{\text{exc}})$ (Eqn. 5.7) corresponds to the gray Lorentzian curves and yields

⁶Due to the limited beam time, the chiralities of the vortices have not been measured for the alternating case. They are determined to fit best with $C_i = (-1, 1, 1, -1, 1, 1)^T$.

the three model parameters ω_{iso} , B_{hom} , and Γ . The parameters are determined to be $\frac{\omega_{\text{iso}}}{2\pi} = (225.5 \pm 1.5)$ MHz and $B_{\text{alt}} = (96 \pm 6)$ MHz for the alternating case and $\frac{\omega_{\text{iso}}}{2\pi} = (227.6 \pm 0.8)$ MHz and $B_{\text{hom}} = (31 \pm 2)$ MHz for homogeneous polarization pattern. In both cases the damping parameter has a reasonable value of $\Gamma = (29 \pm 3) \cdot 10^6$ MHz ($\Gamma = 2\alpha_{\text{Gilbert}}\omega_{\text{iso}} \approx 0.02\omega_{\text{iso}}$ [Mar13]). In order to reach the same accuracy in the numerical calculations the coupling strength had to be adjusted to $s = 0.483$ in the homogeneous case. This value deviates from the standard parameter of $s = 0.6875$ used for the alternating case and all other experiments shown in the previous chapters. Without the reduction of s , the bandwidth of the homogeneous case would be overestimated [Wan14; Suk15]. For a discussion on the coupling strength parameter s see appendix A.2.

In conclusion we have shown that there are strong similarities between the vibrational modes of benzene and the gyrational modes of a six-fold magnetic-vortex ring-molecule. The symmetry of both systems determines the motions of the oscillators, i.e., the carbon atoms or the vortices. The best accordance in the analogy can be achieved when an alternating polarization pattern is tuned to the vortex molecule. In this case all gyrational modes can be identified with vibrational modes in the actual benzene. The symmetry allows to simplify the derivation of the fundamentally different dispersion relations of the vortex molecule for the homogeneous and alternating core polarization patterns. In contrast to other models the presented approach includes the effect of damping and is characterized by only three model parameters, each of them determined in the experiments. Both dispersion relations have been confirmed by X-ray transmission microscopy proving that the magnetic vortex molecule features a reprogrammable band structure or dispersion relation.

6. Conclusion and Outlook

Ferromagnetic microdisks for the investigation of magnetic vortex dynamics were fabricated at the Institute of Applied Physics of the University of Hamburg. The magnetic vortex is the magnetic ground state of such microstructures. It can be described by two binary state parameters, i.e., polarization and chirality. The dynamics of vortices are characterized by a gyration of the vortex core around the center of the disk. Theoretically their dynamics are described in a quasi-particle model. In consequence, the findings of this work are also applicable for other magnetic particles like magnetic bubbles or skyrmions [Rom15; Woo15] that can be excited to perform gyrational motions [Dai13; Mak12; Ono12].

The influence of the stray field coupling on the vortex dynamics has been studied via scanning transmission X-ray microscopy and ferromagnetic absorption spectroscopy. The experiments reveal many analogies to the dynamics of coupled harmonic oscillators, which especially applies to the last chapter where normal modes have been identified in ring-shaped arrangements of vortices. The experiments illustrated that the dynamic properties, i.e., the dispersion relation of such molecules strongly depends on the polarization configuration. For a configuration where the polarizations alternate along the ring, the dispersion relation shows a higher bandwidth and is shifted in the space of wave numbers with respect to the case of identical polarizations. Such behavior of the dispersion relation could also be analytically determined by using the approximation of circular trajectories and exploiting the symmetry of the system. Thus, the findings of chapter 5 substantiate that the manipulation of the polarization in such vortex arrangements is of paramount interest, especially with regard to the in-situ manipulation of magnonic crystals consisting of magnetic vortices. One way for such a manipulation has been presented in chapter 4 on the "self-organized state formation in magnonic vortex crystals" – the main topic of this work. An adiabatic reduction of a strong unidirectional field exciting the gyrotropic modes of the vortices, allows for a formation of global polarization states that is mediated by the local, next-neighbor interaction of the vortices. The results of

such polarization-switching process could be effectively predicted for various types and sizes of vortex arrangements by use of a fundamental stability criterion considering the absorption of the polarization patterns. During the adiabatic field-reduction the vortex arrangements settle in the least efficiently excitable state, which is the state that shows the lowest absorption at the frequency of the state-formation. With that it was possible to tune the alternating polarization pattern in the ring-molecules presented in chapter 5 by exciting only one of the vortices. Besides such "indirect self-organized state formation" (section 4.3) further aspects of the phenomenon have been investigated, e.g., the time-scale of the state formation (section 4.1) that is determined to be in the range of 100 ns for a rectangular 4×4 crystal. Experiments on larger magnonic crystals (section 4.2.1), with more than 100 vortices substantially show behavior that is expected from the theory elaborated for smaller arrangements but also reveals the current limits of the comprehension of the self-organized state formation. Further studies could gain a deeper understanding of the state-formation process itself, instead of predicting the outcome. A simple way to understand the state-formation is the idea of a path through a "potential landscape" of polarization patterns. Up to now it remains unclear whether this path is a random walk that eventually results in the least excitable state or a target-oriented path that constantly reduces the absorption of the system. Studies on this question could reveal whether the process of self-organized state formation does always converge in finite time, regardless of the size or the form of the crystal. Indications for two patterns that compete and thus prohibit a convergence have been found in the experiments on large rectangular crystals. A related unanswered question is whether the state formation shows the phenomenon of geometrical frustration. Up to now it has been shown that there are strong similarities between geometrically frustrated arrangements of nanomagnets and analogous arrangements of vortices like they are presented in section 4.2.2. Such experiments on hexagonal arrangements of vortices could be further elaborated. Frustrated systems are of great general interest since they give insight into the nature of statistically disordered systems [Lam10]. On the other hand, studies on frustration allow for future spintronic devices, either for memory applications or to perform logic operations [Men08]. Although commonly used for data-storage applications, there are relatively few attempts to exploit magnetic-vortex phenomena for logic functionality [Imr06]. This could be an interesting field for arrangements of coupled vortices since it has been shown recently that coupled magnetic vortices can be used to implement transistor functionality [Kum14]. The aspect of data storage with magnetic vortices has been proposed in Ref. [Boh08] as the vortex random access memory (VRAM). The memory like writing process demonstrated in sec-

tion 4.1, adds the aspect of controlling several bits, i.e., vortex polarizations, via only one stripline. Nevertheless, in order to be able to compete with the access times and the storage density of current random access memories a lot of more research is necessary. A straight forward approach is to stack the vortices in order to obtain a third dimension [Win13; Gus05] which is also desirable in the field of magnonics [Kra14; Kru10b]. For such stacked vortices novel, direct core-core interactions are expected. In addition, physical aspects like the Dzyaloshinskii-Moriya interaction [Dzy58; Mor60] are promising candidates to be included into the vortex dynamics. For example, it has recently been shown that such interaction is able to triple the gyration frequency of vortices [Che15]. The same interaction is known to stabilize skyrmion lattices in ultrathin films due to the proximity to an asymmetric sample design featuring an adjacent layer with strong spin-orbit coupling [Sam13]. It has been shown in Ref. [Dai13] that magnetic skyrmions can also be stable as a ground state without Dzyaloshinskii-Moriya interaction in magnetic microdisks. When initially deflected, the skyrmions also show gyrotropic motions around the center of the containing Co/Ru/Co nanodisk. Such similarities to the magnetic vortices presented in this work suggest that the findings are applicable to magnetic skyrmions as well. Nevertheless, in contrast to skyrmions, vortices are also stable in the absence of external magnetic fields. Consequently, they feature two statically degenerate ground states with crucially different dynamics, characterized by the polarization. In order to apply the findings on self-organized state formation to skyrmion arrangements, it would be necessary to implement such behavior for skyrmions as well. This would complement studies that propose magnetic skyrmions as information carriers in ultra-dense memory and logic devices [Fer13]. Apart from the application-oriented memory aspect, coupled vortices understood as artificial (frustrated) crystals are certainly interesting from a fundamental researcher's point of view. This work comprehensively examined the aspect of self-organized state formation that can build a basis for logic and memory applications based on the polarization of magnetic quasi-particles as information carrier.

Bibliography

- [Ado13] C. F. Adolff et al. “Self-organized state formation in magnonic vortex crystals”. *Phys. Rev. B* **88**, 224425 (2013).
DOI: 10.1103/PhysRevB.88.224425.
- [Ado15] C. F. Adolff et al. “Gyrational modes of benzenelike magnetic vortex molecules”. *Phys. Rev. B* **92**, 024426 (2015).
DOI: 10.1103/PhysRevB.92.024426.
- [Aha00] A. Aharoni. *Introduction to the Theory of Ferromagnetism*. International Series of Monographs on Physics. Clarendon Press, 2000.
- [All14] *Positive PMMA E-Beam Resists AR-P 630 - 670 series*. Allresist. 2014.
- [Beh15] C. Behncke et al. “Band structure engineering of two-dimensional magnonic vortex crystals”. *Phys. Rev. B* **91**, 224417 (2015).
DOI: 10.1103/PhysRevB.91.224417.
- [Boh08] S. Bohlens et al. “Current controlled random-access memory based on magnetic vortex handedness”. *Appl. Phys. Lett.* **93**, 142508 (2008).
DOI: 10.1063/1.2998584.
- [Bro59] W. F. Brown. “Micromagnetics, Domains, and Resonance”. *J. Appl. Phys.* **30**, 62 (1959).
DOI: 10.1063/1.2185970.
- [Cha12] W. Chao et al. “Real space soft x-ray imaging at 10 nm spatial resolution”. *Opt. Express* **20**, 9777 (2012).
DOI: 10.1364/OE.20.009777.
- [Che15] S. Chen et al. “Effect of Dzyaloshinskii-Moriya interaction on the magnetic vortex oscillator driven by spin-polarized current”. *J. Appl. Phys.* **117**, 17B720 (2015).
DOI: 10.1063/1.4915476.
- [Che95] C. T. Chen et al. “Experimental Confirmation of the X-Ray Magnetic Circular Dichroism Sum Rules for Iron and Cobalt”. *Phys. Rev. Lett.* **75**, 152 (1995).
DOI: 10.1103/PhysRevLett.75.152.

- [Cho04] S.-B. Choe et al. “Vortex Core-Driven Magnetization Dynamics”. *Science* **304**, 420 (2004).
DOI: 10.1126/science.1095068.
- [Dai13] Y. Y. Dai et al. “Skyrmion ground state and gyration of skyrmions in magnetic nanodisks without the Dzyaloshinsky-Moriya interaction”. *Phys. Rev. B* **88**, 054403 (2013).
DOI: 10.1103/PhysRevB.88.054403.
- [Die08] C. Dietrich et al. “Influence of perpendicular magnetic fields on the domain structure of permalloy microstructures grown on thin membranes”. *Phys. Rev. B* **77**, 174427 (2008).
DOI: 10.1103/PhysRevB.77.174427.
- [Dre09] A. Drews. “Dynamics of magnetic vortices and antivortices”. *Dissertation, Universität Hamburg* (2009).
- [Dre12] A. Drews et al. “Nonlinear magnetic vortex gyration”. *Phys. Rev. B* **85**, 144417 (2012).
DOI: 10.1103/PhysRevB.85.144417.
- [Dzy58] I. Dzyaloshinsky. “A thermodynamic theory of ”weak” ferromagnetism of antiferromagnetics”. *J. Phys. Chem. Solids* **4**, 241 (1958).
DOI: 10.1016/0022-3697(58)90076-3.
- [Fer13] A. Fert et al. “Skyrmions on the track”. *Nat. Nano.* **8**, 152 (2013).
DOI: 10.1038/nnano.2013.29.
- [Fit06] M. R. Fitzsimmons et al. “Surface oxidation of Permalloy thin films”. *Phys. Rev. B* **73**, 014420 (2006).
DOI: 10.1103/PhysRevB.73.014420.
- [Gal07] M. Galassi et al. “The GNU Scientific Library Reference Manual, 2007”. URL <http://www.gnu.org/software/gsl>. ISBN **954161734** (2007).
- [Gil56] T. L. Gilbert. “Formulation, Foundations and Applications of the Phenomenological Theory of Ferromagnetism”. *Dissertation, Illinois Institute of Technology* (1956).
- [Gol03] D. Goll et al. “Critical thickness for high-remanent single-domain configurations in square ferromagnetic thin platelets”. *Phys. Rev. B* **67**, 094414 (2003).
DOI: 10.1103/PhysRevB.67.094414.
- [Gra00] I. S. Gradshteyn et al. “Table of integrals, series, and products. Translated from the Russian. Translation edited and with a preface by Alan Jeffrey and Daniel Zwillinger”. *Academic Press, Inc., San Diego, CA* (2000).

-
- [Gus01a] K. Y. Guslienko et al. “Field evolution of magnetic vortex state in ferromagnetic disks”.
Appl. Phys. Lett. **78**, 3848 (2001).
DOI: 10.1063/1.1377850.
- [Gus01b] K. Y. Guslienko et al. “Magnetization reversal due to vortex nucleation, displacement, and annihilation in submicron ferromagnetic dot arrays”.
Phys. Rev. B **65**, 024414 (2001).
DOI: 10.1103/PhysRevB.65.024414.
- [Gus02] K. Y. Guslienko et al. “Eigenfrequencies of vortex state excitations in magnetic sub-micron-size disks”.
J. Appl. Phys. **91**, 8037 (2002).
DOI: 10.1063/1.1450816.
- [Gus05] K. Y. Guslienko et al. “Dynamics of coupled vortices in layered magnetic nanodots”.
Appl. Phys. Lett. **86**, 223112 (2005).
DOI: 10.1063/1.1929078.
- [Han13] D.-S. Han et al. “Wave modes of collective vortex gyration in dipolar-coupled-dot-array magnonic crystals”.
Sci. Rep. **3**, 2262 (2013).
DOI: 10.1038/srep02262.
- [Hän13] M. Hänze. “Dynamics of magnonic vortex crystals”.
Masterarbeit, Institut für Angewandte Physik und Zentrum für Mikrostrukturforschung der Universität Hamburg (2013).
- [Hän14] M. Hänze et al. “Tunable eigenmodes of coupled magnetic vortex oscillators”.
Appl. Phys. Lett. **104**, 182405 (2014).
DOI: 10.1063/1.4875618.
- [Hän15] M. Hänze et al. “Burst-mode manipulation of magnonic vortex crystals”.
Phys. Rev. B **91**, 104428 (2015).
DOI: 10.1103/PhysRevB.91.104428.
- [Imr06] A. Imre et al. “Majority Logic Gate for Magnetic Quantum-Dot Cellular Automata”.
Science **311**, 205–208 (2006).
DOI: 10.1126/science.1120506.
- [Jai12] S. Jain et al. “From chaos to selective ordering of vortex cores in interacting mesomagnets”.
Nat. Commun. **3**, 1330 (2012).
DOI: 10.1038/ncomms2331.

- [Jun11] H. Jung et al. “Tunable negligible-loss energy transfer between dipolar-coupled magnetic disks by stimulated vortex gyration”.
Sci. Rep. **1** (2011).
DOI: 10.1038/srep00059.
- [Kam11] T. Kamionka et al. “Influence of temperature on the gyrotropic eigenmode of magnetic vortices”.
Phys. Rev. B **83**, 224424 (2011).
DOI: 10.1103/PhysRevB.83.224424.
- [Kam12] T. Kamionka. “Polarisationsumkehr magnetischer Vortizes und Antivortices”.
Dissertation, Institut für Angewandte Physik und Zentrum für Mikrostrukturforschung der Universität Hamburg (2012).
- [Kit76] C. Kittel. *Introduction to solid state physics*. **8**. Wiley New York, 1976.
- [Kra14] M. Krawczyk et al. “Review and prospects of magnonic crystals and devices with reprogrammable band structure”.
J. Phys. Condens. Matter **26**, 123202 (2014).
DOI: 10.1088/0953-8984/26/12/123202.
- [Kro62] H. Kronmüller. “Mikromagnetische Berechnung der Magnetisierung in der Umgebung unmagnetischer Einschlüsse in Ferromagnetika”. German.
Zeitschrift für Physik **168**, 478 (1962).
DOI: 10.1007/BF01378144.
- [Kru10a] V. V. Kruglyak et al. “Magnonics”.
J. Phys. D: Appl. Phys. **43**, 260301 (2010).
DOI: 10.1088/0022-3727/43/26/260301.
- [Kru10b] V. V. Kruglyak et al. “Magnonics”.
J. Phys. D: Appl. Phys. **43**, 264001 (2010).
DOI: 10.1088/0022-3727/43/26/264001.
- [Krü07] B. Krüger et al. “Harmonic oscillator model for current- and field-driven magnetic vortices”.
Phys. Rev. B **76**, 224426 (2007).
DOI: 10.1103/PhysRevB.76.224426.
- [Krü08] B. Krüger et al. “Vortices and antivortices as harmonic oscillators”.
J. Appl. Phys. **103**, 07A501 (2008).
DOI: 10.1063/1.2830011.
- [Kum14] D. Kumar et al. “Magnetic Vortex Based Transistor Operations”.
Sci. Rep. **4**, 4108 (2014).
DOI: 10.1038/srep04108.
- [Kys75] D. F. Kyser et al. “Monte Carlo simulation of spatially distributed beams in electron beam lithography”.
J. Vac. Sci. Technol. **12**, 1305 (1975).
DOI: 10.1116/1.568524.

-
- [Lad10] S. Ladak et al. “Direct observation of magnetic monopole defects in an artificial spin-ice system”.
Nat. Phys. **6**, 359 (2010).
DOI: 10.1038/nphys1628.
- [Lam10] P. E. Lammert et al. “Direct entropy determination and application to artificial spin ice”.
Nat. Phys. **6**, 786 (2010).
DOI: 10.1038/nphys1728.
- [Lan12] H. H. Langner et al. “Vortex dynamics in nonparabolic potentials”.
Phys. Rev. B **85**, 174436 (2012).
DOI: 10.1103/PhysRevB.85.174436.
- [Lan35] L. D. Landau et al. “On the theory of the dispersion of magnetic permeability in ferromagnetic bodies”.
Phys. Z. Sowjetunion **8**, 101–114 (1935).
- [Len11] B. Lenk et al. “The building blocks of magnonics”.
Phys. Rep. **507**, 107 (2011).
DOI: 10.1016/j.physrep.2011.06.003.
- [Li10] J. Li et al. “Comparing artificial frustrated magnets by tuning the symmetry of nanoscale permalloy arrays”.
Phys. Rev. B **81**, 092406 (2010).
DOI: 10.1103/PhysRevB.81.092406.
- [Liu07] Z. Liu et al. “Spin Wave Dynamics and the Determination of Intrinsic Damping in Locally Excited Permalloy Thin Films”.
Phys. Rev. Lett. **98**, 087201 (2007).
DOI: 10.1103/PhysRevLett.98.087201.
- [Mak12] I. Makhfudz et al. “Inertia and Chiral Edge Modes of a Skyrmion Magnetic Bubble”.
Phys. Rev. Lett. **109**, 217201 (2012).
DOI: 10.1103/PhysRevLett.109.217201.
- [Mar12] M. Martens et al. “Influence of the winding number on field- and current driven dynamics of magnetic vortices and antivortices”.
J. Appl. Phys. **112**, 013917 (2012).
DOI: 10.1063/1.4730637.
- [Mar13] M. Martens et al. “Phase diagram for magnetic vortex core switching studied by ferromagnetic absorption spectroscopy and time-resolved transmission x-ray microscopy”.
Phys. Rev. B **87**, 054426 (2013).
DOI: 10.1103/PhysRevB.87.054426.

- [Mar14] M. Martens. “Dynamics of magnetic vortices and antivortices studied by ferromagnetic absorption spectroscopy and transmission x-ray microscopy”. *Dissertation, Institut für Angewandte Physik und Zentrum für Mikrostrukturforschung der Universität Hamburg* (2014).
- [Mej06] J. Mejía-López et al. “Vortex state and effect of anisotropy in sub-100-nm magnetic nanodots”. *J. Appl. Phys.* **10**, 104319 (2006).
DOI: 10.1063/1.2364599.
- [Men08] E. Mengotti et al. “Building blocks of an artificial kagome spin ice: Photoemission electron microscopy of arrays of ferromagnetic islands”. *Phys. Rev. B* **78**, 144402 (2008).
DOI: 10.1103/PhysRevB.78.144402.
- [Mor60] T. Moriya. “Anisotropic Superexchange Interaction and Weak Ferromagnetism”. *Phys. Rev.* **120**, 91 (1960).
DOI: 10.1103/PhysRev.120.91.
- [MPI14] M. P. I. for Intelligent Systems. *X-Ray Microscopy*. (2014). URL: http://www.is.mpg.de/schuetz/x-ray_microscopy.
- [Nak05] Y. Nakatani et al. “Head-to-head domain walls in soft nano-strips: a refined phase diagram”. *J. Magn. Magn. Mater.* **290**, 750 (2005).
DOI: 10.1016/j.jmmm.2004.11.355.
- [Ono12] Y. Onose et al. “Observation of Magnetic Excitations of Skyrmion Crystal in a Helimagnetic Insulator Cu_2OSeO_3 ”. *Phys. Rev. Lett.* **109**, 037603 (2012).
DOI: 10.1103/PhysRevLett.109.037603.
- [Pue15] M. F. A. Pues. “Magnetic microscopy and spectroscopy of excitations in nanostructured ferromagnetic alloys”. *Dissertation, Institut für Angewandte Physik und Zentrum für Mikrostrukturforschung der Universität Hamburg* (2015).
- [Rom15] N. Romming et al. “Field-Dependent Size and Shape of Single Magnetic Skyrmions”. *Phys. Rev. Lett.* **114**, 177203 (2015).
DOI: 10.1103/PhysRevLett.114.177203.
- [Sam13] J. Sampaio et al. “Nucleation, stability and current-induced motion of isolated magnetic skyrmions in nanostructures.” *Nat. Nano.* **8**, 839 (2013).
DOI: 10.1038/nnano.2013.210.

-
- [Sch87] G. Schütz et al. “Absorption of circularly polarized x rays in iron”.
Phys. Rev. Lett. **58**, 737 (1987).
DOI: 10.1103/PhysRevLett.58.737.
- [Shi00] T. Shinjo et al. “Magnetic Vortex Core Observation in Circular Dots of Permalloy”.
Science **289**, 930 (2000).
DOI: 10.1126/science.289.5481.930.
- [Shi03] J. Shibata et al. “Dynamics of magnetostatically coupled vortices in magnetic nanodisks”.
Phys. Rev. B **67**, 224404 (2003).
DOI: 10.1103/PhysRevB.67.224404.
- [Shi04] J. Shibata et al. “Magnetic vortex dynamics in a two-dimensional square lattice of ferromagnetic nanodisks”.
Phys. Rev. B **70**, 012404 (2004).
DOI: 10.1103/PhysRevB.70.012404.
- [Sil99] T. J. Silva et al. “Inductive measurement of ultrafast magnetization dynamics in thin-film Permalloy”.
J. Appl. Phys. **85**, 7849 (1999).
DOI: 10.1063/1.370596.
- [Ste14] F.-U. Stein et al. “Direct observation of internal vortex domain-wall dynamics”.
Phys. Rev. B **89**, 024423 (2014).
DOI: 10.1103/PhysRevB.89.024423.
- [Sto15] H. Stoll et al. “Imaging Spin Dynamics on the Nanoscale using X-Ray Microscopy”.
Front. Phys. **3** (2015).
DOI: 10.3389/fphy.2015.00026.
- [Sto38] E. C. Stoner. “Collective Electron Ferromagnetism”.
Proceedings of the Royal Society of London A: Mathematical, Physical and Engineering Sciences **165**, 372 (1938).
DOI: 10.1098/rspa.1938.0066.
- [Stö06] J. Stöhr et al. “Magnetism: From Fundamentals to Nanoscale Dynamics”.
Springer Series in Solid-state Sciences S. (2006).
DOI: 10.1007/978-3-540-30283-4.
- [Sug11] S. Sugimoto et al. “Dynamics of Coupled Vortices in a Pair of Ferromagnetic Disks”.
Phys. Rev. Lett. **106**, 197203 (2011).
DOI: 10.1103/PhysRevLett.106.197203.

- [Suk13] O. V. Sukhostavets et al. “Probing the Anharmonicity of the Potential Well for a Magnetic Vortex Core in a Nanodot”.
Phys. Rev. Lett. **111**, 247601 (2013).
DOI: 10.1103/PhysRevLett.111.247601.
- [Suk15] O. V. Sukhostavets et al. “Fine structure of excitation spectra of magnetic vortex dot clusters”.
Appl. Phys. Express **8**, 023002 (2015).
DOI: 10.7567/APEX.8.023002.
- [Thi73] A. A. Thiele. “Steady-State Motion of Magnetic Domains”.
Phys. Rev. Lett. **30**, 230 (1973).
DOI: 10.1103/PhysRevLett.30.230.
- [Tho09] A. C. Thompson et al. “X-Ray Data Booklet”.
Lawrence Berkeley National Laboratory, University of California (2009).
- [Vog10] A. Vogel et al. “Influence of Dipolar Interaction on Vortex Dynamics in Arrays of Ferromagnetic Disks”.
Phys. Rev. Lett. **105**, 037201 (2010).
DOI: 10.1103/PhysRevLett.105.037201.
- [Vog11] A. Vogel et al. “Coupled Vortex Oscillations in Spatially Separated Permalloy Squares”.
Phys. Rev. Lett. **106**, 137201 (2011).
DOI: 10.1103/PhysRevLett.106.137201.
- [Vog12] A. Vogel et al. “Direct imaging of phase relation in a pair of coupled vortex oscillators”.
AIP Adv. **2**, 042180 (2012).
DOI: 10.1063/1.4771683.
- [VWa06] B. Van Waeyenberge et al. “Magnetic vortex core reversal by excitation with short bursts of an alternating field”.
Nature **444**, 461 (2006).
DOI: 10.1038/nature05240.
- [Wac02] A. Wachowiak et al. “Direct Observation of Internal Spin Structure of Magnetic Vortex Cores”.
Science **298**, 577 (2002).
DOI: 10.1126/science.1075302.
- [Wan14] X. Wang et al. “Time-resolved photoemission electron microscopy imaging of mode coupling between three interacting magnetic vortices”.
Appl. Phys. Lett. **105**, 102408 (2014).
DOI: 10.1063/1.4895070.

- [Wil34] E. B. Wilson. “The Normal Modes and Frequencies of Vibration of the Regular Plane Hexagon Model of the Benzene Molecule”.
Phys. Rev. **45**, 706 (1934).
DOI: 10.1103/PhysRev.45.706.
- [Win13] S. Wintz et al. “Topology and Origin of Effective Spin Meron Pairs in Ferromagnetic Multilayer Elements”.
Phys. Rev. Lett. **110**, 177201 (2013).
DOI: 10.1103/PhysRevLett.110.177201.
- [WolV9] I. Wolfram Research. “Mathematica Version 9”.
Champaign, Illinois (2012).
- [Woo15] S. Woo et al. “Observation of room temperature magnetic skyrmions and their current-driven dynamics in ultrathin Co films”.
arXiv: **1502.07376** (2015).

Appendix A.

Appendices

A.1. List of Publications

This is a full list of publications the author of this work has contributed to. The publications are not ordered chronologically but sorted by relevance for the context of this thesis. The full references (including DOI) can be found in the Bibliography. The first author of each contribution led the composition of the manuscript. Additional contributions of each author from the group in Hamburg to the research study are indicated using the following specifications:

1. Conception and supervision of the research study
2. Sample preparation
3. Measurements
4. Analytical/Numerical calculations
5. Micromagnetic simulations
6. Data analysis and interpretation
7. Composition of the manuscript

[Ado13] Christian F. Adolff^{1,2,3,4,5,6,7}, Max Hänze^{2,3,4,5,6,7}, Andreas Vogel^{1,3,7}, Markus Weigand, Michael Martens⁶, and Guido Meier^{1,7}. "Self-organized state formation in magnonic vortex crystals." *Phys. Rev. B* **88**, 224425 (2013).

[Ado15] Christian F. Adolff^{1,2,3,4,6,7} and Max Hänze^{3,4,6,7} and Matthias F. A. Pues⁶ and Markus Weigand and Guido Meier^{1,7}. "Gyrational modes of benzene-like magnetic vortex molecules." *Phys. Rev. B* **92**, 024426 (2015).

- [Sto15]** Hermann Stoll, Matthias Noske, Markus Weigand, Kornel Richter, Benjamin Krüger, Robert M. Reeve, Max Hänze^{1,2,3,4,5,6,7}, Christian F. Adolff^{1,2,3,4,5,6,7}, Falk-Ulrich Stein^{1,2,3,4,5,6,7}, Guido Meier^{1,7}, Mathias Kläui, and Gisela Schütz. "Imaging Spin Dynamics on the Nanoscale using X-Ray Microscopy." *Front. Phys.* **3**, 26 (2015)
- [Hän15]** Max Hänze^{1,2,3,4,6,7}, Christian F. Adolff^{1,3,7}, Markus Weigand, and Guido Meier^{1,7}. "Burst-mode manipulation of magnonic vortex crystals." *Phys. Rev. B* **91**, 104428 (2015)
- [Hän14]** Max Hänze^{1,2,3,4,6,7}, Christian F. Adolff^{1,2,3,4,6,7}, Markus Weigand, and Guido Meier^{1,7}. "Tunable eigenmodes of coupled magnetic vortex oscillators." *Appl. Phys. Lett.* **104**, 182405 (2014)
- [Beh15]** Carolin Behncke^{1,2,3,4,6,7}, Max Hänze^{1,2,3,4,6,7}, Christian F. Adolff^{3,6,7}, Markus Weigand, and Guido Meier^{1,7}. "Band structure engineering of two-dimensional magnonic vortex crystals." *Phys. Rev. B.* **91**, 224417 (2015)
- [Lan12]** Hauke H. Langner^{1,2,3,4,5,6,7}, Thomas Kamionka^{1,4,6}, Michael Martens^{4,5,6}, Markus Weigand, Christian F. Adolff^{5,6}, Ulrich Merkt^{1,7}, and Guido Meier^{1,7}. "Vortex dynamics in nonparabolic potentials." *Phys. Rev. B* **85**, 174436 (2012)

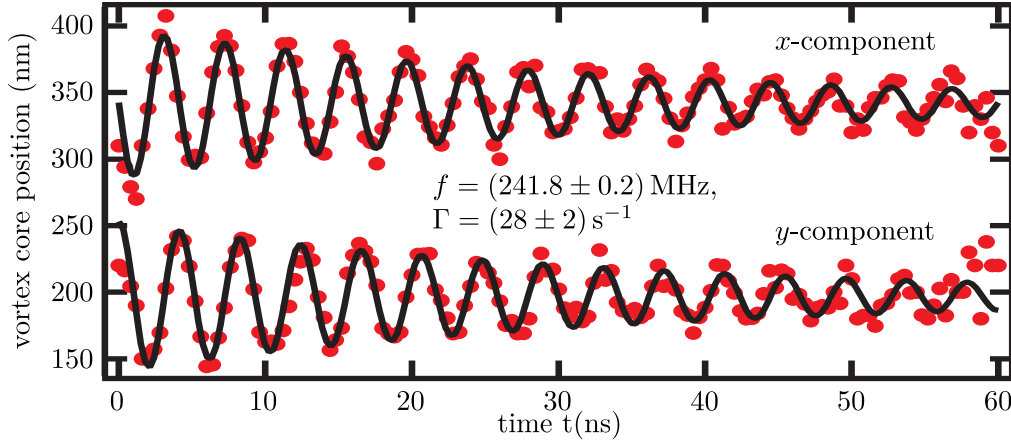


Figure A.1.: Identification of resonance frequency and damping for the eigenmode of an isolated vortex. The data (red dots) is determined by transmission x-ray microscopy and is then compared to an exponentially damped circular trajectory (black fit-curve).

A.2. Model Parameters

In order to perform the numerical calculations presented in this thesis, several parameters of the model have to be determined. The thickness h of the disks is measured using atomic force microscopy. Scanning electron microscopy is used to determine the radii R of the disks and the disk interdistance D . Other experimentally measured characteristics are the frequency and the damping of the gyrotropic eigenmode of a vortex in an isolated disk. Supplementary Figure A.1 shows the x -component and y -component of this eigenmode extracted from transmission X-ray measurements of an isolated disk that has been prepared onto the same sample as the actually investigated vortex arrangement (here: ring-molecule with eight vortices presented in chapter 5). The vortex is deflected with a short field pulse of 1.8 ns and then relaxes on a spiral trajectory back to its equilibrium position. A damped gyration of the form

$$\vec{x} = \begin{pmatrix} x_0 \\ y_0 \end{pmatrix} + \begin{pmatrix} \cos(2\pi f_{\text{iso}}t + \varphi) \\ p \sin(2\pi f_{\text{iso}}t + \varphi) \end{pmatrix} \exp(-\Gamma t) \quad (\text{A.1})$$

is fitted to the experimentally determined vortex trajectory. As can be seen from Fig. A.1, the resonance frequency of the isolated vortex and the damping can be determined precisely for a single disk. Nevertheless further measurements show that the resonance frequencies of other isolated disks on the same sample vary about ± 15 MHz. Thus, the used model parameter $\omega_0 \approx 2\pi f_{\text{iso}}$ is chosen within this accuracy. Besides the saturation

magnetization, that is chosen to be $M_S = 800 \text{ kA m}^{-1}$ [Krü07], only the parameter s remains that modifies the coupling strength. As mentioned in the main text it is predicted from experiments and theory that the coupling strength is overestimated by the rigid vortex approach [Sug11; Vog12; Suk13]. It follows that $s < 1$. Typically a value of $s \approx \frac{2}{3}$ fits best for the experiments¹. Nevertheless, for the last experiment on benzene-like magnetic vortex molecules, a value of $s = 0.483$ had to be used to obtain a good accordance with the experiments when a homogeneous polarization pattern is present. Since the experiments with the same sample but an alternating polarization pattern do not deviate from the $s \approx \frac{2}{3}$ -rule, a deviation because of preparation inaccuracies is unlikely. In addition, the experiments show that the bandwidths for the two polarization patterns vary with a factor of three. Such factor is expected from the analytical calculations elaborated in this work (section 2.2.2 in chapter 2 leading to Eqn. 5.6 in chapter 5) and recent studies on triples of disks (similar to those investigated in section 4.3) presented by Sukhostavets et al. in Ref. [Suk15]. In contrast, this factor would not follow from the numerical calculation if the parameter s was not reduced for the homogenous case. When considering the experiment on triples presented in this work (Fig. 4.11) one can see that the numerical calculation also slightly overestimates the bandwidth for the homogeneous pattern.² The deviation between the numerical calculation and the experiments becomes especially visible in the last experiments on the benzene-like magnetic vortex molecules. To face this inaccuracy of the model, we modify the s -parameter depending on the polarization configuration in order to obtain a better comparability to the experiments. The reasons for the deviations are yet unclear. Interestingly, the relative bandwidths are correctly predicted in the analytical calculations (factor 3 in Eqn. 5.6) that assume pure dipolar coupling and circular trajectories. Possibly, the trajectories in the experiments show lower ellipticities than expected from the Thiele model. This might be due to a concentric deformation of the disks that arises from surface tensions in the membrane on which the microstructures are fabricated [Die08].

A list of the model parameters for all results (figures) presented in this work is depicted in the following table.

¹This is also in accordance with private communications with Prof. Dr. Konstantin Guslienko at a poster session at the IEEE International Magnetic Conference (INTERMAG) in Dresden, from May 4th to May 8th 2014.

²Interestingly, the recent studies of Wang et al. in Ref. [Wan14] on triples also show deficiencies in the theoretical models with regards to experimentally observed behavior for the homogenous polarization pattern.

figure	f (MHz)	Γ (10^6 s^{-1})	s (1)	D (μm)	R (μm)	h (nm)
2.4	227.6	29.0	0.66	—	1.0	60.0
2.6	227.6	29.0	0.66	2.05	1.0	60.0
2.9	227.6	29.0	0.66	4.0	1.0	60.0
4.2	238.0	26.0	0.6875	3.0	1.0	60.0
4.3	238.0	26.0	0.6875	2.25	1.0	60.0
4.4(a)	223.0	25.0	0.6	3.0	1.0	60.0
4.4(b)	223.0	25.0	0.6	2.25	1.0	60.0
4.9	300.0	37.0	0.7	1.15	0.475	40.0
4.10	245.0	25.0	0.6667	2.063	1.0	60.0
4.11	207.0	23.0	0.6	2.05	1.0	55.0
4.12	207.0	—	0.6	2.05	1.0	55.0
5.3	226.0	25.0	0.6875	2.05	1.0	53.0
5.4	234.2	28.5	0.6875	2.06	0.995	60.0
5.6	227.6	29.0	0.6875	2.06	0.995	60.0
5.7	227.6	29.0	0.4583	2.06	0.995	60.0

Table A.1.: Model parameters used for the numerical calculations.

A.3. Auxiliary Calculations

The analytical model elaborated in section 2.2.2 has been used to explain several experimental results presented in this thesis. Starting from Eqn.

$$\omega_e - \omega_{\text{iso}} = \frac{1}{2\pi} \frac{1}{G'_0 Z_{N,e}} \sum_{i=0}^{N-1} \sum_{j \neq i} \int_{\omega t=0}^{\omega t=2\pi} E_{\text{dipole},ij} d(\omega t). \quad (\text{A.2})$$

(originally tagged as Eqn. 2.30) Eqns.2.32, 5.5, and 5.6 have directly been deduced without depicting the intermediate steps of calculation. Those are in most cases straight forward but include several trigonometric identities. Practically the calculations have been performed using the software *Wolfram Mathematica* [WolV9] but in order to get a deeper understanding of the calculation, the auxiliary calculations will be given in detail in the following.

Pair of disks (proof of Eqn. 2.32)

A pair (1,2) of disks that is located at $\vec{r}_1 = (0, 0)^T$, $\vec{r}_2 = (D \cos \vartheta, D \sin \vartheta)^T$ is regarded. The unidirectional alternating magnetic field points in y -direction ($\xi = \frac{\pi}{2}$). Consequently the trajectory of an isolated un-damped vortex in resonance constituting the approximation for the coupled motion of the vortices is given by

$$\vec{x}_i = a_i C_i \begin{pmatrix} \cos(\omega_e t + \varphi_i) \\ p_i \sin(\omega_e t + \varphi_i) \end{pmatrix} \quad (\text{A.3})$$

according to Eqn. 2.22. The magnetic dipole moments $\vec{\mu}_i$ are rotated by $\pm 90^\circ$ (see Eqn. 2.20) and are thus given by

$$\vec{\mu}_i = \tilde{a}_i \begin{pmatrix} -p_i \sin(\omega_e t + \varphi_i) \\ \cos(\omega_e t + \varphi_i) \end{pmatrix} \quad (\text{A.4})$$

Due to the approximation of weak coupling ($\frac{D}{2R} \geq 2$) it is assumed that the vortices are affected by the alternating field in an identical fashion so that only an in-phase motion can be excited resonantly at ω_p and relation 2.31 applies. This yields

$$a_1 = a_2 = a, \quad \varphi_1 = \varphi_2 = \varphi, \quad \omega_e = \omega_p. \quad (\text{A.5})$$

Now all preliminaries to solve Eqn. A.2 are given. For that, we divide the integration of the dipole energy into two parts. Inserting Eqn. 2.21 yields

$$\begin{aligned} \int_0^{2\pi} E_{\text{dipole},12} d(\omega_p t) &= \frac{\mu_0}{4\pi D_{12}^3} \left(\int_0^{2\pi} \vec{\mu}_1 \vec{\mu}_2 d(\omega_p t) - \frac{3}{D_{12}^2} \int_0^{2\pi} (\vec{\mu}_1 \vec{D}_{12})(\vec{\mu}_2 \vec{D}_{12}) d(\omega_p t) \right) \\ &=: \frac{\mu_0}{4\pi D_{12}^3} \left(I_a - \frac{3}{D_{12}^2} I_b \right) \end{aligned} \quad (\text{A.6})$$

It follows that

$$I_a = \int_0^{2\pi} \left(\cos^2(\omega_p t + \varphi) + p_1 p_2 \sin^2(\omega_p t + \varphi) \right) d(\omega t) = \tilde{a}^2 \pi (1 + p_1 p_2) \quad (\text{A.7})$$

for the first integral. With $\vec{D}_{12} := \vec{r}_1 - \vec{r}_2 = -\vec{r}_2$ and $D_{12} := |\vec{D}_{12}| = D$ the second integral can be simplified to

$$\begin{aligned} I_b &= \tilde{a}^2 D^2 \int_0^{2\pi} \left(\cos^2(\omega_p t + \varphi) \sin^2 \vartheta + p_1 p_2 \sin^2(\omega_p t + \varphi) \cos^2 \vartheta \right) d(\omega_p t) \\ &= \tilde{a}^2 D^2 \pi \left(\sin^2 \vartheta + p_1 p_2 \cos^2 \vartheta \right) = \frac{\tilde{a}^2 D^2 \pi}{2} \left((1 + p_1 p_2) + (p_1 p_2 - 1) \cos(2\vartheta) \right) \end{aligned} \quad (\text{A.8})$$

Inserting this into Eqn. A.6 yields

$$\int_0^{2\pi} E_{\text{dipole},12} d(\omega t) = -\frac{\mu_0 \tilde{a}^2 \pi}{8\pi D^3} \left((1 + p_1 p_2) + 3(p_1 p_2 - 1) \cos(2\vartheta) \right) \quad (\text{A.9})$$

for the integrated dipole energy. Inserting this and the abbreviation $Z_{N,e} = \sum_1^2 \vec{x}_i^2 = 2a^2$ into Eqn. A.2 yields

$$\begin{aligned} \omega_p - \omega_{\text{iso}} &= \frac{1}{2\pi} \frac{1}{G'_0 2a^2} 2 \left(-\frac{\mu_0 \tilde{a}^2 \pi}{8\pi D^3} \left((1 + p_1 p_2) + 3(p_1 p_2 - 1) \cos(2\vartheta) \right) \right) \\ &= -\frac{\tilde{a}^2}{a^2} \frac{\mu_0}{16\pi D^3 G'_0} \left[(1 + p_1 p_2) + 3(p_1 p_2 - 1) \cos(2\vartheta) \right] \end{aligned} \quad (\text{A.10})$$

This equals Eqn. 2.32. □

Ring-Molecules

In the following two proofs an even number of N vortices $(0, 1, \dots, N-1)$ that are located at

$$\vec{r}_i = r_c \begin{pmatrix} \sin(i\alpha) \\ -\cos(i\alpha) \end{pmatrix} \quad \text{with } \alpha = \frac{2\pi}{N} \quad (\text{A.11})$$

are regarded, whereas the radius of the ring is denoted with $r_c = \frac{D}{\sqrt{2(1-\cos\alpha)}}$. The unidirectional alternating magnetic field points in y -direction ($\xi = \frac{\pi}{2}$). Consequently the approximation for the coupled motions of the vortices is given by Eqn. A.3 and the gyration of the corresponding dipoles by Eqn. A.4. Due to the symmetry of the system it is assumed that there are N normal modes that are characterized by the dimensionless wave number κ . They are given by

$$a_i = a_\kappa \quad \varphi_i = i\kappa\alpha + ip_i\alpha, \quad \omega_e = \omega_\kappa. \quad (\text{A.12})$$

Case 1: Homogeneous Polarizations (proof of Eqn. 5.5)

In the case homogeneous polarizations $p_i = p$ it can be motivated from the experiments and numerical calculations presented in Fig. 5.6 that each normal mode can be excited at a different frequency. Consequently the rotating dipoles are given by

$$\vec{\mu}_{i,\kappa} = \tilde{a}_\kappa \begin{pmatrix} -p \sin(\omega_\kappa t + i\kappa\alpha + ip\alpha) \\ \cos(\omega_\kappa t + i\kappa\alpha + ip\alpha) \end{pmatrix} \quad (\text{A.13})$$

In analogy to the previous proof the auxiliary integrals $I_{a,ij}$ and $I_{b,ij}$ for two coupled vortices i and j are given by

$$\begin{aligned} I_{a,ij} &:= \int_0^{2\pi} \vec{\mu}_{i,\kappa} \vec{\mu}_{j,\kappa} d(\omega t), \\ I_{b,ij} &:= \int_0^{2\pi} (\vec{\mu}_{i,\kappa} \vec{D}_{ij})(\vec{\mu}_{j,\kappa} \vec{D}_{ij}) d(\omega t). \end{aligned} \quad (\text{A.14})$$

Using the relations

$$\begin{aligned} \int_0^{2\pi} \cos(z + c_i) \cos(z + c_j) dz &= \int_0^{2\pi} \sin(z + c_i) \sin(z + c_j) dz = \pi \cos(c_i - c_j) \\ \int_0^{2\pi} \cos(z + c_i) \sin(z + c_j) dz &= -\pi \sin(c_i - c_j) \end{aligned} \quad (\text{A.15})$$

with the substitutions $z := \omega_\kappa t$ and $c_i := i(\kappa + p)\alpha$, the auxiliary integrals $I_{a,ij}$ and $I_{b,ij}$ can be simplified to

$$\begin{aligned} I_{a,ij} &= 2\pi \tilde{a}_\kappa^2 \cos((i - j)(\kappa + p)\alpha), \\ I_{b,ij} &= \pi \tilde{a}_\kappa^2 D_{ij}^2 \cos((i - j)(\kappa + p)\alpha) \end{aligned} \quad (\text{A.16})$$

Inserting this into Eqn. A.6 yields

$$I_{E,ij} := \int_0^{2\pi} E_{\text{dipole},ij} d(\omega_\kappa t) = -\frac{\mu_0 \tilde{a}_\kappa^2 \pi}{4\pi D_{ij}^3} \cos((i - j)(\kappa + p)\alpha) \quad (\text{A.17})$$

for the interaction energy $I_{E,ij}$ of two vortices i and j during one period of gyration. Before this is inserted into Eqn. A.2, we rearrange the summations:

$$\begin{aligned} \omega_e - \omega_{\text{iso}} &= \frac{1}{2\pi} \frac{1}{G'_0 Z_{N,e}} \sum_{i=0}^{N-1} \sum_{j \neq i} I_{E,ij} \\ &= \frac{1}{2\pi} \frac{1}{G'_0 Z_{N,e}} \sum_{i=0}^{N-1} \sum_n \left(I_{E,i(i+n)} + I_{E,i(i-n)} \right). \end{aligned} \quad (\text{A.18})$$

Here, n indicates the n^{th} next neighbors. Due to the symmetry of the ring, each vortex has two n^{th} neighbors that have the same distance D_n . Inserting Eqn. A.17 with $I_{E,i(i+n)} = I_{E,i(i-n)}$ and the abbreviation $Z_{N,\kappa} = \sum_0^{N-1} \tilde{x}_i^2 = N a_\kappa^2$ yields

$$\omega_\kappa - \omega_{\text{iso}} = -\frac{1}{2} \frac{1}{G'_0} \frac{\mu_0}{2\pi} \left(\frac{\tilde{a}_\kappa}{a_\kappa} \right)^2 \sum_n \frac{1}{D_n^3} \cos(n(\kappa + p)\alpha). \quad (\text{A.19})$$

When only regarding next-neighbor interaction ($n \in \{1\}$) this is identical to Eqn. 5.5. \square

Case 2: Alternating Polarizations (proof of Eqn. 5.6)

In the case homogeneous polarizations it follows from the symmetry that the modes with identical absolute value of κ are always excited simultaneously. Consequently, the rotating dipoles are given by

$$\begin{aligned}\vec{\mu}_{i,|\kappa|} &= \vec{\mu}_{i,\kappa} + \vec{\mu}_{i,-\kappa} \\ &= \tilde{a}_{|\kappa|} \begin{pmatrix} -p_i \sin(\omega_{|\kappa|}t + i\kappa\alpha + ip_i\alpha) \\ \cos(\omega_{|\kappa|}t + i\kappa\alpha + ip_i\alpha) \end{pmatrix} + \tilde{a}_{\kappa} \begin{pmatrix} -p_i \sin(\omega_{|\kappa|}t - i\kappa\alpha + ip_i\alpha) \\ \cos(\omega_{|\kappa|}t - i\kappa\alpha + ip_i\alpha) \end{pmatrix}\end{aligned}\quad (\text{A.20})$$

for $k \neq 0$ and $k \neq N/2$. For the other two cases, the modes with $\pm\kappa$ are identical and thus the first summand is sufficient. Again we will consider the more general case of n^{th} -neighbor interaction between two vortices i and $(i \pm n)$. Whereas this time the polarizations are contrary $p_i p_{i \pm n} = -1$. In analogy to the previous proof, the auxiliary integrals $I_{a,i(i \pm n)}$ and $I_{b,i(i \pm n)}$ are given by

$$\begin{aligned}I_{a,i(i \pm n)} &:= \int_0^{2\pi} \vec{\mu}_{i,|\kappa|} \vec{\mu}_{i \pm n,|\kappa|} d(\omega_{|\kappa|}t), \\ I_{b,i(i \pm n)} &:= \int_0^{2\pi} (\vec{\mu}_{i,|\kappa|} \vec{D})(\vec{\mu}_{i \pm n,|\kappa|} \vec{D}) d(\omega_{|\kappa|}t).\end{aligned}\quad (\text{A.21})$$

Using the relations in Eqn. A.15, the auxiliary integrals result in

$$\begin{aligned}I_{a,i(i \pm n)} &= 0, \\ I_{b,i(i \pm n)} &= -4\pi D_n^2 \tilde{a}^2 \cos(i\kappa\alpha) \cos((i \pm n)\kappa\alpha).\end{aligned}\quad (\text{A.22})$$

for the case $\kappa \neq 0$ and $\kappa \neq N/2$. For the latter simplification the relations

$$D_{n,x}^2 - D_{n,y}^2 = D_n^2 \cos((2i \pm n)\alpha), \quad D_{n,x} D_{n,y} = D_n^2 \sin((2i \pm n)\alpha)\quad (\text{A.23})$$

have been used, whereas $\vec{D}_n = \vec{r}_i - \vec{r}_{(i \pm n)} = (D_{n,x}, D_{n,y})^T$. For the special case $\kappa = 0$ or $\kappa = N/2$ the result has to be divided by two, since the two summands in Eqn. A.20 are identical and thus only one of them has to be considered. Inserting this into Eqn. A.6 yields

$$I_{E,i,(i \pm n)} := \int_0^{2\pi} E_{\text{dipole},i(i \pm n)} d(\omega_{|\kappa|}t) = \frac{3\mu_0 \tilde{a}^2}{D^3} \cos(i\kappa\alpha) \cos((i \pm n)\kappa\alpha)\quad (\text{A.24})$$

Consequently Eq. A.18 results in

$$\begin{aligned}
\omega_e - \omega_{\text{iso}} &= \frac{1}{2\pi} \frac{1}{G'_0 Z_{N,e}} \sum_{i=0}^{N-1} \sum_n \left(I_{E,i(i+n)} + I_{E,i(i-n)} \right) \\
&= \frac{3\tilde{a}^2 \mu_0}{2\pi} \frac{1}{G'_0 Z_{N,e}} \sum_n \frac{1}{D_n^3} \sum_{i=0}^{N-1} 2 \cos^2(i\kappa\alpha) \cos(n\kappa\alpha) \\
&\quad \cdot \begin{cases} \frac{1}{2} & \text{for } \kappa = 0 \text{ or } \kappa = \frac{N}{2} \\ 1 & \text{else.} \end{cases}
\end{aligned} \tag{A.25}$$

Using $Z_{N,e} = 2a^2 N$ and the relation

$$\sum_{i=1}^N \cos^2(i\kappa\alpha) = \begin{cases} N & \text{for } \kappa = 0 \text{ or } \kappa = \frac{N}{2} \\ \frac{N}{2} & \text{else} \end{cases} \tag{A.26}$$

that can be found in mathematic formularies like Ref. [Gra00], the two cases can be merged into

$$\begin{aligned}
\omega_{|\kappa|} - \omega_{\text{iso}} &= \frac{3\tilde{a}^2 \mu_0}{2\pi D^3} \frac{1}{G'_0 2Na^2} \sum_n \cos(n\kappa\alpha) \frac{2N}{2} \\
&= \frac{3}{2} \frac{1}{G'_0} \frac{\mu_0}{2\pi} \left(\frac{\tilde{a}}{a} \right)^2 \sum_n \frac{1}{D_n^3} \cos(n\kappa\alpha)
\end{aligned} \tag{A.27}$$

When only regarding next-neighbor interaction ($n \in \{1\}$) this is identical to Eqn. 5.6 ($B_{\text{hom}} = \frac{1}{G'_0} \frac{\mu_0}{2\pi D^3} \left(\frac{\tilde{a}_\kappa}{a_\kappa} \right)^2$). \square

A.4. Image Processing on Vortex Domain Walls

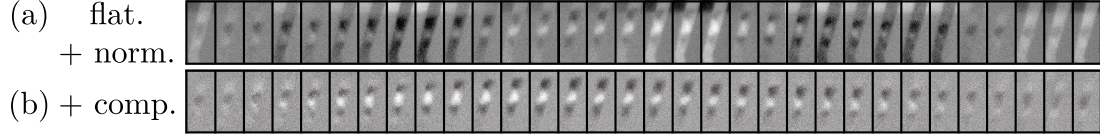


Figure A.2.: Motion of a vortex domain-wall through a wire before (a) and after (b) the compensation of crosstalk-effects. The domain-wall can be identified by the black-white-black contrast [Ste14]. The data is published in Ref. [Ste14]

As described in the chapter 3, an additional image processing step has been developed that allows to isolate the magnetic contrast from parasitic contrast that is due to the crosstalk of the stripline and the avalanche photo diode of the STX microscope. This so-called *compensation* is especially helpful for the evaluation of pulsed measurements where magnetic contrast has to be seen on different transmission levels simultaneously, i.e., beneath and besides the stripline. Such pulsed measurements are not shown in the context of this work. Nevertheless the procedure has been used by Falk-Ulrich Stein *et al.* in Ref. [Ste14] on the direct observation of internal vortex domain-wall dynamics. The study presented in Fig. A.2 shows the movement of a vortex domain-wall through a wire. The vertically aligned wire can be seen as the "blinking" contrast in flattened and normalized image in Fig. A.2(a). An additional stripline is placed horizontally at the top of the images, likewise visible by the blinking contrast. Since pulsed excitations are used, the crosstalk had strongly disguised the magneto dynamics before the compensation was performed. After the compensation, the pure magnetic contrast can clearly be seen in Fig. A.2(b).

A.5. Micromagnetic Simulations of the SOSF in 3×3 Crystals

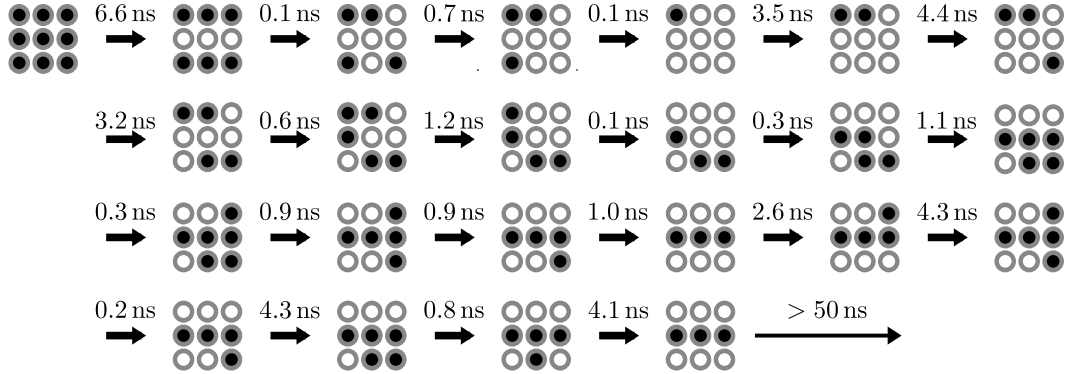


Figure A.3.: Micromagnetic simulation of the emerging polarization states during the self-organized state formation in a 3×3 magnonic vortex crystal. The polarizations are depicted as white or black dots. The simulation lasts 100 ns. The polarization states are evaluated every 0.1 ns. Due to the long simulation times and high memory consumption the disks are reduced in size with respect to the disks that are investigated via scanning transmission x-ray microscopy in chapter 4. The disks are 504 nm in diameter and have a height of 40 nm. The center-to-center distance is 600 nm. The resonance frequency of a single vortex of this geometry is 568 MHz. The frequency of excitation amounts for 570 MHz. The simulation is performed with variable stepsize and a cellsize of $4 \times 4 \times 10 \text{ nm}^3$.

Since the process of polarization switching itself cannot be investigated in the experiment, additional micromagnetic simulations have been performed in order to get a deeper insight into the self-organized state formation. For that a 3×3 crystal is excited with an alternating magnetic field with constant amplitude $\mu_0 H = 3 \text{ mT}$.³ The simulation starts with a homogeneously polarized array. Due to the phenomenon of self-organized state formation the homogeneous polarization state is destroyed and a polarization state with rows of constant polarizations is tuned. During the formation process, several transient states occur that are depicted in Fig. A.3. The formation eventually reaches the stable state of rows of constant polarizations after 41.3 ns.

³Note that in contrast to the experiments on the 3×3 crystal, the amplitude of the exciting field is not adiabatically reduced but stays constant during the whole simulation. Such "burst-mode" self-organized state formation is investigated in detail in section 4.1.

A.6. Further Results of the SOSF in 3×3 Crystals

excitation frequency	in main text (array 2)	additional arrays	$D = 2.25 \mu\text{m}$
225 MHz			
235 MHz			
245 MHz			
255 MHz			
260 MHz			
excitation frequency	in main text (array 1)	additional arrays	$D = 3 \mu\text{m}$
225 MHz			
235 MHz			
245 MHz			
255 MHz			

Figure A.4.: Summary of all experimentally observed stable patterns of the STXM experiments on 3×3 crystals presented in chapter 4. Two types of samples are investigated that vary in disk-interdistance D . In the main text one array of each type is presented. Measurements on arrays with identical geometry reproduce the results discussed in the main text. Eleven samples have been investigated in total. Six samples for the small interdistance and five samples for the large interdistance. Note that not all samples have been measured at all frequencies.

A.7. Process Parameters

substructure	process	product/machine	parameters
microdisks	spin coat	PMMA 50K	6000 U/min, 60 s, accel. 6000
	bake	hotplate	30 s, 160 °C
	spin coat	PMMA 950K	6000 U/min, 60 s, accel. 6000
	bake	hotplate	90 s, 160 °C
	e-beam exposure	Zeiss Supra 55	20 kV, 10 μm aperture, membranes: 400 $\mu\text{C cm}^{-2}$ wafer: 200 $\mu\text{C cm}^{-2}$
	develop	AR-600-56	120 s, 20 °C
	stop/clean	AR-600-60	20 s \rightarrow H ₂ O \rightarrow N ₂
	O ₂ plasma clean	Plasma Prep III	70 W, 0.5 mbar, 60 – 80 s
	thermal evaporation	Balzers-Pfeiffer (PLS500)	Py 60 nm (boat) $p_{\text{start}} < 2 \cdot 10^{-7}$ mbar
	lift-off	acetone	\approx 20 min, 56 °C \rightarrow isopropanol \rightarrow H ₂ O \rightarrow N ₂
striplines	spin coat	PMMA 600K	6000 U/min, 60 s, accel. 6000
	bake	hotplate	120 s, 160 °C
	e-beam exposure	Zeiss Supra 55	10 kV, 120 μm aperture, 180 $\mu\text{C cm}^{-2}$
	develop	AR-600-56	120 s, 20 °C
	stop/clean	AR-600-60	20 s \rightarrow H ₂ O \rightarrow N ₂
	thermal evaporation	Balzers-Pfeiffer (PLS500)	Cu: 120 nm (boat) Au: 5 nm (crucible)
	lift-off	acetone	\approx 20 min, 56 °C \rightarrow isopropanol \rightarrow H ₂ O \rightarrow N ₂

Danksagung

Für die Unterstützung bei der Anfertigung meiner Dissertation möchte ich den folgenden Personen danken:

- Prof. Dr. Ulrich Merkt für die Möglichkeit meine Dissertation in Gruppe N durchführen zu können und die Aufnahme ins Graduiertenkolleg 1286.
- PD Dr. Guido Meier für die Übernahme des Erstgutachtens sowie für die hervorragende Betreuung.
- Prof. Dr. Ralf Röhlsberger für die Übernahme des Zweitgutachtens.
- Der Deutschen Forschungsgemeinschaft (via Graduiertenkolleg 1286 und Sonderforschungsbereich 668) für die finanzielle Unterstützung.
- Dem Helmholtz Zentrum Berlin für die Gewährung von Strahlzeit am Synchrotron BESSY II sowie Dr. Markus Weigand und Michael Bechtel für den Support vor Ort.
- Dr. Katrin Buth für meine Rekrutierung als HiWi der Gruppe N in 2008 und für die Koordination des Graduiertenkollegs 1286, insbesondere der Monthly Highlights, die sehr geholfen haben meine Arbeit zu strukturieren.
- Max Hänze für die sehr gute und beständige Zusammenarbeit während seiner Masterarbeit und danach.
- Den Teilnehmern gemeinsamer Messreisen Carolin Behncke, Max Hänze, Matthias F. A. Pues, Benedikt Schulte, Dr. Falk-Ulrich Stein und Dr. Andreas Vogel.
- Allen aktuellen und ehemaligen Mitgliedern der Gruppe N, insbesondere meinen langjährigen Büro-Kollegen Matthias F. A. Pues, Dr. Falk Stein und Clemens Wuth.
- Sandra Schröder und Max Hänze für die Unterstützung bei der Durchsicht dieser Arbeit.
- Meinen Eltern Heinz-Volker und Ingrid Adolff für den Rückhalt und die Unterstützung während meines gesamten Studiums.

Zuletzt wünsche ich den zukünftigen Doktoranden viel Erfolg im Verlaufe ihrer Promotion.